Stockholm University

# Master Thesis

**Degree Project in Geology 60 hp**

# Carbonate alteration and mineralisation in the Arabian-Nubian Shield, Egypt

Ahmad Boskabadi

Stockholm 2013

Department of Geological Sciences
Stockholm University
SE-106 91 Stockholm

# Carbonate alteration and mineralisation in the Arabian-Nubian Shield, Egypt

Ahmad Boskabadi

This master thesis consists of a summary, two papers and a conference abstract. Below is the list of the papers and the abstract.

Paper I:

**The extent and conditions of alteration surrounding the Tarr carbonatite-albitite complex, Sinai Peninsula, Egypt.**

Paper II:

**Regional carbonate alteration in the ophiolitic components of Meatiq area, Central Eastern Desert (CED), Egypt: Isotopic evidence and geochemical aspects.**

Conference abstract:

**Regional carbonate alteration in the Eastern Desert of Egypt: Isotopic evidence for a mantle-derived fluid source.**

Stockholm University, June 2013

## 1. Introduction

The migration of carbonate-rich solutions was common during the evolution of the Arabian-Nubian Shield (ANS), forming veins and dikes, and causing diffuse and pervasive carbonation of basement rocks (Stern and Gwinn, 1990). Large areas of the Central Eastern Desert are altered ophiolite fragments implying huge fluxes of $CO_2$. The source and timing of these fluxes is not known. Investigation of theses carbonates can provide vital insight into the evolution of ANS. The carbonation of ophiolitic basements is also drawn attention of geologist because of their worldwide association with gold mineralisation (e.g., Barnes et al. 1973; Buisson and Leblanc, 1985, 1986; Aydal, 1990; Koç and Kadıolu, 1996; Uçurum, 2000). Recently, the carbonated ophiolitic basement of ANS is receiving more attention because of the potential association with economic gold concentrations (Oweiss et al. 2001; Ramadan, 2002; Zoheir and Lehmann, 2011; Azer, 2013).

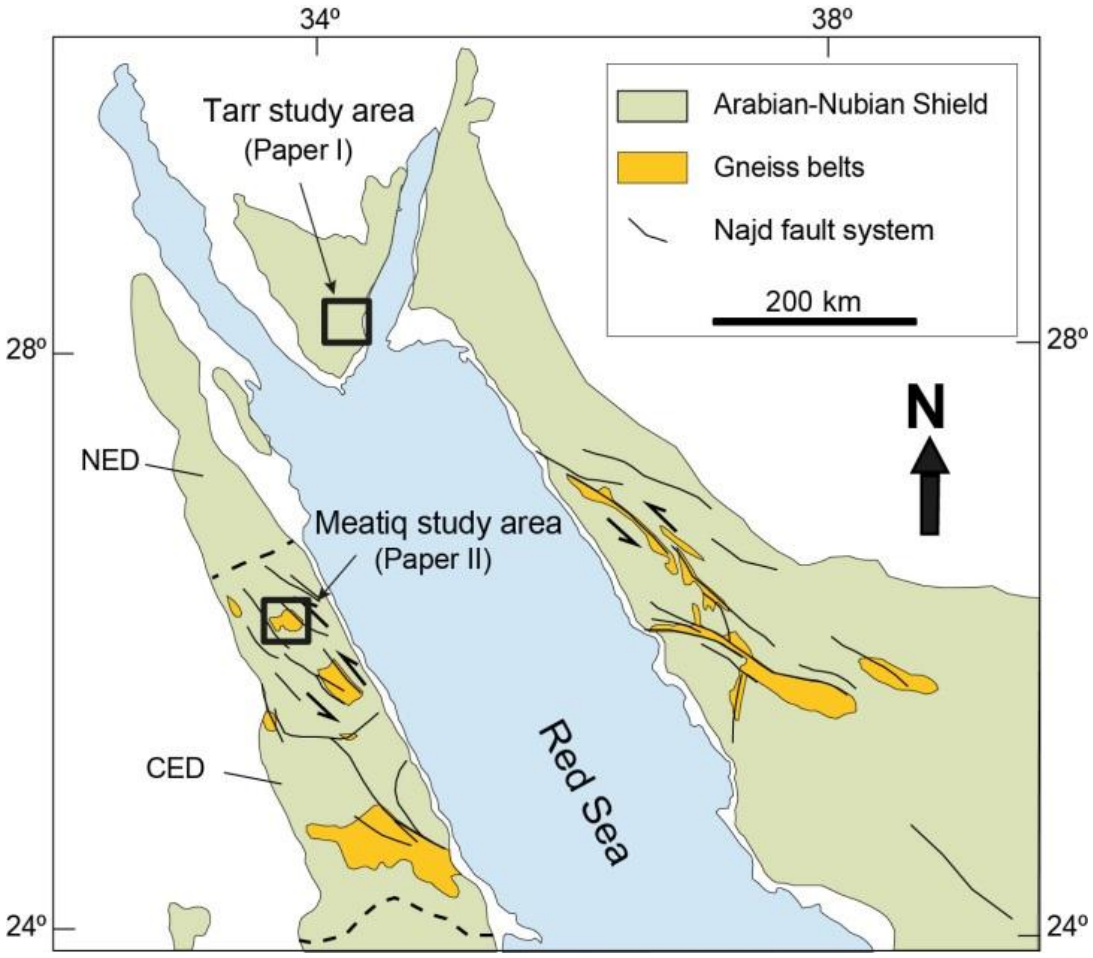


**Fig. 1** General simplified map of ANS showing Tarr study area, southern Sinai and Meatiq study area, CED, Egypt.

This study investigates two examples of carbonation in Neoproterozoic basement of ANS (Fig. 1). The first example found at Wadi Tarr in southern Sinai is a series of carbonatite dykes associated with hypabyssal and sub-volcanic albitite (paper I) whereas the second example is an area of carbonate alteration within ophiolitic fragments in the Meatiq area, Central Eastern Desert (paper II and EGU 2013 conference abstract). Previous investigations of the carbonatites at Wadi Tarr have reached little consensus on the classification of these rocks, their source and genetic mechanisms (Shimron et al. 1973; Shimron, 1975; Bogoch et al. 1982, 1986; Bogoch and Magaritz, 1983; Blasy et al. 2001; Azer et al. 2010). The rocks have previously been described as "intrusive carbonates" rather than carbonatites, mainly due to their low Sr, Ba, Nb, Y, Th and REE contents compared to "classic" carbonatites (Bogoch et al., 1986; Stern and Gwinn, 1990; Blasy et al. 2001; Azer et al.

2010). The carbonate dykes are clearly intrusive and classify as carbonatites according to the IUGS classification. Isotopic (H, O, C and Sr) compositions of dolomite, the dominant carbonate mineral in these rocks, are consistent with a mantle source Azer et al. (2010). Fennitic alteration (alkali metasomatism associated with alkali-silicate and carbonatite igneous activity; Le Bas, 2008) that is a common occurrence around carbonatite complexes has also been reported from the Tarr area but with little agreement as to its extent and significance (Shimron 1975; Bogoch et al. 1986). A re-evaluation of the Tarr carbonatite-albitite complex and the extent of associated fennitic alteration are clearly required.

The second example investigates an area of diffuse carbonate alteration affecting ultramafic portions of the ophiolitic fragments in the Central Eastern Desert (CED). The prevalence of carbonate alteration of ANS ophiolitic ultramafics suggests a tremendous flux of $CO_2$-rich fluids from the mantle during middle and late Neoproterozoic time (Newton and Stern, 1990; Stern and Gwinn, 1990). However, the source of this $CO_2$ is unknown. Previous isotopic analyses have focused on the intrusive carbonates in the CED (Stern and Gwinn, 1990). The diffuse carbonate alteration of the ophiolite complexes has been suggested to play an important role in the formation orogenic gold deposits both globally and in the CED. A large number of orogenic gold deposits occur in the CED and a significant proportion of these occurs in or near carbonate altered ultramafic rocks (Abd El-Rahman et al. 2012; Botros, 2002, 2004). The source of the $CO_2$ rich fluid that caused this carbonate alteration and its association with the gold deposits clearly needs further investigation.

In this study, we present new field and geochemical, isotopic and microthermometric data in order to determine the origin of $CO_2$-rich fluids and the conditions of alteration in both Wadi Tarr and Meatiq area. We also present geochemical data to investigate the extent of element mobility that occurred during carbonate alteration in these two field areas.

## 2. Geological settings

### 2.1. Tarr carbonatite-albitite complex, Sinai Peninsula, Egypt (paper I)

The Tarr carbonatite-albitite complex (TCA) occurs in the southernmost part of the Wadi Kid metamorphic core complex, southern Sinai (Fig. 1). The Tarr Formation that hosts the intrusion is a volcano-sedimentary succession that mostly consists of pelitic schists, conglomerates, metagraywackes and carbonate metasediments. The main carbonatite-albitite body occurs as an irregularly shaped intrusive covering 1.2 $km^2$. Recent U–Pb zircon dating yields age of 605±15 Ma for the Tarr albitite (Azer et al. 2010). The carbonatite occurs within breccia zones that surround the albitite bodies in the form of small dyke-like bodies (several centimeters up to 1m wide). The breccia zone (from few meters up to 30 m thick) can be subdivided into albitite-breccia proximal to the intrusion and volcanic-breccia within the country rock. The albitite-breccia (interior-breccia) consists of angular albitite clasts in a matrix of dark green fibrous amphibole and minor intrusive carbonates while the volcanic breccia (exterior-breccia) consists of angular fragments of volcanic country rocks, mainly pyroclastic rocks, cemented by intrusive carbonate.

### 2.2. Meatiq area, Central Eastern Desert (paper II and EGU abstract)

The Meatiq core complex (MCC) occurs within the Najd mega shear zone (Fig. 1) and represents the structurally lower unit in the CED which exposed in a tectonic window through the Neoproterozoic cover nappes and include ophiolites and island-arc volcanic rocks (Loizenbauer et al. 2001). The investigated area in the northern and southern parts of Meatiq dome mostly comprises of dismembered ophiolitic components of serpentinite, meta-volcanic, meta-gabbro, talc-rich rocks and metasediments. Serpentinites constitute an abundant part of ophiolite components in the north and the south parts of study area and became sheared and

foliated near contacts and along shear zones where these are replaced by late talc-rich rocks. The alteration of serpentinites to talc-rich rocks has been of variable intensity. In outcrop, the talc-rich rocks are mostly soft due to surface weathering, talcose and in places with schistose fabrics. The magnesite and dolomite together with quartz and minor chlorite observed mostly in talc-rich rocks and sheared serpentinites, forming veins (up to 50 cm), nodules or irregular pockets. The ophiolitic meta-volcanics of study area have been metamorphosed under greenschist-amphibolite facies.

## 3. Sampling

### 3.1. Tarr area

The original aim of this study was to investigate the occurrence of fennitic alteration surrounding the TCA and for this purpose, samples of albitite, breccia zone, intrusive carbonates and country rocks were collected along two main transects; the Northern Transect and Wadi Khashm El-Fakh.

### 3.2. Meatiq area

Ophiolitic rocks of the Meatiq area are the focus of this study and comprise mainly of serpentinites, talc-carbonates, metagabbro and amphibolites (meta-volcanics) which are in tectonic contact with the metasediments (Shackelton et al. 1980; Loizenbauer et al. 2001). Two areas exposing fragmented ophiolitic rocks have been investigated in this study, one in the north (north locality) and one in the south (south locality) of the Meatiq dome. These two localities have been selected based on different degree of serpentinites alteration, and on the availability of fresh material from quarries. The lithologies at two localities are mostly composed of serpentinite, meta-volcanic rocks, talc-carbonate and metasedimentary rocks with minor quartz and carbonate veins. In order to discern the source of altering fluid, condition of alteration and chemical changes during alteration/metamorphism in Neoproterozoic basements of study areas, several samples from different rock types and associated carbonate (and quartz) veins were collected.

## 4. Analytical Methods

**SEM**

The mineralogy of selected rocks were examined on polished thin sections using a Philips XL30 FEG environmental scanning electron microscope (ESEM) at the Department of Geological Sciences, Stockholm University, operating at 20 kv and equipped with OXFORD energy dispersive analytical X-ray spectrometer.

**XRF/LA-ICP-MS**

Thirty two samples (twenty nine from Tarr area-paper I and three from Meatiq area-paper II) were analysed for major elements using ZSX Rigaku Primus II X-ray Fluorescence spectrometer at Geological Sciences Department, Stockholm University. The XRF analyses were carried out on fused-glass discs (flux-to-sample ratios of 5:2) for major elements. In-house standard (AGV-2) was also analysed to check the accuracy and precision of the method.

After XRF analyses, the trace element analyses of the three samples (Meatiq area, paper II) fused glass discs were performed by LA-ICP-MS, utilising an 193 nm ArF excimer laser coupled to a Thermo X-Series II quadruple ICP-MS at the PetroTectonics Facility, Stockholm University. Analytical conditions comprised a laser beam diameter of 150μm, laser frequency of 10 Hz and laser energy density of 7.5 J/cm$^2$. Nitrogen ($N_2$) gas with a flow rate of 3.0 ml/min was used to increase the sensitivity. Additionally to the external standard

reference material NIST 612, BCR-2G was analysed to control the accuracy. The internal standard used was $^{29}Si$. Forty seven one rock samples (twenty nine from Tarr and eighteen from Meatiq) were analysed for trace elements and eighteen samples of Meatiq were also analysed for major elements using method of lithium metaborate/tetraborate fusion ICP Whole Rock (Package Code 4B) and a trace element ICP/MS (package Code 4B2) at Activation Laboratories Ltd. (Actlabs), Canada.

**EMPA**

Concentrations of Ti, Zr and other trace elements (paper I) in rutile were measured by field emission electron probe microanalyser (FE-EPMA), JXA-8530F JEOL HYPERPROBE, equipped with four wavelength dispersive spectrometers (WDS), secondary (SE), backscattered electron detectors (BSE) and energy dispersive spectrometer (EDS) at Department of Earth Sciences, Uppsala University, Sweden. Rutile grains were selected in polished thin sections for in situ measurements. For EPMA analysis, we adopted analytical conditions described by Zack et al. (2004) in order to get the best detection limit possible. Accelerating voltage was 20 kV with 100 nA beam current and 5 μm 170 beam spot.

**Microthermometry**

Microthermometric analyses (paper I and II) were carried out in the temperature range -180° to 600°C with a Linkam THM 600 heating and cooling stage mounted on a Nikon microscope utilising a 40x long working-distance objective at the Department of Geological Sciences, Stockholm University.

**Raman spectroscopy**

To identify the gases in the fluid inclusions, Raman spectrometric analyses (paper II) were performed using a laser Raman confocal spectrometer (Horiba instrument LabRAM HR 800) equipped with a multichannel air cooled CCD detector at the Department of Geological Sciences, Stockholm University. An Ar-ion laser ($\lambda$ = 514 nm) was used as the excitation source with an output power at the sample of 8 mW. The instrument was integrated with an Olympus microscope and the laser beam was focused to a spot of 1 μm with a 100x objective. The spectral resolution is about 0.3 $cm^{-1}$.

**Stable isotopes (C and O)**

Carbon and oxygen isotope analysis (paper II) was undertaken using an automated triple-collector gas source mass spectrometer (Analytical Precision AP2003) linked to an automated gas preparation device at the Scottish Universities Environmental Research Centre, East Kilbride. For the C-isotope analyses, c. 2 mg of the powdered whole-rocks and carbonate veins samples were reacted with 103% phosphoric acid to produce carbon dioxide, which was then purified before analysis. Results are reported as δ‰ values relative to the V-PDB and V-SMOW scales for C- and O-isotopes, respectively.

**Trace element and Sr isotope**

Trace element and Sr isotope analysis was carried out at the National Oceanography Centre, Southampton, UK. Samples were dissolved in a hydrofluoric, perchloric and nitric acid mixture on a hot plate overnight and made up to mother solutions in hydrochloric acid. For trace element analysis the mother solutions were subsampled to produce a 4000x dilution daughter solution for ICP-MS analysis. The sub sample was dried down and then dissolved in 3% $HNO_3$ containing 5ppb In and Re and 20 ppb Be to act as internal standards. The solution was analysed on a ThermoFisher Sicientific XSeries 2 ICP-MS using international rock standards to calibrate.

The mother solutions were then subsampled to give approximately 1μg Sr and the Sr isolated using 50μl Sr-Spec resin columns, the column blanks were <0.1ng. The dried samples were loaded onto a single Ta filament with a Ta activator solution. $^{87}Sr/^{86}Sr$ was analysed using multidynamic peak jumping routines on ThermoFisher Scientific Triton Plus Thermal Ionisation Mass Spectrometers with a beam size of $^{88}Sr$ = 2V normalised to $^{86}Sr/^{88}Sr$=0.1194. The long term average for NBS987 on the instrument is 0.710244±0.000019 (2sd) on 138 analyses.

**Gold analyses**

Gold analysis at Stockholm University was carried out using a Thermo XSeries 2 ICP-MS following the ultra-low detection limit method (<10 ppt) described in Pitcairn et al. (2006). Analytical precision for Au analysis at Stockholm was controlled through analysis of CANMET reference material TDB1 and Rocklabs reference materials OxA71 and SE44. Multiple analyses of TDB1 (n = 21), OxA71 (n = 10) and SE44 (n = 4) yield values of 6.3 ± 1.7 ppb, 80 ± 8.5 ppb, and 599 ± 64 ppb respectively which compare favorably with certified values of 6.3 ± 1 ppb, 85 ± 6 ppb, and 606 ± 17 ppb.

## 5. Summary of results

The results of the two papers are briefly described below.

### 5.1. Paper I: The extent and conditions of alteration surrounding the Tarr carbonatite-albitite complex, Sinai Peninsula, Egypt

Paper I reports petrography, mineralogy and geochemistry of TCA and volcanic host rocks in the vicinity. The microthermometry and thermometry are the first case study in the TCA area.

The petrography studies show that, albitite bodies are mostly composed of albite (90-95%) and minor of quartz and biotite. Accessory minerals include apatite, zircon, titanite, monazite, rutile, allanite and xenotime, and secondary sericite, chlorite and Fe-oxides also occur. The country rock units consist dominantly of weakly altered to unaltered pyroclastic rocks. The main phenocrysts and crystal fragments in the pyroclastic rocks are plagioclase and quartz with minor amount of K-feldspar, biotite, chlorite, sericite and epidote. These rocks do not show any regional metamorphic overprint. In the Northern Transect, cordierite schists also occur in the country rock, They consist of cordierite in groundmass of biotite, chlorite, sericite and opaque minerals and have been locally mylonitized. The carbonatites occur as dyke-like bodies, veins and as cement in breccia zones spatially associated with the main albitite body. The carbonatites contain dolomite, breunnerite and rare calcite with accessory apatite, chlorite and iron oxides. The dolomite is white to light grey while the breunnerite (ferroan magnesite with 5-50% $FeCO_3$) is dark brown in color. The contact between albitite and country rock (volcanics) is sharp and highly brecciated. Two types of breccia are distinguished; an interior albitite-hosted breccia, and an exterior volcanic-hosted breccia. The albitite-breccia comprises angular fragments of albitite with matrix of fibrous amphiboles and minor carbonate. Dolomite and calcite occur as cement and fracture-filling together with actinolite and chlorite. The volcanic-breccia consists of angular to sub-angular fragments of tuff, invaded by veins of carbonate, albite and minor actinolite and epidote. Carbonates (mostly breunnerite) occur as fracture-filling cement or replacing primary feldspars and amphiboles in volcanic country rocks. Coarse grained, dark-green dolerite or lamprophyre dykes occur proximal to the albitite margin, dominantly within or close to the breccia zone. They comprise phenocrysts of augite and brown hornblende, with calcic plagioclase as lath shaped phenocrysts and/or as a matrix phase, and minor magnetite, ilmenite and carbonate.

The geochemical results show that albitite contains 67.1 to 67.7 wt.% $SiO_2$, ~19 wt.% $Al_2O_3$, and ~11 wt.% $Na_2O$, similar to the "typical" albitite of Kinnaird and Bowden (1991). Concentrations of all other majors are below 1%. The albitite breccia samples generally contain lower $SiO_2$, $Al_2O_3$ and $Na_2O$ and higher CaO, MgO, MnO and $Fe_2O_3$ than the fresh albitite. There are no clear differences in minor and trace element concentrations albitite and albitite breccia samples with the exception of breccia sample T8, which has significantly higher LREE and $P_2O_5$. The least altered volcanic country rock samples contain 61.9 to 64.5 wt.% $SiO_2$, 16.5 to 17.1 wt.% $Al_2O_3$, 4.8 to to 7.6 wt.% $Na_2O$, 5.1 to 7.2 wt.% $Fe_2O_3$, 2.1 to 3.2 wt.% MgO, 1.3 to 3.8 wt.% $K_2O$ and 1 to 2.5 wt.% CaO with all other majors being below 1 wt.%. In comparison to the albitite they contain lower $Na_2O$, Zr and Nb but higher $K_2O$, $Fe_2O_3$, MgO and MnO, Ba, Rb, Sr, V, Cr, Ni. The volcanic breccia samples have more variable compositions than the least altered volcanic country rock, although some samples contain lower $Al_2O_3$ and higher CaO, MgO, $P_2O_5$, $TiO_2$, Cu and Pb. The metasedimentary rocks contains 60.1 to 62.5 wt.% $SiO_2$, 15.8 to 16.6 wt.% $Al_2O_3$, 7.1 to 8.8 wt.% $Fe_2O_3$, 6.7 to 9.4 wt.% MgO, 0.5 to 2.9 wt.% $Na_2O$, 1.9 to 3.2 wt.% $K_2O$ and 1 to 1.2 wt.% CaO with all other majors being below 1 wt.%. The carbonatite samples analysed in this study contain ~21 to 29 wt.% MgO, 15.1 to 19.6 wt.% CaO, 9.7 to 15.3 wt.% $Fe_2O_3$, and 0.7 to 4.1 wt.% $SiO_2$. The trace element concentrations are low with <260 ppm Sr, <20 ppm Ba and less than 35 ppm ∑REE. The samples represent mixtures of dolomite and breunnerite. Representative analyses of dolomitite and breunneritite reported in previous studies show that dolomitite contains higher CaO, Sr, Y and REE and lower $Fe_2O_3$, V, and Ni, than the breunneritite (Bogoch et al. 1986; Azer et al. 2010). The lamprophyre samples contain 47.2 to 54 wt.% $SiO_2$, 13.4 to 16.5 wt.% $Al_2O_3$, 7.8 to 13.6 wt.% $Fe_2O_3$, 7.7 to 8.5 wt.% CaO, 5.7 to 8 wt.% MgO, 1.2 to 2.1 wt.% $TiO_2$, and 0.8 to 1.1 wt.% $K_2O$.

Zr-in-rutile thermometry has been used to estimate the crystallisation temperature of hydrothermal rutile and other coexisting REE-host minerals in both breccia zones. The Zr-in-rutile thermometry is based on Zr concentrations in rutile coexisting with quartz and zircon (Zack et al. 2004; Watson et al. 2006; Ferry and Watson, 2007; Tomkins et al. 2007). Based on the Ferry and Watson (2007) calibration, the albitite and volcanic breccias give various temperatures that range between ~520 to 630°C. Three types of fluid inclusions ($CO_2$-rich, halite-bearing aqueous and aqueous) have been identified in dolomite and breunnerite veins and studied for condition of alteration. The aqueous inclusions occur only in breunnerite that shows a recrystallised texture.

### 5.2. Paper II and EGU conference abstract: Regional carbonate alteration in the ophiolitic components of Meatiq area, Central Eastern Desert (CED), Egypt: Isotopic evidence and geochemical aspects

Paper II and abstract conference report petrography, geochemistry and isotopic (C, O and Sr) compositions of ophiolitic sequences in two localities in Meatiq area. The gold analysis in ophiolitic rocks is the first case study in the Meatiq area. Stable isotope (C and O) and radiogenic $^{87}Sr/^{86}Sr$ ratio of carbonated serpentinites and meta-volcanics and of pure carbonate veins are used to constrain the origin of the fluid involved.

Two varieties of serpentinite, Lz-serpentinite (lizardite-serpentinite) and Atg-serpentinite (antigorite-serpentinite) have been identified by microscopic observations and Raman micro-spectroscopy in the study area. Field and microscopic observations show that the carbonate alteration is more pervasive in Atg-serpentinites. The bulk rock geochemistries of ophiolitic rocks (e.g., two types of serpentinites and talc-rich rocks) reflect the differences between their mineralogy. The results indicate that major elements show no remarkable variations between two serpentinites varieties. However, some trace elements including FME (Li, As, S, Pb, U, Ba, Sr and Au except Sb and Cs) and LREE show systematic decrease from the Lz-serpentinite

group compared to the Atg-serpentine and talc-rich rocks groups. The talc-rich rocks make a distinct group with different major elements concentrations compared to the two types of serpentinite. However, their absolute trace elements contents (Cr, Ni and Co) show close similarities to serpentinites. Compared to non-metasomatic protoliths, talc-rich rocks are extremely depleted in some FME (e.g., As, S and Au). The major and trace element concentrations in meta-volcanics show no significant correlation with serpentinites and talc-rich rocks.

Based on isotopic data, the meta-volcanics and carbonate veins define distinct group with lowest $\delta^{13}C$ (-6.8 to -10.0‰) and $\delta^{18}O$ (+6.4 to ~+11.1‰) with fairly uniform values of radiogenic $^{87}Sr/^{86}Sr$ ratio (0.70280 to 0.70344). Two serpentinite phases with highest values in $\delta^{13}C$ (-4.1 to -5.9‰), $\delta^{18}O$ (+10.3 to +15.1‰) and $^{87}Sr/^{86}Sr$ ratios (0.70396 to 0.70623) define another distinct group within different Meatiq samples. Three different inclusions (aqueous, aqueous-carbonic and carbonic types) have been studied in quartz and carbonate (dolomite, magnesite) veins for evaluating the condition of altering fluid in the Meatiq study area. Raman spectrometric analyses show mostly pure $CO_2$ gas for the inclusions in carbonate veins while traces of $N_2$ and $CH_4$ have been identified in quartz veins.

## 6. Discussion

### 6.1. Paper I: Tarr area

The stable and radiogenic isotope compositions of dolomite (mean $\delta^{18}O$ = +6.9‰; mean $\delta^{13}C$ = -8.1‰; mean $\delta D$ = -65‰, mean $\varepsilon Nd$ = +3.4 to +5.49; $^{87}Sr/^{86}Sr$ = 0.70356 to 0.70422; Bogoch et al. 1986; Azer et al. 2010) indicate they were derived from a mantle source whereas the isotopic composition of the breunnerite also shows a dominantly mantle source but with partial re-equilibration with surface derived fluids such as seawater (mean $\delta^{18}O$ = +18.85‰; mean $\delta^{13}C$ = -6.1‰; mean $\varepsilon Nd$ = +2.2; mean $^{87}Sr/^{86}Sr$ = 0.70805; Azer et al. 2010). Besides the clear spatial association, an isotopic and geochemical association can also be observed between the albitite and the carbonatites in the TCA (Shimron, 1975; Bogoch et al. 1986; Blasy et al, 2001; Azer et al. 2010). The albitite has similar isotopic compositions that indicate a mantle source similar to the carbonatite and supporting the interpretation that these rocks are genetically linked (Azer et al. 2010). The lamprophyres are also strongly carbonated and the isotopic and geochemical characteristics of the carbonate in these rocks are reported to be similar to the carbonatites (Bogoch and Magaritz, 1983). In addition, normalised REE patterns for the albitite, dolomite from the carbonatite, volcanic country rock and lamprophyre are very similar indicating the possibility of a common source for these rocks. We suggest that based on 1) the field relationships, 2) the isotopic compositions, and 3) the chemical compositions, specifically of the REE, that the Wadi Tarr igneous complex should be classified as a carbonatite-albitite-lamprophyre igneous complex, and that these rocks come from a common mantle derived source. Azer et al. (2010) suggest that the magmas were separated through liquid immiscibility in a magmatic cupola at hypabyssal depths. Tarr carbonatite is characterized by depletion in trace elements (specifically Sr, Ba and REE) relative to average classic carbonatite. REE poor carbonatites have been reported for a number of localities in the ANS (e.g. El-Haddad et al. 1984) and it is possible that this is a function of a regional scale REE-poor source area for the ANS.

The mineralogy investigation shows that actinolite, carbonate, chlorite, sericite and epidote occur in the both the albitite and volcanic country rock-hosted breccia. The lamprophyre samples that also occur in the breccia zone are strongly altered with sericitised and epidotized feldspar, clinopyroxenes altered to chlorite ± carbonate ± Fe-oxides, and primary hornblende altered along grain margins to actinolite ± tremolite. None of the minerals commonly associated with fennitisation such as Na-rich amphiboles or pyroxenes, or alkali feldspar occur in the altered breccia zone samples or distal to the intrusion.

The geochemical compositions also suggest that large-scale alkali metasomatism has not occurred. Normalised albitite breccia and volcanic breccia compositions are shown in figure 2. The albitite breccia and carbonatite samples have been normalised to the composition of fresh albitite, and the volcanic breccia samples have been normalised to the composition of least altered volcanic country rock. Neither the metasedimentary rocks or the lamprophyres have not been included, as we do not know the composition of the unaltered protolith rock that would allow normalisation. The diagrams show that the alteration in the breccia zones is dominantly controlled by precipitation of carbonate. $SiO_2$, $Al_2O_3$, $Na_2O$ and $K_2O$ show lower concentrations in the albitite and volcanic breccia and in the carbonatites compared to their unaltered end member compositions (Fig.2a), whereas CaO, MgO, $Fe_2O_3$ and MnO concentrations are higher in the albitite and volcanic breccia and in the carbonatites compared to the fresh albitite and volcanic country rock (Fig. 2b). The breccia samples plot on mixing lines between the fresh albitite and volcanic compositions and that of the carbonatites (Fig. 2a, b). In the albitite breccia the dilution and enrichment trends shown in figures 2a and 2b can be attributed to the occurrence of carbonates, but also to the precipitation of actinolite, epidote and chlorite. In the volcanic breccia the depletion and enrichment trends are attributed to hydrothermal alteration of K-feldspar and plagioclase to sericite + carbonate ± epidote leading to dilution of silica, $Al_2O_3$ and $K_2O$. Enrichment of CaO, MgO occurring in some volcanic breccia samples, is attributed to diffusive veinlets of carbonates and albite.

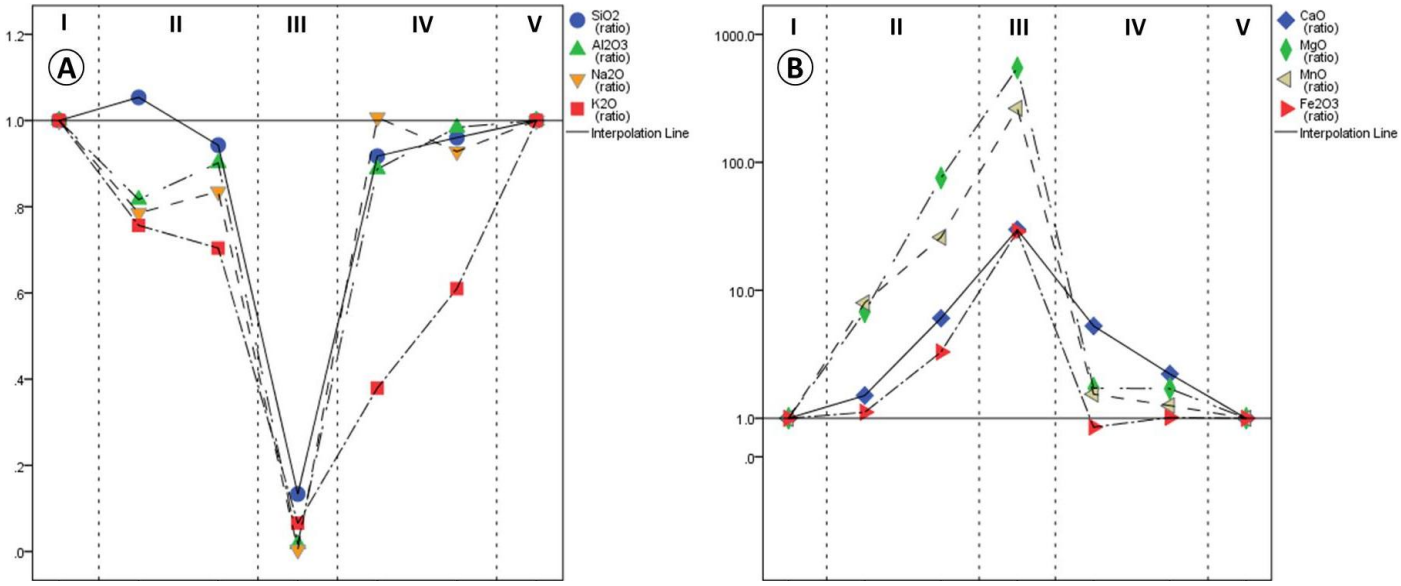


**Fig. 2** Plots of normalised elemental concentrations of albitite and volcanic breccia and carbonatite samples; I: fresh albitite, II: albitite-breccia, III: intrusive carbonate, IV: volcanic-breccia, V: least altered volcanics**. (a)** $SiO_2$, $Al_2O_3$, $Na_2O$ and $K_2O$**; (b)** CaO, MgO, $Fe_2O_3$ and MnO and $Fe_2O_3$. The albitite breccia samples were normalised to fresh albitite (the mean of samples T7, T19 and T20), and the volcanic breccia samples to least altered volcanic country rock (the mean of T28, T34, and T41). Carbonatites were normalized to fresh albitite so that they fit on the same diagram. The diagrams show that the alteration in the breccia zones is dominantly controlled by precipitation of carbonate.

In summary, fennitisation surrounding the TCA observed in this study is limited in scale occurring only in the zone of brecciation immediately surrounding the intrusion, and limited in degree being mainly controlled by carbonate precipitation. We suggest that fennitisation has occurred but extent of this alteration is spatially variable and most likely lithologically controlled.

Fluid inclusions and Zr-in-rutile thermometry indicate that the intrusive carbonates at Wadi Tarr were formed after immiscibility of a high-temperature (~520°-630°C) and high-salinity $H_2O$-$CO_2$-NaCl-$CaCl_2$ parental fluid. The fluid had a magmatic source and was exsolved from crystalising albitite magma under lithostatic pressure. Immiscibility of the parental fluid was initiated at a depth of 4.9 to 2.8 km and a temperature of 420° to 480°C. Primary fluid inclusions reveal similar fluid characteristics for both dolomite and breunnerite implying that both carbonate phases preserve the original magmatic fluid signature. However also contains secondary aqueous (type 3) fluid inclusions in breunnerite with low salinity (3.6 to 5.1 mass% NaCl eq.) and a homogenization temperature (~180°C) suggest interaction with a surficial fluid such as meteoric water or seawater, which most likely led to the partial isotopic re-equilibration of breunnerite (Bogoch et al. 1986; Azer et al. 2010).

### 6.2. Paper II and EGU conference abstract: Meatiq area

Recent studies show that the Egyptian ophiolitic basements are dismembered serpentinized mantle peridotite slices of ANS which formed in a suprasubduction (SSZ) setting (Stern et al. 2004; El Gaby, 2005; Azer and Stern, 2007) however the exact nature of their setting is controversial (Stern et al. 2004; Azer and Stern, 2007; El-Sayed et al. 1999; El Bahariya, 2008; Ali et al. 2009). Based on present geochemical data the tectonic settings of Meatiq serpentinites, a forearc setting appears most likely but further work is required to confirm this.

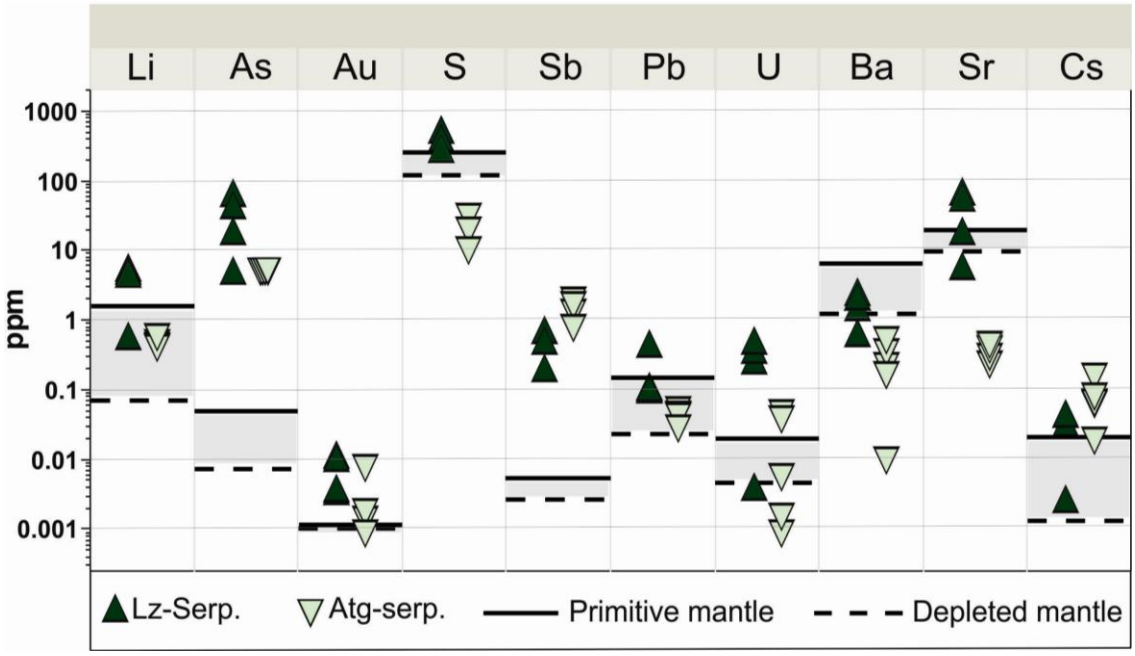


**Fig. 3** Plots of concentration of fluid-mobile elements (Li, As, Au, S, Sb, Pb, U, Ba, Sr and Cs) in two serpentine phases from Meatiq study area. Values of primitive mantle after McDonough and Sun (1995) and depleted mantle after Salters and Stracke (2004) are also reported (thick and dashed black lines). Grey boxes represent the ranges between primitive and depleted mantle.

Microscopic and geochemical data show that ultramafic rocks in the study area are highly altered to mixture of serpentine, talc, tremolite, chlorite and magnesite and dolomite. Based on mineralogy and texture evolution of Cr-spinel, it is suggested that Lz-serpentinites are least altered, Atg-serpentinites have experienced higher temperature alteration and with abundance carbonate alteration while the talc-rich rocks are extremely altered and deformed with carbonate veins. The talc-rich rocks are the metasomatite products

of serpentinites alteration in fault and shear zones. The geochemical data indicate that FME (Li, As, S, Pb, U, Ba, Sr, and Au except Sb and Cs) are depleted during transition of lizardite to antigorite and we suggest that these elements have been remobilised by $CO_2$-rich fluid that caused the carbonate alteration (Fig. 3). The talc-rich rocks were clearly formed from serpentinite protoliths and show similar depletions in some of FME (S, As, and Au) as the Atg-serpentinites.

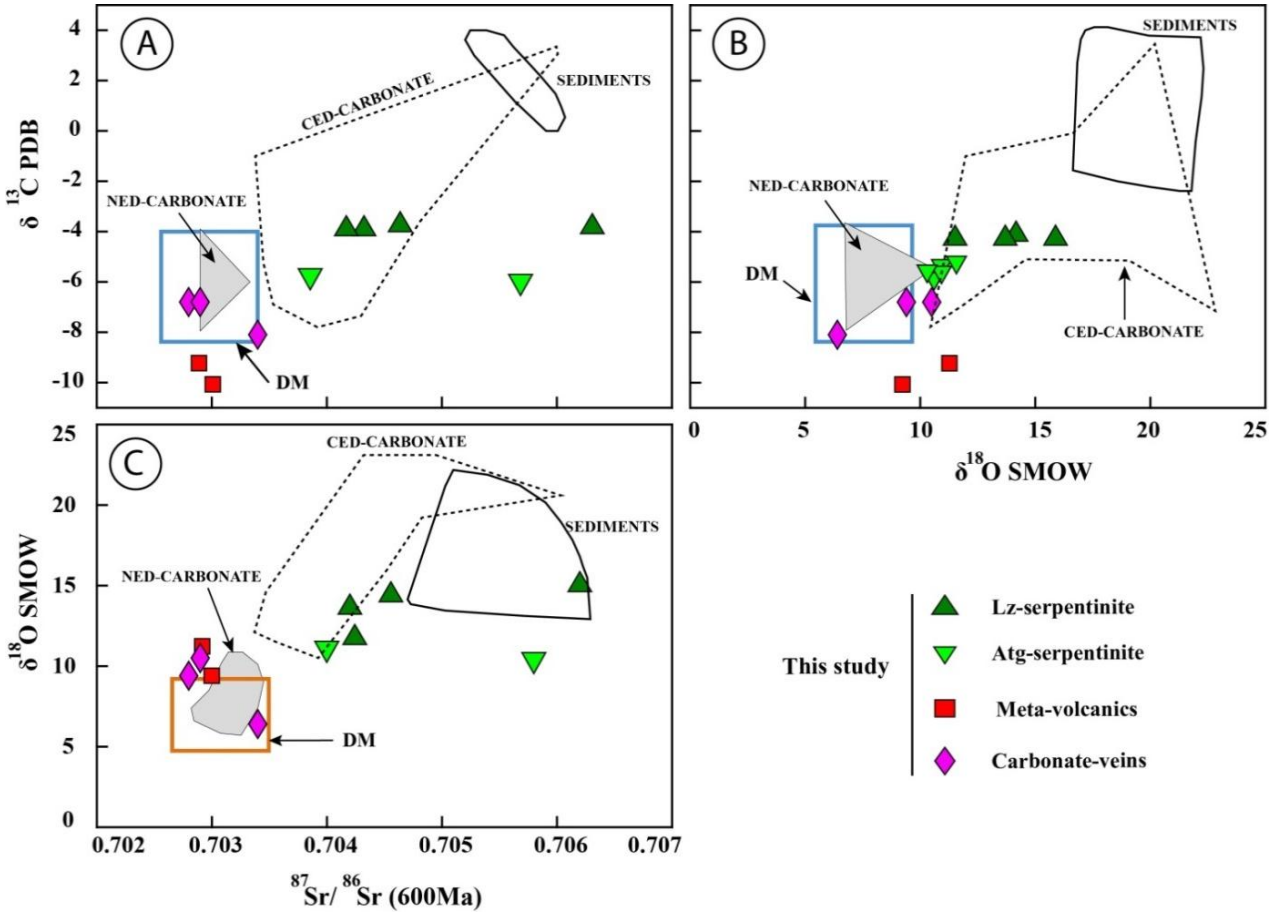


**Fig. 4** Plots of O, C and Sr isotope data for Meatiq ophiolitic rocks and carbonate veins. Data for (CED) carbonates, sedimentary and NED are shown as dashed-line, solid-line and grey area respectively (data are adopted from Stern and Gwinn, 1990); **(a)** $\delta^{13}C$ vs. $^{87}Sr/^{86}Sr$ at ~600Ma. Field of late Precambrian mantle-derived carbonates (blue boxes) is taken from C-isotopic data of Taylor et al. (1967) and Deines (1989), and Sr-isotopic data for Egyptian basement rocks (brown box) are from Stern and Hedge (1985); **(b)** $\delta^{13}C$ vs. $\delta^{18}O$ from the same samples, with similar fields displayed; **(c)** $\delta^{18}O$ vs. $^{87}Sr/^{86}Sr$ at 600Ma with similar reference fields outlined.

Stable isotope ($\delta^{13}C$ and $\delta^{18}O$) values of carbonate veins are within mantle-derived carbonate-rich fluids (Taylor et al. 1967; Demeny et al. 1998) (Fig. 4). Furthermore, the restricted range of initial $^{87}Sr/^{86}Sr$ in carbonate and meta-volcanics are indistinguishable from initial ratio for mantle-derived volcanics from Egyptian basement and Neoproterozoic igneous rocks of the Arabian-Nubian Shield (Stern and Hedge, 1985; Stern and Gwinn, 1990). This is suggesting a mantle-origin for $CO_2$-rich fluid that caused the carbonate alteration in the study area. Based on $\delta^{13}C$ stable isotope data, both serpentine phases have mantle component signature however the higher $\delta^{18}O$ values and radiogenic Sr ratios show the mantle-peridotite have interacted with external fluid (such as meteoric water, connate fluid or seawater (Fig.4a, c).

The isotopic composition of Atg-serpentinites show mixing between the Lz-serpentinite composition and the composition of carbonate veins. Based on fluid inclusion studies, the fluid responsible for alteration has Mg-Na-Cl dominated composition with a low salinity (<7 eq. mass% Mg-Na-Cl). The carbonate alteration occurred at temperature of 300 ± 30˚C and pressure of 0.7 to 1.6 kbar corresponding to a depth of ~2.6 to ~6 km. Isotopic data of carbonate veins in shear zones show large flux of mantle $CO_2$-rich fluid in the form of pervasive carbonate veins and alteration in the ophiolitic rocks of study area. The C isotopic value of serpentinites indicates that they have undergone carbonation from mantle derived C-rich fluid while the radiogenic Sr and O values in serpentinites indicate mixing between mantle and surface fluid such as meteoric water, connate fluid or seawater.

## 7. Conclusion:

### 7.1. Tarr area:

We suggest based on field and petrographic observations, and geochemical and isotopic compositions, that the TCA should be classified as a carbonatite-albitite-lamprophyre igneous complex. Fennitic alteration surrounding the TCA carbonatites is variable in extent. In the areas investigated in this study alkali metasomatism is not observed and alteration is dominated by precipitation of carbonatite in the breccia zone surrounding the albitite with spatially associated actinolite, chlorite, sericite and epidote. Previous investigations suggest more pervasive fennitisation that caused albitisation of the intrusive and country rocks (Shimron 1975, Bogoch et al. 1987). The carbonatite magma contained a high-salinity $H_2O$-$CO_2$-NaCl-$CaCl_2$ fluid that most likely caused the reported fennitisation in some areas. We suggest that fennitisation has occurred but extent of this alteration is spatially variable and most likely lithologically controlled. Crystallization of the carbonatite in the dykes and the breccia zone occurred between 565±38°C and 420°-480°C, and at 0.75 to 1.3 kbar which corresponds to a depth of 2.8-4.9 km. Small aggregates of rutile, apatite, allanite, xenotime, monazite, and zircon within the carbonatite breccia most likely crystallized early at 565±38°C. The carbonatite dykes crystallized later after cooling to around 420°-480°C. Our data support the model proposed by Azer et al (2010) of immiscibility of a carbonatite and albitite melts in a shallow-level cupola culminating in explosive emplacement of the albitite breccia and carbonatite.

### 7.2. Meatiq area:

The petrological, geochemical and isotopic study of different ophiolitic rocks from the north and south of Meatiq area (CED) provide new insights into the source of $CO_2$-rich altering fluid and element mobility associated with this process. Based on microscopy and Raman spectroscopy, two serpentine phases (lizardite and antigorite) are identified in Meatiq area. Between two serpentine phases, the Atg-serpentinites underwent intensive prograde alteration/metamorphism by $CO_2$ rich fluid. The transition of lizardite to antigorite causes a depletion in FME (except Sb and Cs), As, S and gold concentrations and it is inferred that these elements have been remobilised during this transition by the $CO_2$ rich fluid that caused carbonation. Fluid inclusion studies show that the carbonate alteration occurred at temperature of 300 ± 30˚C and pressure of 0.7 to 1.6 kbar corresponding to a depth of ~2.6 to ~6 km. Isotopic data of carbonate veins show large flux of mantle $CO_2$-rich fluid in the form of pervasive carbonate veins and alteration in the ophiolitic rocks of study area. Pervasive carbonate veins and related alteration products in the ANS represent a natural analogue of mantle degassing and crustal $CO_2$ sequestration in Neoproterozoic.

## 8. Future perspectives

The origin of carbonate veins and related alteration in Neoproterozoic basement of ANS is inferred to be mantle-origin, but the precise timing of this pervasive carbonate alteration and influx of $CO_2$ is not yet known. SEM studies of carbonate veins indicate that hydrothermal zircon, apatite and monazite could be good candidates for dating. Further investigation is needed to address the relationship between carbonatised ultramafics and subsequent granitoid intrusions and gold mineralisation in the ANS. The transition boundary and tectonic setting of lizardite to antigorite in ANS is not well clear. This might be related to prograde metamorphism and alteration in subduction zones or regional metamorphism. Still the relationship between collision of east-west Gondwana and possible slab-break off event at the end of collision is not studied. The possible relationship between slab-break off and mantle-upwelling and consequent mantle-degassing through the deep-seated structures (e.g., Najd fault systems and shears) might be an attractive subject for the future studies.

**Acknowledgements**

I would like to thank Stockholm University for providing me opportunity to become a master student at the Department of Geological Sciences. I would like to take this opportunity to express my deep gratitude to my supervisor (Dr. Iain Pitcairn), JEBEL (Jordanian-Egyptian basement evolution) team leader (Prof. Victoria Pease), colleagues, my family and my wife who have supported me in making these studies enjoyable and possible.

This thesis could not be like this if I don't have:

***Iain Pitcairn.*** Thank you, Iain for offering me this wonderful opportunity and giving me constructive advice and feedback during my work. You always encourage and support me in new scientific challenges and train me become an independent student. I will never forget how many good ideas and inspirations you offered me.

***Curt Broman.*** I would like to acknowledge your gentle, valuable advice and supports. Working with you gave me a great chance to learn about fluid inclusions. Thank you very much.

***Robert Stern.*** I greatly appreciate your brilliant guidance and insightful comments during my work. I admire your broad knowledge and experience.

I am very grateful for my co-authors Mokhles Azer, Adrian Boyce, Damon Teagle, Fathy Mohamed and Matthew Cooper for scientific contribution and constructive comments to greatly improve the manuscripts.

I want to express my grateful to Alasdair Skelton, Patrick Crill, Volker Brüchert and Joakim Mansfeld for their broad knowledge and the lessons I learnt from their courses.

I also would like to express my gratitude to Runa Jacobsson, Marianne Ahlbom, and Cora Wohlgemuth-Ueberwasser for providing technical knowledge for XRF, ESEM and LA-ICP-MS. I would like to particularly thank Dan Zetterberg for Polish thin-section preparation.

Special thanks to all my kind friend and former and present fellow PhD and Master's students.

I am also grateful for help from Elisabeth Däcker, Monica Rosenblom, Helena Bergman, Arne Lif and Elin Tollefsen with all of administrative work.

Undoubtedly, the greatest thank you is deserved by my wife, Sima Javanbakht, for her patient and endless love and believing in me. Without her love and encouragements, this study would have been much more difficult.

## References


- Abd El-Rahman, Y., Polat, A., Dilek, Y., Kusky, M.T., El-Sharkawi, M., Said, A., 2012. Cryogenian ophiolite tectonics and metallogeny of the Central Eastern Desert of Egypt. International Geology Review, iFirst, 1–15.
- Ali, K.A., Stern, R.J., Manton, W.I., Kimura, J.I., Khamis, H.A., 2009. Geochemistry Nd isotopes and U-Pb SHRIMP zircon dating of Neoproterozoic volcanic rocks from the Central Eastern Desert of Egypt: New insight into the ~750 Ma crust-forming event. Precambrian Research, 171, 1–22.
- Aydal, D., 1990. Gold-bearing listwaenites in the Arac Massif, Kastamonu, Turkey. Terra Nova, 2, 43-52.
- Azer, M.K., 2013. Evolution and economic significance of listwaenites associated with Neoproterozoic ophiolites in South Eastern Desert, Egypt. Geologica Acta , 1, 113-128.
- Azer, M.K., Stern, R.J., 2007. Neoproterozoic (835-720 Ma) serpentinites in the Eastern Desert, Egypt: Fragments of forearc mantle. The Journal of Geology, 115, 457-472.
- Azer, M.K., Stern, R.J., Kimura, J.I., 2010. Origin of a Late Neoproterozoic (605±13 Ma) intrusive carbonate-albitite complex in Southern Sinai Egypt. International Journal of Earth Sciences 99, 245–267.
- Barnes, I., O'Neil, J.R., Rapp, J.B., White, D.E., 1973. Silicacarbonate alteration of serpentine: Wall rock alteration in mercury deposits of the California Coast Ranges. Economic Geology, 68, 388-398.
- Blasy, M., Baroudy, A.F., Kharbish, S.M., 2001. Geochemical characteristics of Wadi Tarr albitite, Southeastern Sinai, Egypt. Egyptian Journal of Geology 42, 767–780.
- Bogoch, R., Bahat, D., Kisch, H., 1987. The Tarr albitite: a metasomatic plagiogranite from mainly non-intrusive protoliths. Ofioliti, 12, 8-22.
- Bogoch, R., Halicz, L., Nathan, Y., 1982. Breunnerite from the Tarr albitite complex, Sinai. American Mineralogist 67, 822–825.
- Bogoch, R., Magaritz, M., 1983. Immiscible silicate–carbonate liquids as evidenced from ocellar diabase dykes, Southeast Sinai. Contributions to Mineralogy and Petrology 83, 227–230.
- Bogoch. R., Magaritz, M., Michard, A., 1986. Dolomite of possible mantle origin, Southeast Sinai. Chemical Geology 56, 281–288.
- Botros, N.S., 2002, Metallogeny of gold in relation to the evolution of the Nubian Shield in Egypt. Ore Geology Reviews, 19, 137-164.
- Botros, N.S., 2004. A new classification of the gold deposits of Egypt. Ore Geology Reviews, 25, 1-37.
- Buisson, G., Leblanc, M., 1985. Gold in carbonatized ultramafic rocks from ophiolite complexes. Economic Geology, 80, 2026-2029.
- Buisson, G., Leblanc, M., 1986. Gold-bearing listwaenites (carbonatized ultramafic rocks) from ophiolite complexes. In: Gallagher, J.M., Ixer, R.A., Neary, C.R. (eds.). Metallogeny of Basic and Ultrabasic Rocks. London, Institution of Mining and Metallurgy, 121-132.
- Deines, P., 1989. Stable isotope variations in carbonatites. In: Bell, K. (Ed.), Carbonatites: Genesis and evolution. Unwin Hyman, London, Boston, Sydney, Wellington, pp. 301-359.
- Demeny, A., Ahijado, A., Casillas, R., Vennemann, T.W., 1998. Crustal contamination and fluidrrock interaction in the carbonatites of Fuerteventura _Canary Islands, Spain/: a C, O, H isotope study. Lithos 44, 101–115
- El Bahariya, G.A., 2008, Geology, mineral chemistry and petrogenesis of Neoproterozoic metamorphosed ophiolitic ultramafics, Central Eastern Desert, Egypt: Implication for the classification and origin of the ophiolitic mélange: Egyptian Journal of Geology, v. 52, p. 55–81.
- El-Gaby, S., 2005. Integrated evolution and rock classification of the Pan-African belt in Egypt. First Symposium on the Classification of the Basement Complex of Egypt, pp 1-9.
- El-Haddad, M.A., Hashad, M.H., 1984. The major and minor elements chemistry of Gebel Tarbtie carbonatites South, Egypt. Bull Fac Sci Assuit Univ 13, 205-217.
- El-Sayed, M.M., Furnes, H., Mohamed, F.H., 1999. Geochemical constraints on the tectonomagmatic evolution of the late Precambrian Fawakhir ophiolite, Central Eastern Desert, Egypt. Journal of African earth Sciences, 29, 515–533.
- Ferry, J.M., Watson, E.B., 2007. New thermodynamic models and revised calibrations for the Ti-in-zircon and Zr-in-rutile thermometers. Contributions to Mineralogy and Petrology 154, 429–437.

- Kinnaird, J.A., Bowden, P., 1991. Magmatism and mineralization associated with Phanerozoic Anorogenic Plutonic complexes of the African plate, In: Kampunzu, A., Lubala, R.T., (Eds.), The Phanerozoic African Plate. Springer, Berlin, 410–485.
- Koç, S., Kadıoğlu, Y.K., 1996. Mineralogy, geochemistry and precious metal content of Karacakaya (Yunusemre-Eskisehir) listwaenites. Ofioliti, 21, 125-130.
- Le Bas, M.J., 2008, Fenites associated with carbonatites: Canadian Mineralogist, 46, 915-932.
- Loizenbauer, J., Wallbrecher, E., Fritz, H., Neymayr, P., Khudeir, A.A., Kloetzli, U., 2001. Structural geology, single zircon ages and fluid inclusion studies of the Meatiq metamorphic core complex: implications for Neoproterozoic tectonics in the Eastern Desert of Egypt. Precambrian Research, 110, 357–383.
- McDonough, W.F., and Sun, S.S., 1995. Composition of the Earth. Chemical Geology, 120, 223-253.
- Newton, R.C., Stern, R.J., 1990. A late Precambrian $CO_2$ "Event". Geological Society of America, Dallas, p. 190.
- Oweiss, Kh.A., El Naggar, A.A., Abdel Razik, K.A., Moselhy, N., Ali, A.B., 2001. Gold exploration at Heiani area, South Eastern Desert, Egypt. Annals Geological Survey of Egypt, XXIV, 435-450.
- Pitcairn, K.I., Warwick, E.P., Milton J.A., Teagle, A.H.D., 2006. Method for Ultra-Low-Level Analysis of Gold in Rocks. Analytical Chemistry 78, 1290-1295.
- Ramadan, T.M., 2002. Exploration for gold-bearing listwaenites at Um Khasila area, Central Eastern Desert, Egypt. Egyptian Journal of Remote Sensing and Space Sciences. 5, 63-76.
- Salters, V.J.M., Stracke, A., 2004. Composition of the depleted mantle. Geochemistry, Geophysics, Geosystems, 5, Q05B07, 27pp.
- Shackleton, R.M., Ries, A.C., Graham, R.H., Fitches, W.R., 1980. Late Precambrian ophiolite melange in the Eastern Desert of Egypt. Nature, 285, 472-474.
- Shimron, A.E., 1975. Petrogenesis of the Tarr albitite–carbonatite complex, Sinai Peninsula. Mineralogical Magazine 40, 13–24.
- Shimron, A.E., Brookins, D.G., Magaritz, M., Bartov,Y., 1973. Origin of the intrusive carbonate rocks between the Gulf of Elat and Gulf of Suez Rifts. Israel Journal of Earth Sciences 22, 243–254.
- Stern, R,J., Johanson, P.R., Kroner, A., Yibas, B., 2004. Neoproterozoic ophiolites of the Arabian–Nubian Shield. In: Kusky TM (ed) Precambrian ophiolites and related rocks. Developments in Precambrian geology, Elsevier, Amsterdam, 13, 95– 28.
- Stern, R.J. and Hedge, C.E., 1985. Geochronologic and isotopic constraints on Late Precambrian crustal evolution in the Eastern Desert of Egypt. American Journal of Science, 285, 97-127.
- Stern, R.J., Gwinn, C.J., 1990. Origin of late Precambrian intrusive carbonates, Eastern Desert of Egypt and Sudan: C, O and Sr isotopic evidence. Precambrian Research 46, 259–272.
- Taylor, H.P., Frechen, J. and Degens, E.T., 1967. Oxygen and carbon isotope studies of carbonatites from the Laacher See district, West Germany and the Alno district, Sweden. Geochimica et Cosmochimica Acta, 31, 407-430.
- Tomkins, H.S., Powell, R., Ellis, D.J., 2007. The pressure dependence of the zirconium-in-rutile thermometer. Journal of Metamorphic Geology 25, 703–713.
- Uçurum, A., 2000. Listwaenites in Turkey: Perspectives on formation and precious metal concentration with reference to occurrences in East-Central Anatolia. Ofioliti, 25, 15-29.
- Watson, E.B., Wark, D.A., Thomas, J.B., 2006. Crystallization thermometers for zircon and rutile. Contributions to Mineralogy and Petrology 151, 413–433.
- Zack, T., Moraes, R., Kronz, A., 2004. Temperature dependence of Zr in rutile: empirical calibration of a rutile thermometer. Contribution to Mineralogy and Petrology 148, 471–488.
- Zoheir, B.A., Lehmann , B., 2011. Listvenite-lode association at the Barramiya gold mine, Eastern Desert, Egypt. Ore Geology Reviews, 39, 101-115.

# Paper I

# The extent and conditions of alteration surrounding the Tarr carbonatite-albitite complex, Sinai Peninsula, Egypt

**AHMAD BOSKABADI[1], IAIN K. PITCAIRN[1], ROBERT J. STERN[2], MOKHLES K. AZER[3], CURT BROMAN[1], FATHY H. MOHAMED[4]**

*(1) Department of Geology and Geochemistry, Stockholm University, Stockholm, Sweden*
*(2) Geosciences Department, University of Texas at Dallas, Texas, USA*
*(3) Geology Department, National Research Centre, Cairo, Egypt*
*(4) Geology Department, Faculty of science, Alexandria University, Alexandria, Egypt*

**Abstract**

Carbonate dykes occurring in the Arabian-Nubian Shield (ANS) are clearly intrusive in origin and classify as carbonatites according to the IUGS classification, yet previous investigations refer to them as "intrusive carbonates" rather than carbonatites, due mainly to their low Sr, Ba, Nb, Y, Th and REE contents. The Tarr carbonatite albitite complex (TCA) in SE Sinai, Egypt contains a series of small (<1.2 km wide) albitite intrusions surrounded by small veins and dykes of carbonatite, which occur predominantly in a narrow zone of brecciation surrounding the intrusions. Fennitic alteration surrounding the TCA has been reported but there is little consensus on the extent and style of this alteration. We use mineralogy and chemical composition of the albitite, carbonatite and altered country rocks as well as fluid inclusion and thermometry data from the carbonatites to investigate the extent of fennitisation surrounding the TCA and the conditions under which the carbonatite emplacement and related alteration occurred.

Fennitic alteration surrounding the TCA carbonatites is not abundant in the areas investigated in this study. Alteration is dominated by precipitation of carbonatite in the breccia zone surrounding the albitite with spatially associated actinolite, chlorite, sericite and epidote. Geochemical trends are consistent with addition of carbonate and associated secondary minerals with altered rocks containing higher CaO, MgO, $Fe_2O_3$ and MnO and lower $SiO_2$, $Al_2O_3$, $Na_2O$ and $K_2O$ values compared to their unaltered end member compositions. Pervasive alkali metasomatism of country rocks has previously been reported in the TCA implying that the extent of this alteration is spatially variable and most likely lithologically controlled. Fluid inclusion investigations show that the carbonatite magma contained a high-salinity $H_2O$-$CO_2$-NaCl-$CaCl_2$ fluid that most likely caused the fennitisation previously reported in some areas.

The crystallisation conditions of the carbonatite dykes and carbonatite matrix in the breccia zones have been constrained using Zr-in-rutile thermometry and fluid inclusion microthermometry. Crystallisation of the carbonatite in the dykes and the breccia zone occurred between 565±38°C and 420°-480°C, and at 0.75 to 1.3 kbar which corresponds to a depth of 2.8-4.9 km. Rutile hosted within the carbonatite crystallised early at 565±38°C and the carbonate itself crystallised later after cooling to around 420°-480°C. Our data support the model proposed by Azer et al (2010) of immiscibility of a carbonatite and albitite melts in a shallow-level cupola culminating in explosive emplacement of the albitite breccia and carbonatite.

**Keywords**

Carbonatite, Fennitisation, Wadi Tarr, Albitite, Zr-in-rutile thermometry

## 1. Introduction

The migration of carbonate-rich solutions was common during deformation and metamorphism of the Arabian-Nubian Shield (ANS), forming veins and dykes, and causing diffuse and pervasive carbonation of a wide range of basement rocks (Stern and Gwinn, 1990). The carbonate dykes are clearly intrusive, contain more than 50% carbonate minerals and thus classify as carbonatites according to the International Union of Geological Sciences (IUGS) classification (Le Maitre, 2002), yet much of the literature describing intrusive carbonates in the ANS refer to them as "intrusive carbonates" rather then carbonatites, due mainly to their low Sr, Ba, Nb, Y, Th and REE contents compared to "classic" carbonatites (Bogoch et al. 1986; Stern and Gwinn, 1990; Blasy et al. 2001; Azer et al. 2010). The association between carbonatites and REE-enrichment is well known; carbonatite rocks currently represent one of world's major REE resources (Hornig-Kjarsgaard, 1998). Some previous studies have suggested that carbonatites should contain Sr, REE and Ba contents in excess of 700, 500 and 250 ppm respectively (Le Bas, 1981; Samoilov, 1991). However, carbonatites with low trace element contents are not uncommon particularly those with a magnesian, dolomite-rich affinity (e.g. Andersen 1986; Harmer et al. 1998; Hornig-Kjarsgaard, 1998; Halama et al. 2005; Brady and Moore, 2012). The low trace element concentrations in these rocks is an interesting feature that may aid interpretation of their origin and emplacement conditions (Brady and Moore, 2012).

Global compilations of the diversity and abundance of silicate rocks associated with carbonatites, show a common spatial association with a specific suite of alkaline silicate rocks including nephenlinites, ijolites, phonolites, lamprophyres, trachyte and syenites, but also that at 24% of localities carbonatites were found to occur with no associated igneous silicate rocks (Woolley and Kjarsdgaard, 2008). The relationship between carbonatite and associated silicate rocks, should they occur, is key to understanding the petrogenesis of carbonate complexes (Moore et al. 2009). Another characteristic feature of carbonatite complexes is the occurrence of fennitic alteration; alkali metasomatism associated with alkali-silicate and carbonatite igneous activity (Le Bas, 2008). The extent and style of fennitisation associated with carbonatite complexes is highly variable and in many cases the exact relationship between the fennitic alteration, the alkali silicate and carbonatite magmatism is unclear (Heinrich, 1985; Le Bas, 2008).

The Tarr carbonatite albitite complex (TCA) in SE Sinai, Egypt is the only carbonatite in the ANS occurring with an associated alkaline igneous intrusion. Most other ANS carbonatites are reported to occur as veins or dykes intruding calc-alkaline metavolcanic rocks (Stern, 1981). The TCA contains a series of small (<1.2 km wide) albitite intrusions surrounded by small veins and dykes of carbonatite which occur predominantly in a narrow zone of brecciation surrounding the intrusions (Shimron, 1975; Bogoch et al. 1984; Blasy et al. 2001; Azer et al. 2010). Although a number of different origins for the carbonatite have been proposed including remobilised carbonate sediments and carbonate produced by metamorphism of serpentinites, stable and radiogenic isotope analyses indicate a mantle source (Bogoch et al. 1986; Azer et al. 2010). Fennitic alteration has been reported but there is little consensus on the extent and style of this alteration (Shimron, 1975; Bogoch et al. 1987). Shimron (1975) reports a zone of fennitisation up to a few hundred m wide occurring outside the breccia zone that surrounds the albitite, whereas Bogoch et al. (1987) propose that the albitite body itself is the result of fennitisation from a carbonatite that lost its alkalinity during crystallisation and cooling. The extent of fennitic alteration at Tarr, the conditions under which it occurred and the relationship between this alteration and the albitite and carbonatite are not well known.

We present a re-evaluation of the TCA and use mineralogy and chemical composition of the albitite, carbonatite and altered country rocks to investigate the extent and style of fennitisation surrounding the TCA. We also present new fluid inclusion and thermometry data from the carbonatites in order to constrain the conditions under which the carbonatite emplacement and related alteration occurred.

## 2. Geological setting

The TCA occurs in the southernmost part of the Wadi Kid metamorphic core complex, one of the four main Neoproterozoic metamorphic belts in the Sinai Peninsula (Fig. 1; Blasband et al. 1997; 2000; Brooijmans et al. 2003; Fowler et al. 2010). Metamorphic grades of the Wadi Kid metasedimentary and metavolcanic rocks range from lower-greenschist to amphibolite facies with a general increase in grade towards the north (Shimron, 1980; Khalaf, 2004). The TCA is hosted by the Tarr formation, a volcano-sedimentary succession with late Proterozoic intrusive rocks that occurs in the southern parts of Wadi Kid (Khalaf, 2004). Volcanic rocks of this area include pyroclastic rocks and lavas of andesitic to rhyolitic composition of the Heib and Tarr formation and metasedimentary rocks mostly consist of metamorphosed mudstones, sandstones, conglomerates and carbonates (Shimron, 1975). Zircon from a Heib formation rhyolite clast defines a $^{206}Pb/^{238}U$ weighted mean age of 609±5 Ma, which is taken to approximate the age of Heib and Tarr formation (Moghazi et al. 2012).

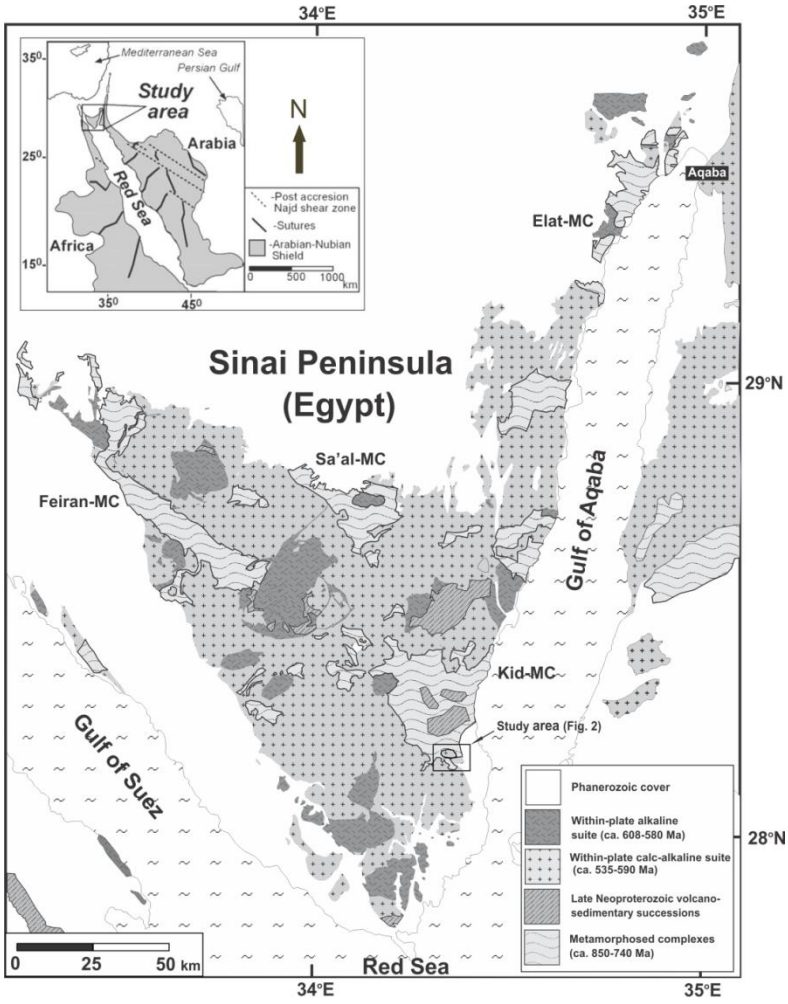


**Fig. 1** Simplified geological map of Neoproterozoic basement in Sinai (after Eyal et al. 1980; Bentor & Eyal 1987 and Be'eri-Shlevin et al. 2009) showing the location of detailed study area (Fig. 2). Inset shows the location of the Sinai in the northernmost exposures of eastern Africa and western Arabia (dark grey).

The TCA occurs as a series of irregular-shaped intrusive bodies scattered over a 10 $km^2$ area in the SE part of Wadi Kid, with the largest body occurring in Wadi Tarr (Fig. 2). The albitite is a white to pale yellow leucocratic rock consisting of up to 90% albite with minor quartz and orthoclase, and accessory biotite, zircon, and titanite (Azer et al. 2010). Medium-grained equigranular and fine-grained porphyritic textures

both occur and are interpreted to indicate hypabyssal and volcanic components of the intrusion (Azer et al. 2010). U-Pb SIMS dating of zircons from the albitite yield ages of 605 ± 13 Ma (Azer et al. 2010), similar to A-type granites in the Wadi Kid region (Be'eri-Schlevin et al. 2009, Ali et al. 2009, Moghazi et al. 2012). The country rocks immediately surrounding the albitites are dominated by pyroclastic rocks and metasedimentary rocks metamorphosed up to greenschist facies (Fig. 2). A zone of brecciation that affects the albitite and the hosting volcanic rock surrounds the albitite intrusions. The carbonatites occur within the breccia zones surrounding the albitites as small dyke-like bodies commonly <1m but up to 10m wide in places. They are coarsely crystalline and consist dominantly of dolomite and breunnerite with minor calcite in places. The dolomite varies in grain size from < 0.5 cm to > 4cm wide with the larger grains appearing as phenocrysts that are locally zoned (Azer et al. 2010). Breunnerite contains secondary Fe-oxides and cross cuts the dolomite in places. Olivine dolerite and lamprophyre dykes also occur mainly within or near the breccia zone surrounding the albitite intrusion (Shimron, 1975; Bogoch and Magaritz, 1983; Azer et al. 2010). The commonly occur as swarms of parallel bodies but can be irregularly shaped with variable dip and orientation, and are reported to contain abundant dolomite rich ocelli (Bogoch and Margitz, 1983).

## 3. Sampling:

The original aim of this study was to investigate the occurrence of fennitic alteration surrounding the TCA and for this purpose, samples of albitite, breccia zone, intrusive carbonates and country rocks were collected along two main transects; the Northern Transect and Wadi Khashm El-Fakh. Further samples were collected from carbonatite and surrounding rocks near the quarry office (Fig. 2).

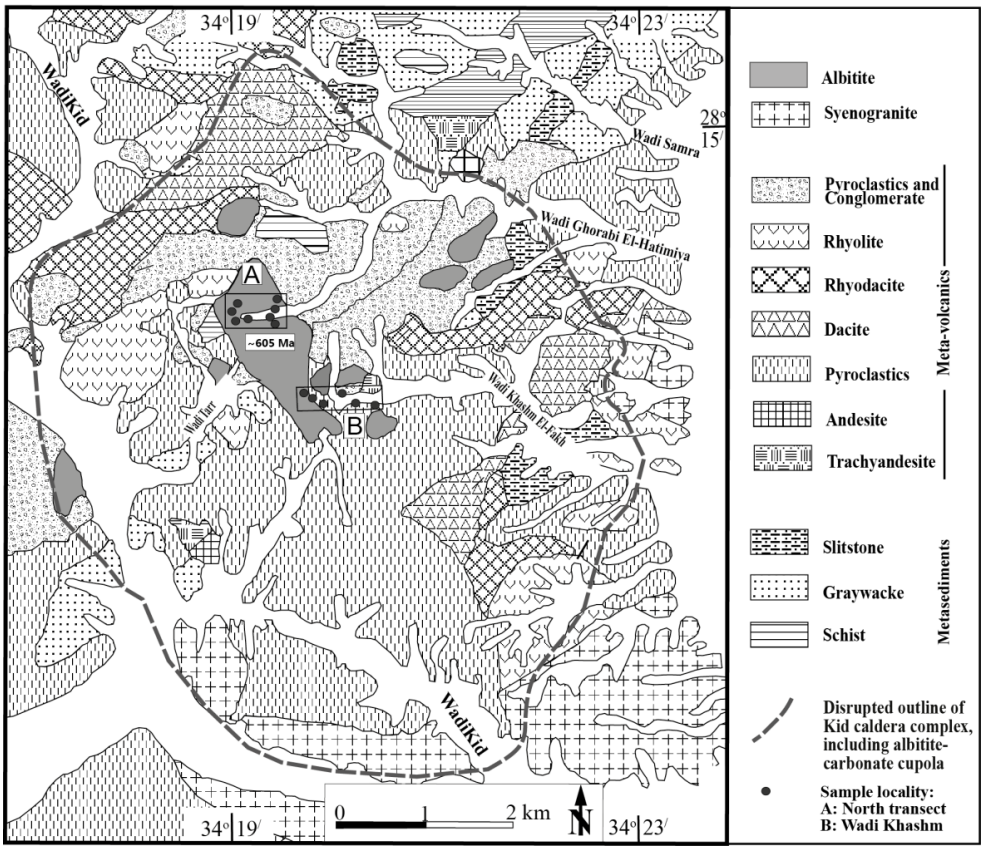


**Fig. 2** Geological map of the Wadi Tarr area (after Blasy et al. 2001 and Azer et al. 2010) and sample localities: **(a)** North Transect and **(b)** Wadi Khashm El-Fakh.

The Northern transect area is actually located inside the main Tarr albitite pluton according to previous maps (Fig. 2). In this area dominantly volcanic country rock is surrounded by irregularly shaped patches of albitite (Fig. 3a). The country rock comprises pyroclastic volcanic rocks and cordierite bearing metasedimentary rocks (Fig. 3a). Two patches of coarse dolerite-like rock also occur, most likely as irregularly orientated dykes although contacts with surrounding rocks were not exposed (Fig. 3a). The contact between the albitite and country rocks is sharp (Fig. 3b) and is characterized by a roughly 20 m wide zone of brecciation both hosted by the albitite and the volcanic country rock (Fig. 3c). Systematic sampling of the same lithology outwards from the albitite was not possible due to the variability of exposure of country rock lithologies and the irregular nature of the albitite-country rock contact (Fig. 3a).

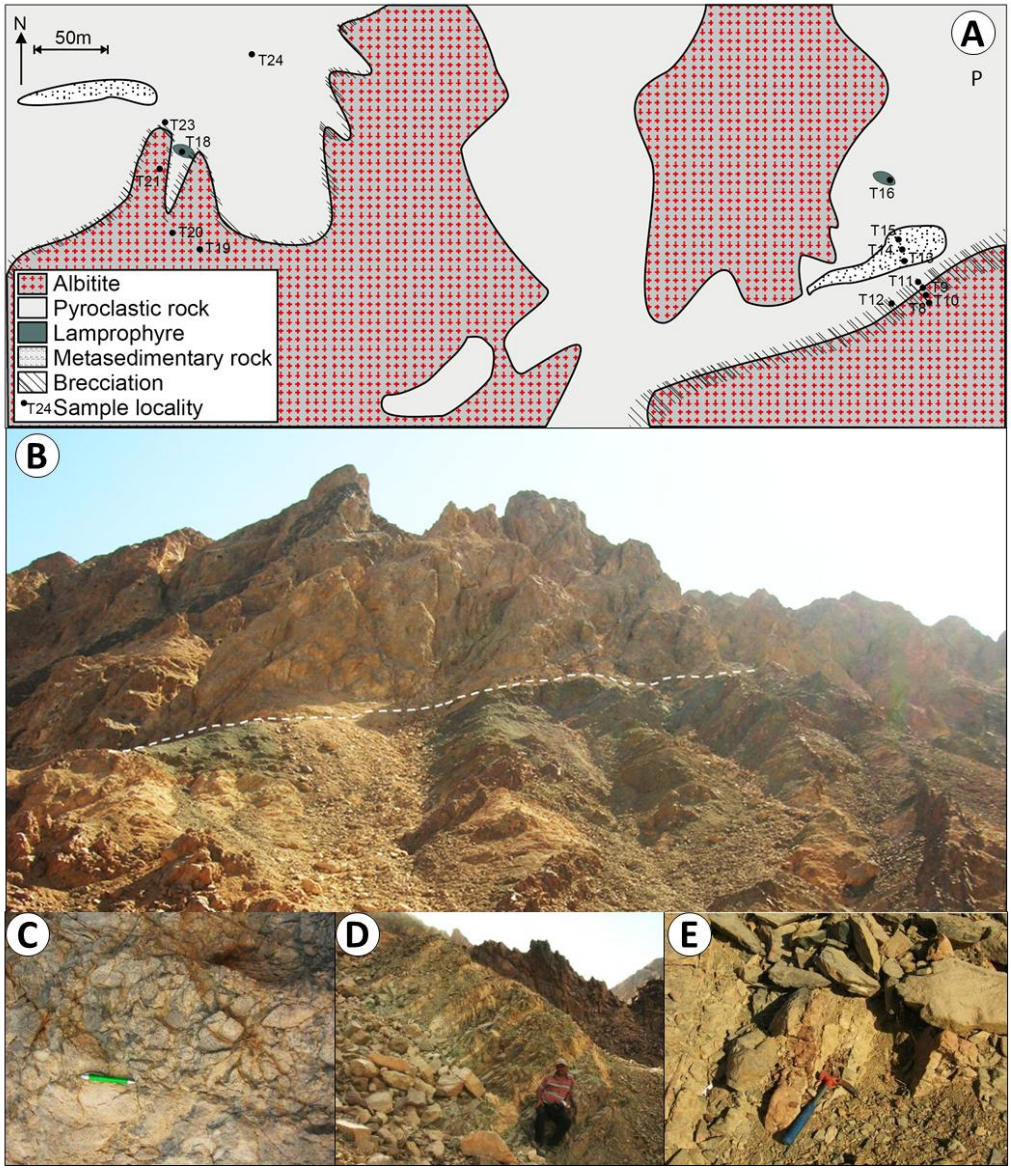


**Fig. 3 (a)** Schematic geological map of the northern transect area showing sampling localities**.** Not all albitite-country rock contacts were investigated for brecciation, **(b)** the contact between the main albitite body and volcanic country rock in the Northern Transect. Photo taken looking south from position P in figure 3a; **(c)** albitite breccia clasts in dark green actinolite matrix from the northern transect; **(d)** veins of albitite in metasedimentary country rocks, northern transect; **(e)** carbonatite dyke from the Quarry locality.

Wadi Khashm El-Fakh displays similar features to those observed in the Northern transect. The sharp contact between the albitite and the country rock is brecciated and the country rock is variable in composition including pyroclastic rocks and metasedimentary rocks (Table 1). Coarse dolerite-like rock is also observed occurring here as thin (1m) wide dykes distal (300m from the albitite contact; Table 1).

## 4. Analytical Methods:

The mineralogy of polished thin sections was investigated by petrographic microscopy and using a Philips XL30 FEG environmental scanning electron microscope (ESEM) at the Department of Geological Sciences, Stockholm University, operating at 20 kv and equipped with OXFORD energy dispersive analytical X-ray spectrometer.

Concentrations of Ti, Zr and other trace elements (Al, Si, Ca, Nb, Ti, La, Ce, V and Cr) in rutile were measured by field emission electron probe microanalyser (FE-EPMA), JXA-8530F JEOL HYPERPROBE, equipped with four wavelength dispersive spectrometers (WDS), secondary (SE), backscattered electron detectors (BSE) and energy dispersive spectrometer (EDS) at Department of Earth Sciences, Uppsala University, Sweden. The instrument set-up described by Zack et al. (2004) was used although the beam current and counting time were increased so that the peak-background position was accordingly optimized for a better analysis. Accelerating voltage was 20 kV with 100 nA beam current and 5 μm beam spot. Counting times for Zr, Nb and Ti were 200s and for Cr and Fe were 10s. Spectroscopic crystals for Zr, Ti, Nb, Cr, and Fe were PETH, PETJ, LIFJ, and LIFJ, with respective detection limits of 8, 49, 29, 27 and 26 ppm, respectively. PAP corrections were applied.

Powdered samples were analysed for major elements using ZSX Rigaku Primus II X-ray Fluorescence spectrometer at Geological Sciences Department, Stockholm University. The XRF analyses were carried out on fused-glass discs (flux-to-sample ratios of 5:2) for major elements. The same powdered samples were also analysed for trace elements by inductively coupled plasma mass spectrometry (ICP-MS) after lithium metaborate/tetraborate fusion at activation laboratories Ltd. (Actlabs), Canada. Precision and accuracy was controlled by analysis of International reference materials and replicate analyses and are 1% for major elements and 2% to 10% for trace elements.

Analyses of fluid inclusions of intrusive dolomite, breunnerite and recrystallised carbonates were carried out at the Department of Geological Sciences, Stockholm University. Fluid inclusions were studied in doubly polished 150 μm thick sections. Microthermometric analyses on fluid inclusions in the carbonates were made with a Linkam THM 600 stage mounted on a Nikon microscope utilising a 40x long working-distance objective. The working range of the stage is from -196° to +600°C. The thermocouple readings were calibrated by means of SynFlinc synthetic fluid inclusions and well-defined natural inclusions in Alpine quartz. The reproducibility was ±0.1°C for temperatures below 40°C and ±0.5°C for temperatures above 40°C.

**Table 1** Whole chemical composition of different rock types in Wadi Tarr area

| Lithology | Albitite | | | Albitite | | | | Carbonatite | | | | | Lamprophyre | | |
|---|---|---|---|---|---|---|---|---|---|---|---|---|---|---|---|
| | Fresh | | | Brecciated | | | | Dolomite/Breunnerite | | | Dolomite[b] | Breunnerite[b] | | | |
| Sample | T7 | T19 | T20 | T8 | T23 | T36 | T37 | T25 | T26[a] | T27 | 100C | 200C | T16 | T18 | T33 |
| Transect | WK | NT | NT | NT | NT | WK | WK | WK | WK | WK | _ | _ | NT | NT | WK |
| $SiO_2$ (wt%) | 67.1 | 67.3 | 67.7 | 63.5 | 63.5 | 70.0 | 72.0 | 0.7 | 27.6 | 3.5 | 0 | 0 | 47.3 | 49.4 | 54.0 |
| $Al_2O_3$ | 19.4 | 19.5 | 19.6 | 17.1 | 18.1 | 16.0 | 15.9 | 0.0 | 0.5 | 0.7 | 0.15 | 0.57 | 16.4 | 16.5 | 13.4 |
| CaO | 0.9 | 0.6 | 0.4 | 4.2 | 3.7 | 1.4 | 0.6 | 15.1 | 27.6 | 15.8 | 26.8 | 12.4 | 8.6 | 7.7 | 8.5 |
| MgO | 0.0 | 0.0 | 0.1 | 2.8 | 3.1 | 0.4 | 0.2 | 29.0 | 8.6 | 26.5 | 22.2 | 30.7 | 6.9 | 5.7 | 8.0 |
| MnO | 0.0 | 0.0 | 0.0 | 0.0 | 0.0 | 0.0 | 0.0 | 0.2 | 0.2 | 0.3 | 0.47 | 0.25 | 0.1 | 0.2 | 0.2 |
| $P_2O_5$ | 0.4 | 0.2 | 0.0 | 0.9 | 0.1 | 0.1 | 0.1 | 0.0 | 0.1 | 0.1 | 0 | 0.05 | 0.3 | 0.2 | 0.3 |
| $Fe_2O_3$ | 0.3 | 0.3 | 0.4 | 1.4 | 1.0 | 0.4 | 0.4 | 9.7 | 4.7 | 11.5 | 4.58 | 12.8 | 13.6 | 12.5 | 7.8 |
| $Na_2O$ | 11.3 | 11.4 | 11.2 | 9.4 | 9.5 | 8.8 | 8.9 | 0.0 | 0.0 | 0.0 | 0.01 | 0.04 | 3.6 | 3.7 | 3.9 |
| $K_2O$ | 0.1 | 0.1 | 0.2 | 0.1 | 0.1 | 0.1 | 0.2 | 0.0 | 0.0 | 0.0 | 0.05 | 0.05 | 1.0 | 0.8 | 1.1 |
| $TiO_2$ | 0.3 | 0.3 | 0.3 | 0.3 | 1.0 | 0.3 | 0.2 | 0.0 | 0.0 | 0.0 | 0 | 0.02 | 2.1 | 2.0 | 1.2 |
| LOI | _ | _ | _ | _ | _ | 1.4 | 0.5 | 45.8 | 30.8 | 41.6 | 45.8 | 43.1 | _ | 2.0 | 1.9 |
| Total | 99.9 | 99.9 | 99.9 | 99.9 | 99.9 | 98.8 | 99.0 | 100.1 | 100.1 | 100.1 | 100 | 100 | 99.8 | 100.7 | 100.1 |
| V (ppm) | 18 | 24 | 27 | 53 | 70 | 16 | 13 | 79 | 89 | 150 | 44 | 94 | 332 | 233 | 204 |
| Cr | 40 | 50 | 50 | 90 | 100 | 80 | 100 | 40 | 80 | 30 | 112 | 89 | 110 | 40 | 100 |
| Co | 1 | 2 | 8 | 3 | 2 | 2 | 2 | 11 | 4 | 14 | _ | _ | 50 | 55 | 31 |
| Ni | 20 | 20 | 20 | 20 | 30 | 20 | 20 | 120 | 100 | 180 | 37 | 167 | 70 | 70 | 40 |
| Cu | 10 | 10 | 10 | 10 | 10 | 10 | 10 | 10 | 10 | 10 | _ | _ | 100 | 50 | 10 |
| Zn | 30 | 30 | 30 | 30 | 30 | 70 | 30 | 30 | 30 | 30 | _ | _ | 30 | 130 | 30 |
| Ga | 25 | 26 | 27 | 23 | 15 | 21 | 19 | 1 | 1 | 1 | 0 | 1 | 19 | 23 | 17 |
| Rb | 2 | 2 | 3 | 2 | 2 | 2 | 3 | 2 | 2 | 2 | 0 | 1 | 40 | 12 | 31 |
| Sr | 104 | 98 | 115 | 122 | 89 | 93 | 116 | 100 | 170 | 257 | 237 | 109 | 475 | 673 | 273 |
| Y | 35 | 31 | 18 | 87 | 19 | 21 | 18 | 12 | 4 | 7 | 26 | 2 | 20 | 20 | 28 |
| Zr | 374 | 335 | 343 | 306 | 190 | 273 | 258 | 6 | 9 | 12 | 5 | 7 | 136 | 118 | 142 |
| Nb | 14 | 34 | 32 | 17 | 11 | 18 | 19 | 1 | 1 | 1 | 0 | 1 | 8 | 15 | 11 |
| Ba | 37 | 42 | 52 | 22 | 16 | 28 | 40 | 6 | 11 | 17 | 31 | 39 | 414 | 372 | 122 |
| Hf | 8.4 | 7.8 | 8.0 | 6.7 | 4.6 | 6.8 | 6.6 | 0.2 | 0.2 | 0.2 | _ | _ | 3.0 | 3.0 | 3.6 |
| Tl | 0.1 | 0.1 | 0.1 | 0.1 | 0.1 | 0.1 | 0.1 | 0.1 | 0.1 | 0.1 | _ | _ | 0.2 | 0.1 | 0.1 |
| Pb | 5.0 | 5.0 | 5.0 | 5.0 | 5.0 | 5.0 | 5.0 | 5.0 | 5.0 | 5.0 | _ | _ | 5.0 | 5.0 | 5.0 |
| Th | 4.7 | 10.7 | 9.1 | 6.7 | 6.5 | 6.3 | 5.4 | 0.1 | 0.3 | 0.3 | 2 | 1 | 1.0 | 1.5 | 2.9 |
| U | 1.0 | 1.5 | 1.5 | 1.0 | 1.9 | 1.3 | 1.4 | 0.3 | 0.2 | 0.3 | _ | _ | 0.5 | 0.4 | 2.4 |
| REEs (ppm) | | | | | | | | | | | | | | | |
| La | 17 | 52 | 45 | 67 | 16 | 44 | 28 | 1.3 | 2.1 | 1.5 | 18.6 | 0.5 | 11 | 14 | 13 |
| Ce | 40 | 112 | 93 | 143 | 34 | 88 | 62 | 5.8 | 4.2 | 3.8 | 46.8 | 1.2 | 29 | 31 | 32 |
| Pr | 5.5 | 14 | 11 | 19 | 4.3 | 11 | 7.9 | 1.3 | 0.6 | 0.6 | 5.6 | 0.2 | 4.3 | 4.3 | 4.9 |
| Nd | 24 | 54 | 42 | 80 | 16 | 41 | 32 | 7.8 | 2.7 | 2.9 | 24.0 | 1.2 | 20 | 19 | 23 |
| Sm | 5.7 | 9.1 | 6.1 | 19.0 | 3.1 | 7.0 | 5.4 | 3.3 | 0.7 | 1.0 | 4.7 | 0.5 | 4.7 | 4.5 | 5.8 |
| Eu | 1.4 | 1.7 | 0.9 | 4.8 | 1.0 | 1.4 | 1.1 | 1.6 | 0.2 | 0.3 | 1.7 | 0.1 | 1.7 | 1.6 | 2.7 |
| Gd | 5.7 | 6.8 | 3.7 | 19.0 | 2.6 | 4.9 | 3.6 | 3.3 | 0.8 | 1.1 | 4.3 | 0.6 | 4.5 | 4.3 | 5.8 |
| Tb | 1.0 | 1.0 | 0.5 | 3.2 | 0.4 | 0.7 | 0.5 | 0.5 | 0.1 | 0.2 | 0.6 | 0.1 | 0.7 | 0.7 | 0.9 |
| Dy | 6.1 | 5.6 | 2.7 | 18.1 | 2.8 | 3.7 | 3.0 | 3.0 | 0.7 | 1.1 | 3.6 | 0.6 | 4.2 | 3.9 | 5.2 |
| Ho | 1.2 | 1.1 | 0.6 | 3.2 | 0.6 | 0.7 | 0.6 | 0.5 | 0.1 | 0.2 | 0.7 | 0.1 | 0.8 | 0.7 | 1.0 |
| Er | 3.5 | 3.4 | 2.0 | 8.6 | 2.2 | 2.2 | 1.9 | 1.2 | 0.4 | 0.6 | 1.7 | 0.3 | 2.2 | 2.0 | 2.7 |
| Tm | 0.5 | 0.5 | 0.3 | 1.2 | 0.4 | 0.4 | 0.3 | 0.2 | 0.1 | 0.1 | 0.3 | 0.1 | 0.3 | 0.3 | 0.4 |
| Yb | 3.6 | 3.4 | 2.4 | 6.9 | 2.7 | 2.6 | 2.3 | 1.3 | 0.7 | 1.1 | 1.7 | 0.5 | 2.1 | 1.7 | 2.7 |
| Lu | 0.6 | 0.6 | 0.5 | 1.0 | 0.5 | 0.4 | 0.4 | 0.2 | 0.2 | 0.2 | 0.3 | 0.1 | 0.3 | 0.3 | 0.4 |
| ∑REE | 116 | 265 | 211 | 393 | 87 | 208 | 148 | 31 | 14 | 15 | 114 | 6 | 86 | 89 | 101 |
| (Eu/Eu*)n | 0.74 | 0.62 | 0.55 | 0.77 | 1.09 | 0.69 | 0.71 | 1.42 | 0.86 | 0.84 | 1.16 | 0.82 | 1.10 | 1.11 | 1.42 |
| (La/Lu)n | 2.90 | 9.31 | 10.4 | 6.81 | 3.68 | 10.4 | 7.19 | 0.64 | 1.45 | 0.68 | 7.89 | 0.52 | 3.55 | 5.23 | 3.09 |
| (La/Sm)n | 1.83 | 3.57 | 4.63 | 2.20 | 3.28 | 3.93 | 3.20 | 0.25 | 1.87 | 0.94 | 2.56 | 0.65 | 1.50 | 1.96 | 1.41 |
| (Gd/Lu)n | 1.17 | 1.45 | 1.02 | 2.30 | 0.70 | 1.38 | 1.11 | 1.94 | 0.66 | 0.59 | 2.10 | 0.78 | 1.69 | 1.90 | 1.63 |

NT-North Transect, WK-Wadi Khashm Transect.

[a] Altered carbonate.

[b] Data from Azer et al. 2010.

**Table 1** Continued

| Lithology | Volcanic (pyroclastics) | | | Volcanic (pyroclastics) | | | | | | | | | | Metasedimentary | | |
|---|---|---|---|---|---|---|---|---|---|---|---|---|---|---|---|---|
| | Fresh | | | Brecciated | | | | | | | | | | Cordierite-schist | | |
| Sample | T28 | T34 | T41 | T9 | T10 | T11 | T12 | T21 | T24 | T30 | T35 | T38 | T40 | T13 | T14 | T15 |
| Transect | NT | WK | WK | NT | NT | NT | NT | NT | NT | WK | WK | WK | WK | NT | NT | NT |
| $SiO_2$ (wt%) | 64.5 | 61.9 | 63.4 | 62.1 | 57.9 | 55.2 | 57.6 | 70.0 | 64.1 | 60.2 | 60.6 | 61.1 | 61.8 | 62.5 | 61.5 | 60.1 |
| $Al_2O_3$ | 17.1 | 16.5 | 16.8 | 15.7 | 13.0 | 15.9 | 15.0 | 16.6 | 16.8 | 16.0 | 16.7 | 16.2 | 17.2 | 16.3 | 16.6 | 15.8 |
| CaO | 0.9 | 1.9 | 2.6 | 4.2 | 10.0 | 12.7 | 10.9 | 1.2 | 1.8 | 4.1 | 4.9 | 2.0 | 4.9 | 1.2 | 1.0 | 1.1 |
| MgO | 3.2 | 2.6 | 2.1 | 4.2 | 9.8 | 2.2 | 1.7 | 0.7 | 2.5 | 7.3 | 3.5 | 4.5 | 2.3 | 6.7 | 7.0 | 9.4 |
| MnO | 0.0 | 0.1 | 0.0 | 0.1 | 0.1 | 0.1 | 0.1 | 0.0 | 0.1 | 0.1 | 0.1 | 0.0 | 0.1 | 0.0 | 0.0 | 0.1 |
| $P_2O_5$ | 0.2 | 0.2 | 0.1 | 0.2 | 0.2 | 0.3 | 0.3 | 0.1 | 0.2 | 0.1 | 0.3 | 0.2 | 0.2 | 0.2 | 0.2 | 0.2 |
| $Fe_2O_3$ | 5.1 | 7.2 | 5.2 | 5.8 | 3.0 | 4.6 | 6.4 | 2.3 | 6.2 | 6.2 | 7.1 | 5.5 | 5.3 | 7.1 | 7.9 | 8.8 |
| $Na_2O$ | 6.8 | 4.8 | 7.6 | 6.0 | 5.0 | 6.7 | 4.9 | 8.2 | 3.3 | 3.4 | 3.9 | 8.0 | 5.5 | 2.9 | 1.6 | 0.5 |
| $K_2O$ | 1.3 | 3.8 | 1.4 | 0.9 | 0.2 | 1.0 | 2.0 | 0.6 | 4.0 | 1.7 | 1.6 | 1.3 | 1.8 | 1.9 | 3.1 | 3.2 |
| $TiO_2$ | 0.8 | 0.8 | 0.6 | 0.8 | 0.8 | 1.1 | 1.0 | 0.3 | 0.9 | 0.7 | 1.1 | 0.9 | 0.7 | 0.9 | 0.9 | 0.9 |
| LOI | _ | _ | _ | _ | _ | _ | _ | _ | _ | _ | _ | _ | _ | _ | _ | _ |
| Total | 99.9 | 99.8 | 99.9 | 99.9 | 99.9 | 99.8 | 99.9 | 99.9 | 99.8 | 99.9 | 99.8 | 99.9 | 99.9 | 99.9 | 99.9 | 99.9 |
| V (ppm) | 113 | 118 | 105 | 107 | 145 | 88 | 113 | 8 | 99 | 109 | 125 | 151 | 140 | 151 | 151 | 162 |
| Cr | 120 | 110 | 100 | 130 | 100 | 40 | 30 | 70 | 80 | 110 | 130 | 130 | 110 | 120 | 100 | 100 |
| Co | 7 | 17 | 16 | 22 | 22 | 12 | 10 | 3 | 19 | 18 | 22 | 12 | 16 | 24 | 22 | 22 |
| Ni | 40 | 40 | 30 | 80 | 80 | 20 | 20 | 20 | 30 | 40 | 50 | 40 | 20 | 80 | 80 | 60 |
| Cu | 10 | 10 | 10 | 30 | 200 | 660 | 310 | 10 | 60 | 10 | 20 | 10 | 10 | 10 | 10 | 10 |
| Zn | 30 | 30 | 30 | 30 | 30 | 60 | 50 | 30 | 50 | 30 | 60 | 30 | 30 | 30 | 30 | 40 |
| Ga | 21 | 20 | 16 | 19 | 15 | 14 | 16 | 21 | 22 | 18 | 21 | 20 | 22 | 20 | 21 | 19 |
| Rb | 28 | 87 | 21 | 18 | 3 | 31 | 68 | 15 | 121 | 39 | 40 | 41 | 38 | 47 | 61 | 63 |
| Sr | 93 | 171 | 237 | 458 | 114 | 133 | 94 | 293 | 222 | 152 | 575 | 88 | 495 | 93 | 59 | 51 |
| Y | 19 | 20 | 17 | 13 | 20 | 16 | 17 | 20 | 29 | 18 | 17 | 18 | 22 | 23 | 22 | 21 |
| Zr | 209 | 151 | 104 | 151 | 123 | 137 | 144 | 304 | 251 | 176 | 189 | 169 | 116 | 172 | 173 | 160 |
| Nb | 10 | 7 | 6 | 6 | 7 | 9 | 8 | 24 | 15 | 9 | 9 | 6 | 6 | 9 | 8 | 8 |
| Ba | 253 | 710 | 390 | 229 | 125 | 75 | 246 | 152 | 696 | 258 | 528 | 36 | 187 | 143 | 229 | 334 |
| Hf | 5.0 | 3.8 | 2.5 | 3.5 | 3.0 | 3.1 | 3.3 | 6.8 | 6.1 | 4.2 | 4.3 | 4.0 | 2.9 | 4.3 | 4.4 | 3.9 |
| Tl | 0.1 | 0.2 | 0.1 | 0.1 | 0.1 | 0.2 | 0.2 | 0.1 | 0.5 | 0.1 | 0.1 | 0.1 | 0.2 | 0.1 | 0.2 | 0.2 |
| Pb | 5.0 | 5.0 | 5.0 | 11 | 11 | 74 | 11 | 5.0 | 5.0 | 5.0 | 5.0 | 5.0 | 7.0 | 5 | 5 | 5 |
| Th | 6.2 | 5.1 | 2.4 | 3.4 | 4.5 | 3.2 | 3.2 | 5.9 | 9.2 | 5.2 | 3.8 | 4.7 | 2.5 | 4.6 | 4.5 | 4.2 |
| U | 1.8 | 1.8 | 0.9 | 1.4 | 3.2 | 1.7 | 1.3 | 1.8 | 3.1 | 2.0 | 1.6 | 1.9 | 1.8 | 1.5 | 1.5 | 1.8 |
| REEs (ppm) | | | | | | | | | | | | | | | | |
| La | 20 | 19 | 13 | 16 | 17 | 15 | 18 | 29 | 36 | 17 | 21 | 26 | 23 | 4.9 | 8.3 | 11.2 |
| Ce | 43 | 42 | 29 | 36 | 37 | 33 | 40 | 66 | 74 | 37 | 47 | 49 | 46 | 10.9 | 18.2 | 23.5 |
| Pr | 5.4 | 5.4 | 3.6 | 4.7 | 4.7 | 4.6 | 5.3 | 7.5 | 9.3 | 4.8 | 6.1 | 5.5 | 5.7 | 1.5 | 2.5 | 3.2 |
| Nd | 22 | 23 | 15 | 19 | 19 | 20 | 23 | 28 | 37 | 20 | 26 | 20 | 22 | 6.7 | 10.7 | 13.2 |
| Sm | 4.9 | 5.1 | 3.5 | 4.0 | 3.8 | 4.2 | 5.0 | 4.9 | 7.5 | 4.4 | 5.1 | 3.5 | 4.6 | 1.9 | 2.6 | 3.0 |
| Eu | 1.1 | 1.5 | 1.1 | 1.1 | 0.7 | 1.2 | 1.6 | 1.2 | 1.7 | 1.0 | 1.4 | 0.7 | 1.3 | 0.6 | 0.7 | 0.7 |
| Gd | 4.1 | 4.3 | 3.2 | 3.1 | 3.5 | 3.6 | 4.2 | 3.8 | 6.3 | 3.6 | 4.2 | 3.0 | 4.1 | 2.6 | 3.0 | 3.1 |
| Tb | 0.6 | 0.7 | 0.5 | 0.5 | 0.6 | 0.6 | 0.6 | 0.6 | 1.0 | 0.5 | 0.6 | 0.5 | 0.6 | 0.5 | 0.6 | 0.6 |
| Dy | 3.6 | 3.9 | 3.0 | 2.5 | 3.6 | 3.1 | 3.6 | 3.5 | 5.7 | 3.2 | 3.3 | 3.0 | 3.7 | 3.7 | 3.9 | 3.6 |
| Ho | 0.7 | 0.8 | 0.6 | 0.5 | 0.7 | 0.6 | 0.6 | 0.7 | 1.1 | 0.7 | 0.6 | 0.6 | 0.7 | 0.8 | 0.8 | 0.8 |
| Er | 2.3 | 2.3 | 1.8 | 1.4 | 2.2 | 1.8 | 1.7 | 2.3 | 3.2 | 2.0 | 1.7 | 1.9 | 2.1 | 2.5 | 2.6 | 2.4 |
| Tm | 0.4 | 0.4 | 0.3 | 0.2 | 0.3 | 0.3 | 0.2 | 0.4 | 0.5 | 0.3 | 0.3 | 0.3 | 0.3 | 0.4 | 0.4 | 0.4 |
| Yb | 2.6 | 2.5 | 1.9 | 1.3 | 2.3 | 1.9 | 1.6 | 2.6 | 3.1 | 2.4 | 1.6 | 2.2 | 2.2 | 2.8 | 2.8 | 2.6 |
| Lu | 0.5 | 0.4 | 0.3 | 0.2 | 0.4 | 0.3 | 0.3 | 0.5 | 0.5 | 0.4 | 0.3 | 0.4 | 0.3 | 0.5 | 0.5 | 0.4 |
| ∑REE | 110 | 112 | 77 | 91 | 96 | 90 | 105 | 151 | 188 | 98 | 119 | 117 | 117 | 40 | 58 | 69 |
| (Eu/Eu*)n | 0.72 | 0.94 | 1.02 | 0.90 | 0.61 | 0.89 | 1.07 | 0.82 | 0.72 | 0.75 | 0.90 | 0.65 | 0.91 | | | |
| (La/Lu)n | 4.31 | 4.96 | 3.96 | 8.11 | 4.59 | 4.69 | 6.84 | 6.76 | 7.31 | 4.41 | 7.93 | 6.99 | 7.23 | | | |
| (La/Sm)n | 2.49 | 2.34 | 2.25 | 2.56 | 2.76 | 2.22 | 2.22 | 3.73 | 2.99 | 2.41 | 2.62 | 4.57 | 3.12 | | | |
| (Gd/Lu)n | 1.08 | 1.33 | 1.20 | 1.82 | 1.14 | 1.35 | 1.92 | 1.04 | 1.53 | 1.11 | 1.85 | 0.98 | 1.54 | | | |

## 5. Results:

### 5.1. Petrography and mineralogy of the TCA rocks

The albitite occurs as leucocratic, pale yellow to white or grey, fine to medium grained rock. The main albitite body is composed of mostly medium grained rock with equigranular subvolcanic texture (Fig. 4a) whereas at Wadi Khashm El-Fakh and Wadi Ghorabi El Hatimiya, the albitite intrusions are mostly fine-grained, with a sub-porphyritic texture. In both varieties, albite accounts for 90-95% of the mineralogy and is subhedral, highly sodic ($An_{5-10}$) with albite-carlsbad and albite twinning. Quartz (1-5%), orthoclase (<5%), and biotite (<1%) also occur with the latter locally associated with sericite-chlorite alteration. Accessory minerals include apatite, zircon, titanite, monazite, rutile, allanite and xenotime, and secondary sericite, chlorite and Fe-oxides also occur.

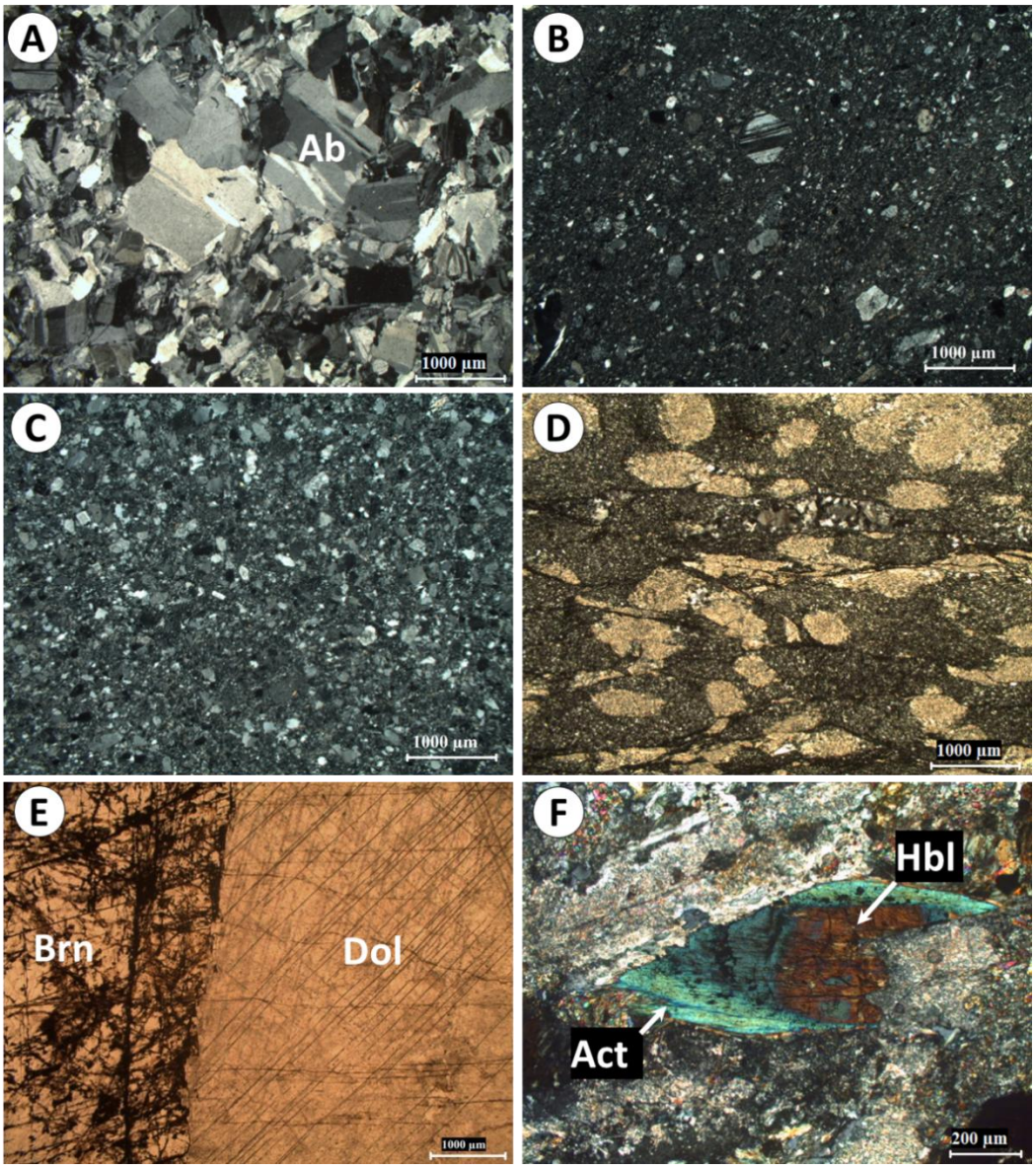


**Fig. 4 (a)** Medium grained albitite with intergranular texture (T7); **(b)** and **(c)** mostly fresh pyroclastic country rocks (T28 and T34); **(d)** mylonitized cordierite schist (T15); **(e)** Tarr carbonatite: dolomite (right) and breunnerite (left) with secondary iron-manganese oxides along cleavages planes and rhomb boundaries (T25); **(f)** highly altered lamprophyre with plagioclase mostly replaced by sericite, epidote and carbonate and primary hornblende replaced by actinolite (T16). Act = actinolite, Ab = albite, Brn = breunnerite, Dol = dolomite, Hbl = hornblende (symbols after kretz, 1983).

The country rock units sampled in this study consist of two lithologies; pyroclastic rocks and cordierite-bearing metasedimentary rocks. The pyroclastic rocks contain phenocrysts and crystal fragments of plagioclase and quartz with minor amount of K-feldspar, biotite, chlorite, sericite and epidote (Fig. 4b, c). They are commonly weakly altered but are unfoliated and appear unaffected by regional metamorphism. The metasedimentary rocks are fine grained and foliated with conspicuous cordierite phenocrysts (Fig. 4d). They consist of cordierite in groundmass of biotite, chlorite, sericite and opaque minerals. These rocks are commonly deformed and metamorphism is interpreted to be part of the Wadi Kid regional overprint that has been previously reported as being greenschist facies in the Tarr area (Shimron, 1975; 1984; Reymer, 1983; Soliman et al. 1992). The volcanic country rocks surrounding Tarr albitite were presumably emplaced after regional metamorphism.

The carbonatites occur as dyke-like bodies, veins and as cement in breccia zones spatially associated with the main albitite body. The carbonatites contain dolomite, breunnerite and rare calcite with accessory apatite, chlorite and iron oxides. The dolomite is white to light grey, mostly coarse to medium-grained aggregate, showing perfect rhombohedral cleavages and sometime pressure twining (Fig. 4e). The breunnerite (ferroan magnesite with 5-50% $FeCO_3$) is dark brown in color and contains dark iron-manganese oxides occurring along cleavage planes and rhombic boundaries, and accessory rutile, sericite, chlorite, and pyrite. The breunnerite-dolomite contact is typically sharp (Fig. 4e).

Coarse grained, dark-green dolerite or lamprophyre dykes occur proximal to the albitite margin, observed in this study to be hosted dominantly in the country rock (Fig. 3a). They comprise phenocrysts of augite and brown hornblende, with calcic plagioclase as lath-shaped phenocrysts and/or as a matrix phase, and minor magnetite, ilmenite and carbonate (Fig. 4f). Carbonate occurs both as globular ocelli and also replacing plagioclase and clinopyroxene. These rocks are similar in composition to those described as olivine dolerites and lamprophyres from the Tarr region (Shimron 1975; Bogoch and Magaritz, 1983), and elsewhere on ANS (Ibrahim et al. 2010; Ibrahim and Ragab, 2011). The mineralogy and textures are similar to lamprophyre rocks but the occurrence of lath-shaped phenocrysts of plagioclase in some samples suggest they do not all classify as lamprophyres. Those with amphibole and clinopyroxene phenocrysts and feldspar as only a matrix phase would as spessartites following the lamprophyre classification of Le Maitre et al. (1989) and Rock (1991). The composition of these dykes is variable but from here onwards they will be referred to as lamprophyres.

The contact between albitite and country rock is sharp and highly brecciated (Fig. 3a, b). Two types of breccia are distinguished; an *interior* albitite-hosted breccia, and an *exterior* volcanic-hosted breccia. Both breccias contains less than 25 percent matrix and are mostly clast supported. The albitite-breccia comprises angular fragments (0.3-10 cm) of pale to pink albitite with matrix of fibrous amphiboles and minor carbonate (Figs. 3c and 5a, 5b). Radiating prismatic actinolite crystals occur together with chlorite, epidote and dolomite forming patches and infilling vugs and cracks in albitite breccia (Fig. 5a, b). Primary biotite has been completely altered to sericite and albite is locally replaced by sericite ± carbonate. The carbonate in albitite-breccia zone is composed of dolomite and calcite, which occurs as cement and fracture-filling together with actinolite and chlorite. The volcanic-breccia consists of angular to sub-angular fragments of pyroclastic rock invaded by veins of carbonate, albite and minor actinolite and epidote (Fig. 5c, d). Carbonates occur as fracture-filling cement or replacing primary feldspars and amphiboles in volcanic country rocks (Fig. 5c, d). Carbonate is more abundant in the volcanic-breccia compared to the albitite-breccia, and within the volcanic-breccia, breunnerite is more abundant than dolomite. Carbonate in both of the breccia zones contains accessory rutile, apatite, iron-oxides, allanite and xenotime (Fig. 5e, f). These

grains occur as clusters surrounded by the carbonated and show subhedral to euhedral textures indicating that they have precipitated from the carbonate-bearing liquid.

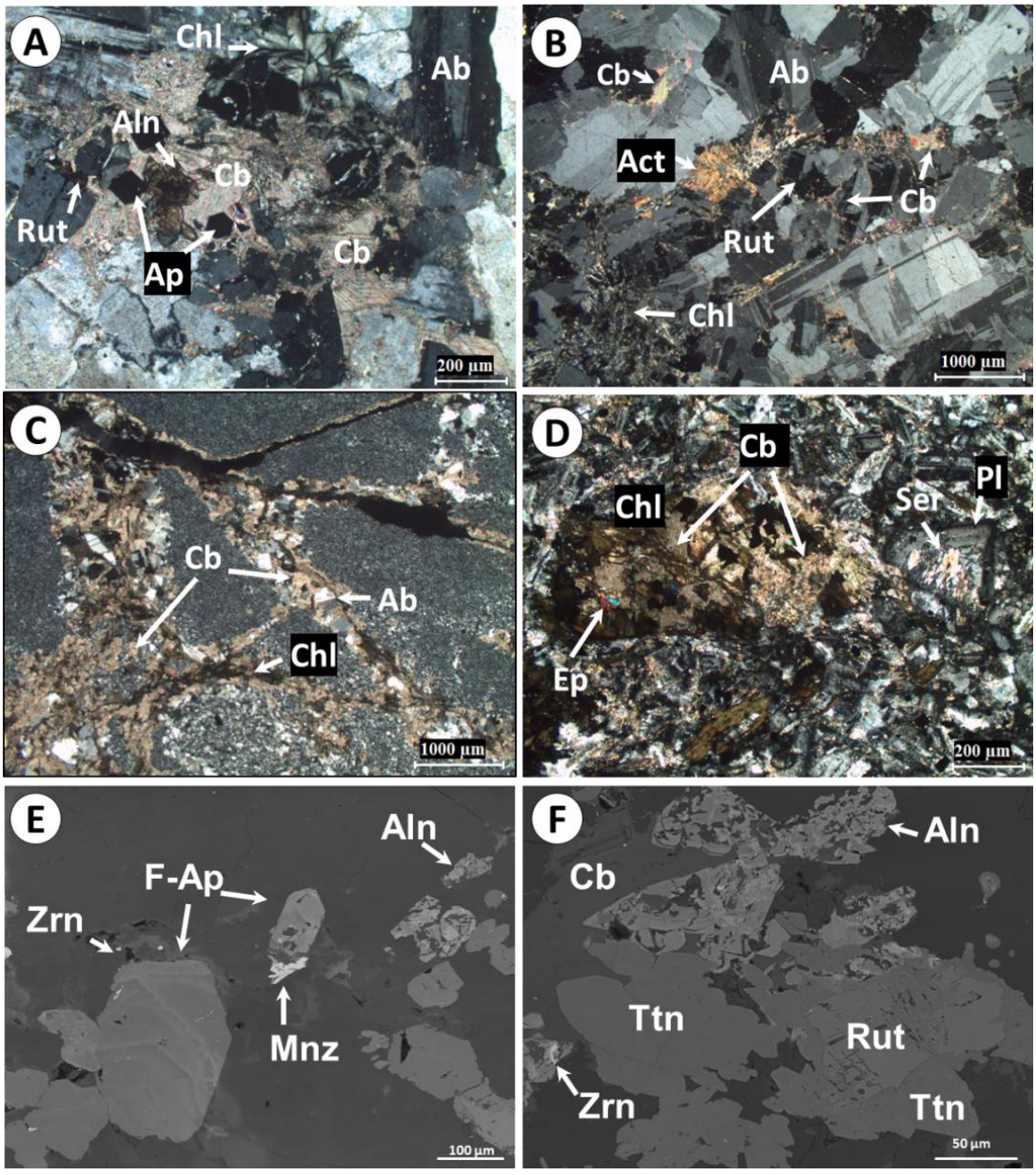


**Fig. 5** Photomicrograph of both albitite and volcanic breccia zones: **(a)** and **(b)** albitite-breccia (T8 and T23), carbonate occurs as cement and fracture-filling together with actinolite, chlorite, apatite, allanite and rutile; **(c)** volcanic-breccia consists of angular to sub-angular fragments of pyroclastic rock invaded by veins of carbonate, albite, minor actinolite and chlorite (T11); **(d)** volcanic-breccia, primary feldspars replaced by carbonate, sericite, chlorite and epidote (T9); **(e)** backscatter image of REE host minerals in albitite breccia (T23) **(f)** backscatter image of zircon, allanite and rutile surrounded by carbonate (mostly dolomite) in albitite breccia (T8). Aln = allanite, Ap = apatite, Cb = carbonate, Chl = chlorite, Ep = epidote, Mnz = monazite, Rut = rutile, Ser = sericite, Zrn = zircon. Other symbols are the same as for Fig. 4.

### 5.2. Geochemistry

The albitite contains 67.1 to 67.7 wt.% $SiO_2$, 19.4 to 19.6 wt.% $Al_2O_3$, and 11.2 to 11.4 wt.% $Na_2O$ (Table 1), similar to the "typical" albitite of Kinnaird and Bowden (1991). Concentrations of all other majors are below 1% (Table 1). The albitite breccia samples generally contain lower $SiO_2$, $Al_2O_3$ and $Na_2O$ and higher CaO, MgO, MnO and $Fe_2O_3$ than the fresh albitite (Table 1). There are no clear differences in minor and trace element concentrations albitite and albitite breccia samples with the exception of breccia sample T8, which has significantly higher LREE and $P_2O_5$ (Table 1).

The least altered pyroclastic rock samples contain 61.9 to 64.5 wt.% $SiO_2$, 16.5 to 17.1 wt.% $Al_2O_3$, 4.8 to 7.6 wt.% $Na_2O$, 5.1 to 7.2 wt.% $Fe_2O_3$, 2.1 to 3.2 wt.% MgO, 1.3 to 3.8 wt.% $K_2O$ and 1 to 2.5 wt.% CaO with all other majors elements being below 1 wt.% (Table 1). In comparison to the albitite they contain lower $Na_2O$, Zr and Nb but higher $K_2O$, $Fe_2O_3$, MgO and MnO, Ba, Rb, Sr, V, Cr, Ni (Table 1). The volcanic breccia samples have more variable compositions than the least altered volcanic country rock, although some samples contain lower $Al_2O_3$ and higher CaO, MgO, $P_2O_5$, $TiO_2$, Cu and Pb (Table 1). The metasedimentary rocks contains 60.1 to 62.5 wt.% $SiO_2$, 15.8 to 16.6 wt.% $Al_2O_3$, 7.1 to 8.8 wt.% $Fe_2O_3$, 6.7 to 9.4 wt.% MgO, 0.5 to 2.9 wt.% $Na_2O$, 1.9 to 3.2 wt.% $K_2O$ and 1 to 1.2 wt.% CaO with all other majors elements being below 1 wt.% (Table 1).

The carbonatite samples analysed in this study contain 21.2 to 29 wt.% MgO, 15.1 to 19.6 wt.% CaO, 9.7 to 15.3 wt.% $Fe_2O_3$, and 0.7 to 4.1 wt.% $SiO_2$ (Table 1). The trace element concentrations are low with <260 ppm Sr, <20 ppm Ba and less than ∑35 ppm REE (Table 1). The samples represent mixtures of dolomite and breunnerite. Representative analyses of dolomitite and breunneritite reported in Azer et al 2010 are also included in Table 1 and these show that dolomitite contains higher CaO, Sr, Y and REE and lower $Fe_2O_3$, V, and Ni, than the breunneritite (Bogoch et al. 1986; Azer et al. 2010). This is confirmed by semi-quantitative ESEM analyses of the dolomitic and breunneritic components of the carbonatites collected in this study (Table 2). The lamprophyre samples contain 47.2 to 54 wt.% $SiO_2$, 13.4 to 16.5 wt.% $Al_2O_3$, 7.8 to 13.6 wt.% $Fe_2O_3$, 7.7 to 8.5 wt.% CaO, 5.7 to 8 wt.% MgO, 1.2 to 2.1 wt.% $TiO_2$, and 0.8 to 1.1 wt.% $K_2O$ (Table 1).

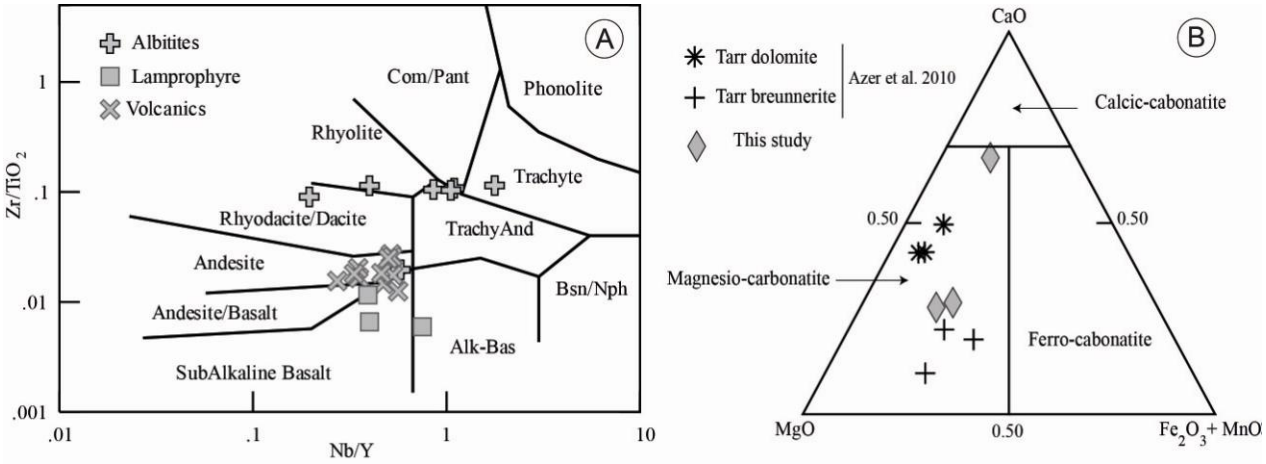


**Fig. 6 a)** Classification of the Wadi Tarr albitites, volcanic country rocks and lamprophyres using the Nb/Y vs. $Zr/TiO_2$ tectonic discrimination diagram (Winchester and Floyd, 1977) **(b)** Classification of the Wadi Tarr carbonatites using the MgO-CaO-$Fe_2O_3$+MnO diagram of Woolley and Kempe (1989). Dolomitite and breunneritite values from Azer et al. (2010) are plotted for comparison.

The Nb/Y vs. $Zr/TiO_2$ lithological discrimination diagram (Winchester and Floyd, 1977) indicates that the albitite has a trachytic to rhyolitic composition and the volcanic country rock a predominantly andesitic composition (Fig. 6a). On the same diagram, the lamprophyres plot within the fields of alkaline and subalkaline basalt (Fig. 6a). The carbonatites plot in the field of magnesio-carbonatite on the MgO-CaO-$Fe_2O_3$+MnO diagram of Woolley and Kempe (1989; Fig. 6b).

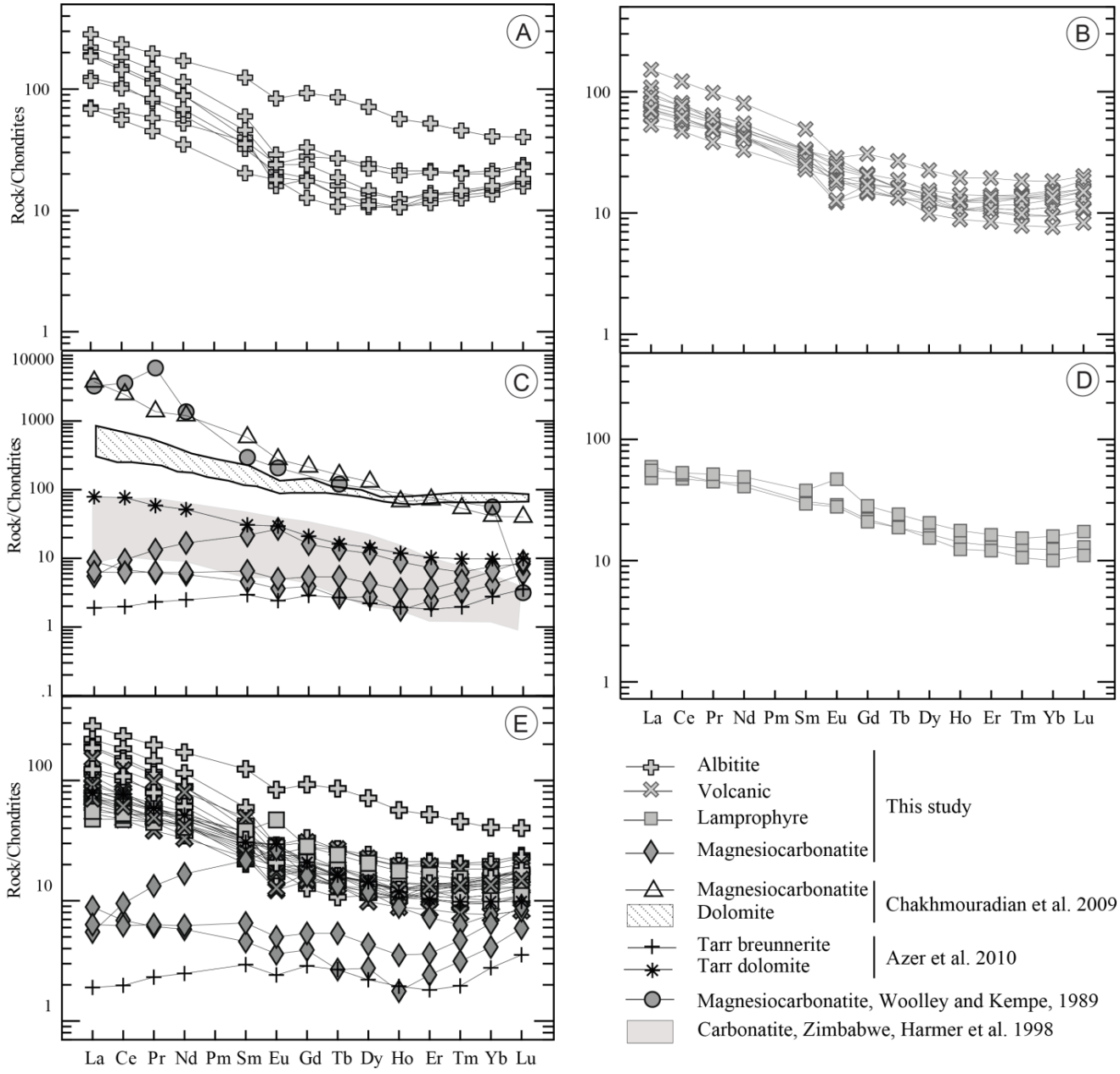


**Fig. 7** Chondrite-normalized REE for the Tarr samples (normalising values after Sun and McDonough, 1989): **(a)** albitites; **(b)** volcanic country rocks; **(c)** carbonatites including dolomitite and breunneritite values from Azer et al. 2010 and magnesiocarbonatite and dolomite values from Wooley and Kempe (1989) and Chakhmouradian et al. (2009), **(d)** lamprophyres **(e)** a comparative plot of albitites, volcanic country rocks, carbonatites and lamprophyres.

The REE concentrations for the albitite, volcanic country rock, lamprophyre and carbonatite are plotted normalised to chondrite in Figure 7. The normalised REE trends for the albitite and volcanic country rocks are similar displaying moderate LREE-enrichment (albitite and volcanic $(La/Lu)_n$ = 2.9-10.4 and 3.96-4.96 respectively), weak to no Eu anomalies (albitite and volcanic Eu/Eu* = 0.55-0.74 and 0.72-1.02 respectively) and almost flat HREE patterns (Albitite and volcanic $(Gd/Lu)_n$ = 1.02-1.45 and 1.08-1.33 respectively)(Fig. 7a, b). One albitite sample (T8) that shows higher REE concentrations and a flatter REE trend contains abundant dolomite and REE-bearing minerals including Gd and Dy bearing oxides which explains the higher MREE values (Fig. 7a). Due to the fact our samples are mixtures of dolomite and breunnerite, we have used the REE compositions of dolomitite and breunneritite from Azer et al. (2010) in the chondrite-normalised REE discrimination diagrams for the carbonatites (Fig. 7c). The compositions of magnesiocarbonatites from Woolley and Kempe (1989) and Chakhmouradian et al. (2009), and the carbonatites from Zimbabwe (Harmer et al. 1988) are also plotted for comparative purposes (Fig. 7c).

**Table 2** ESEM semi-quantitative mineral compositions of the Tarr intrusive dolomite and breunnerite (normalised to 100%)

| Sample | Dolomitic-proportion (T25) | | | Breunneritic proportion (T25) | | | Breunnerite outlining (T25) | | |
|---|---|---|---|---|---|---|---|---|---|
| Spot No. | 1 | 2 | 3 | 1 | 2 | 3 | 1 | 2 | 3 |
| CaO | 52.97 | 55.20 | 55.64 | 0.00 | 0.00 | 0.00 | 31.09 | 27.18 | 34.29 |
| MgO | 37.84 | 38.80 | 38.53 | 73.63 | 74.66 | 74.87 | 25.17 | 29.99 | 26.27 |
| Fe2O3 | 6.32 | 6.00 | 5.83 | 26.37 | 25.34 | 25.13 | 36.48 | 39.89 | 37.01 |
| SiO2 | 2.87 | 0.00 | 0.00 | 0.00 | 0.00 | 0.00 | 6.54 | 2.27 | 2.43 |
| MnO | 0.00 | 0.00 | 0.00 | 0.00 | 0.00 | 0.00 | 0.72 | 0.67 | 0.00 |
| Total | 100.00 | 100.00 | 100.00 | 100.00 | 100.00 | 100.00 | 100.00 | 100.00 | 100.00 |

The samples collected in this study plot between the dolomitite and breunneritite trends from Azer et al. (2010; Fig. 7c). The breunneritite shows distinctive LREE depletion (Fig. 7c), which is characteristic of hydrothermally modified carbonates (Bau and Moller, 1992). The dolomitite which is considered the primary carbonate mineral (see discussion below) shows similar REE patterns to other magnesiocarbonatites albeit with lower REE concentrations (Fig. 7c). Chondrite-normalised REE patterns for the lamprophyres show a slight LREE enrichment [$(La/Lu)_n$=3.1-5.23] and relatively flat HREE profile [$(Gd/Lu)_n$=1.64-1.9] (Fig. 7d). In summary, the albitite, volcanic, the dolomite compositions from the carbonatite and the lamprophyres all have relatively similar REE patterns (Fig. 7e).

### 5.3. Thermometry

Zr-in-rutile thermometry has been used to estimate the crystallisation temperature of hydrothermal rutile in the breccia zone. The Zr-in-rutile thermometry is based on Zr concentrations in rutile, coexisting with quartz and zircon (Zack et al. 2004; Watson et al. 2006; Ferry and Watson 2007; Tomkins et al. 2007). A total of twenty-six spots from 18 rutile grains in two representative samples of albitite-breccia and volcanic-breccia were analysed. The rutile grains in both breccia samples occur in the breccia matrix entirely surrounded by secondary carbonate and these grains are interpreted to have precipitated from the same liquid that precipitated the carbonate. The rutiles in the volcanic-breccia zone (T11) occur mostly as large single grains (50-350 µm) with co-existing fluorapatite, quartz, zircon and monazite (Fig. 8a). The rutile grains in the albitite-breccia are smaller (20-100 µm) than those in the volcanic-breccia but also occur with a similar co-existing assemblage of fluorapatite, zircon, titanite, allanite (Fig. 8b).

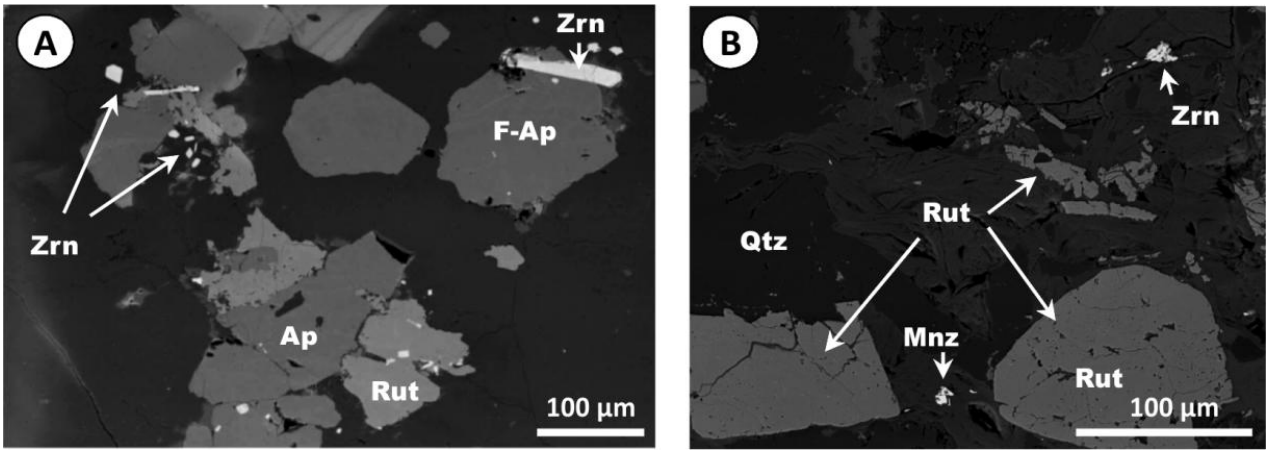


**Fig. 8** Backscatter electron images showing the textural setting of rutile grains investigated with Zr-in-rutile thermometry: **(a)** albitite-breccia, rutile grains with zircon inclusions occur in the matrix coexisting with zircon and fluorapatite (T8); **(b)** volcanic-breccia, rutile grains in the matrix coexisting with quartz, monazite and zircon (T11), F-Ap = fluorapatite, Ap = apatite; Zrn = zircon, Rut = rutile, Qtz = quartz, Mnz = monazite (symbols after Kretz, 1983).

During analysis, rutile grains with zircon submicroscopic inclusions or exsolutions have been avoided. Zoning was observed in two rutile grains of albitite breccia on the basis of decreasing temperatures between the core and rims. Three calibrations of the Zr-in rutile thermometer are used for comparison:

**Table 3** Zr-in-rutile thermometry analysis (EMPA) in Wadi Tarr area

| Sample | Zr (ppm) | T ($^0$C) Zack et al.(2004) | T ($^0$C) Watson et al.(2006) | T ($^0$C) Ferry & Watson (2007) |
|---|---|---|---|---|
| T8-1 | 52 | 519 | 495 | 521 |
| T8-2-1 | 52 | 519 | 495 | 521 |
| T8-2-2 | 30 | 486 | 423 | 489 |
| T8-2-3 | 252 | 628 | 697 | 630 |
| T8-2-4 | 192 | 608 | 662 | 609 |
| T8-2-5 | 96 | 558 | 574 | 560 |
| T8-3 -1 | 96 | 558 | 574 | 560 |
| T8-3-2 | 59 | 527 | 512 | 529 |
| T8-3-3 | 96 | 558 | 574 | 560 |
| T8-3-4 | 74 | 541 | 540 | 543 |
| T8-3-5 | 37 | 499 | 452 | 501 |
| T8-4 | 126 | 577 | 608 | 578 |
| T8-6 | 215 | 616 | 676 | 617 |
| T8-7 | 111 | 568 | 592 | 570 |
| T8-8 | 96 | 558 | 574 | 560 |
| T8-10 | 237 | 624 | 689 | 625 |
| T8-11 | 96 | 558 | 574 | 560 |
| T8-14 | 118 | 573 | 600 | 574 |
| T8-50 | 207 | 613 | 672 | 615 |
| T8-51 | 141 | 585 | 622 | 586 |
| T11-1 | 155 | 592 | 635 | 593 |
| T11-2 | 89 | 553 | 563 | 555 |
| T11-3 | 96 | 558 | 574 | 560 |
| T11-4 | 118 | 573 | 600 | 574 |
| T11-5 | 178 | 602 | 652 | 603 |
| T11-6 | 126 | 577 | 608 | 578 |

Zack et al. (2004): $T_C = 127.8 \ln(Zr_{ppm}) - 10$

Watson et al. (2006): $T_C = \frac{4470}{7.36 - \log(Zr_{ppm})} - 273$

Ferry & Watson (2007): $T_C = \frac{4530}{7.42 - \log(Zr_{ppm})} - 273$

Zr concentrations in rutile and temperature calculated by three different calibrations of the Zr-in-rutile thermometer are listed in Table 3. Based on the Ferry and Watson (2007) calibration, the albitite breccia (T8) gives various temperatures that range between 521 and 630°C with an average of 565±38°C. The volcanic breccia (T11) yields temperatures between 555 and 603°C and an average of 582±18°C.

### 5.4. Fluid inclusion microthermometry:

Fluid inclusions in dolomite and breunnerite from the Wadi Tarr carbonatite were studied in two doubly polished 150 µm thick wafers and the results are listed in Table 4. The majority of fluid inclusions are rhombohedral in shape with minor rectangular, rounded, irregular to negative shapes, and ranging in size from 6 to 23 µm in dolomite and 5 to 25 µm in breunnerite. Three inclusion types have been defined based on their different phases (liquid-vapor-solid) at room temperature and phase transitions observed during heating and cooling measurements (Fig. 9). Type-1 inclusions are $CO_2$-rich (>60 volume percent) with a thin rim of an aqueous liquid phase. Type 2 inclusions contain an aqueous liquid, a halite cube (ca. 10 volume percent) and a $CO_2$-rich vapor phase (10 volume percent). The third type of inclusions consists of an aqueous liquid and a vapor bubble (5 volume percent). Type-1 and 2 inclusions coexist in the same crystals while type-3 inclusions occur in partially recrystallised breunnerite grains. The majority of the fluid inclusions appear to be primary, occurring distributed parallel to the rhombic cleavage and twinning in the carbonates. The following abbreviations are used in text for liquid phases; aqueous liquid ($L_{H2O}$) and liquid carbon dioxide ($L_{CO2}$), and for the vapor phases; aqueous vapor ($V_{H2O}$) and gaseous carbon dioxide ($V_{CO2}$).

**Table 4** Microthermometric data of fluid inclusions from the Wadi Tarr carbonates

| Host mineral (sample) | Type of fluid inclusions | $TmCO_2$ (°C) | Tm,cla (°C) | Tm ice (°C) | $ThCO_2$ (°C) | Tm halite (°C) | Salinity (mass% NaCl) | Th total (°C) | T decr (°C) |
|---|---|---|---|---|---|---|---|---|---|
| **Dolomite (T25)** | Type 1-1 (VCO2) | -56.6 to -58.3 | | | 29.2 to 30.6 (*l*) | | | | |
| | Type 1-2 (LCO2+VCO2) | -56.6 | | | 30.1(*l*) | | | | >300 |
| | Type 1-3 (LCO2+VCO2+LH2O) | -56 to -58.9 | -9.8 to -12.8 | | 29.4 to 30.7 | | 24-25.4* | 378 to 418 | 343-392 |
| | Type 2, ($VCO_2$, LH2O, halite) | -56.6 to -58.8 | | | 31.0 (*l*) | 256-299 | 35.0 to 38.1 | 266 to >440 | 285-379 |
| **Breunnerite (T25)** | Type 1-1 (VCO2) | -56.6 to -58.1 | | | 27.6 to 30.6 (*l*)<br>29.7 to 30.5 (*g*) | | | | |
| | Type 1-2 (LCO2+VCO2) | -57.2 to -58.0 | | | 29.5 (*l*) | | | | >300 |
| | Type 2, ($VCO_2$, LH2O, halite) | -57.2 to -58.1 | | | 30.0 (*l*) | 166-317 | 30.3 to 39.6 | 364-408 | 289-422 |
| **Altered carbonate (T26)** | Type 3, aqueous (V+L) | | | -2.1 to -3.1 | | | 3.6 to 5.1 | 177-182 (*l*) | |

* mass % (CaCl2+NaCl) eq, $T_{m,CO2}$ = melting of the $CO_2$; Tm,cla=melting of carbonic hydrate, $T_{h,CO2}$ = homogenization of the CO2 phases to liquid (*l*) or gas (*g*); $T_{m,ice}$ = final melting of ice; $T_{m.halite}$= melting of the halite cube. Salinity = wt.% NaCl calculated from $T_{m.ice}$; $T_{h.total}$ = total homogenization to the liquid phase.

Type-1 inclusions dominate in the dolomite and breunnerite and can be subdivided into three types. Subtype 1-1 is mostly monophase ($V_{CO2}$) $CO_2$-rich inclusions, subtype 1-2 contains two phases ($L_{CO2}$+$V_{CO2}$) and subtype 1-3 consists of three phases ($L_{CO2}$+$V_{CO2}$+$L_{H2O}$) at room temperature. These three subtypes account for 80% of the total number of fluid inclusions present in the studied carbonates (Fig. 9a). The subtype 1-3

inclusions occur mainly in dolomite rather than breunnerite. Type-1 inclusions do not cross-cut crystal boundaries and occur parallel to the main crystal habits of the carbonate and suggesting that they are primary in origin. After cooling the inclusions to total solidification, the melting temperature of the solid $CO_2$ (Tm $CO_2$) is measured between -56.6° and -58.9°C with homogenization temperature of $CO_2$ ($T_h$ $CO_2$) from +28.0° to +31.0°C to $CO_2$ liquid and between +29.7°C and +30.6° to $CO_2$ gas. The difference in melting temperature from the $CO_2$ triple point (-56.6°C) in some inclusions may indicate the presence of other compounds (e.g., $CH_4$, $N_2$). Based on the data in Van den Kerkhof and Thiéry (2001), the corresponding molar volumes of the $CO_2$ range from about 70 to 100 $cm^3$/mole. Clathrate (gas-hydrate) melting of subtype 1-3 took place in the presence of $L_{H2O}$, $L_{CO2}$ and $V_{CO2}$ in the range from -9.8° to -12.8°C. The melting temperature is lower than the eutectic melting for the pure $CO_2$-$H_2O$-NaCl (-10°C, 24.2 wt. % NaCl), but it is inferred that such low clathrate melting temperatures is possible when $CaCl_2$ is involved in addition to NaCl (Bakker et al., 1996). Using the data in Bakker et al. (1996) the clathrate melting temperatures correspond to between 24 and 25 mass% ($CaCl_2$+NaCl) eq. Total homogenization of type 1-3 inclusions occurred to $L_{H2O}$ at temperatures between 314° and 418°C, although some inclusions decrepitated prior to homogenization. There was no significant difference noted in temperatures when the results are compared for inclusions in dolomite or breunnerite (Table 4).

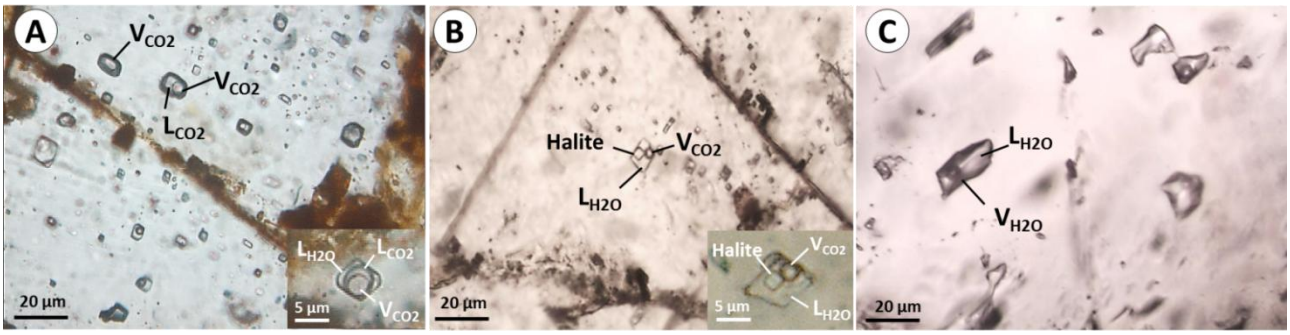


**Fig. 9** Photomicrographs of typical fluid inclusions in samples from the Tarr carbonatites: **(a)** Type 1, carbonic inclusions, subtype1: $CO_2$-rich, subtype 2: ($LCO_2$ +$VCO_2$) and subtype 3: ($LCO_2$+$VCO_2$+$LH_2O$); **(b)** Type 2, halite-bearing; **(c)** Type 3, aqueous inclusions ($LH_2O$+$VH_2O$).

Type-2 inclusions are halite-bearing aqueous inclusions some of which contain a $CO_2$-phase. This type of inclusions accounts for 20% of the total number of fluid inclusion in the carbonates. Halite is the dominant daughter mineral (Fig. 9b); although other unidentified small solid phases with irregular, pseudocubic, or round shapes have also been recognized. The liquid occupies the main inclusion volume 60-80 volume percent in this type while the proportion of the $CO_2$-rich vapor phase is 10-30 vol% and halite proportion is 5-10 vol%. Melting of the $CO_2$ phase occurs at temperatures of -56.6° to -58.8°C and homogenization of the $CO_2$ takes place between +30.0° and +31.0°C (to $L_{CO2}$). Dissolution of halite is measured in the range 166° to 300°C which gives salinities that vary from 30.3 to 38.2 mass% NaCl (Bodnar, 2003). The total homogenization temperatures (to liquid phase) range from 266° to >440°C, however in some inclusions decrepitation occurred before total homogenization was achieved. The halite-bearing inclusions without a $CO_2$ phases showed similar halite melting and homogenization temperatures with halite dissolution at 297° to 317°C, corresponding to salinities of 38.0 to 39.6 mass% NaCl eq. and total homogenization (to liquid) at 367° to 376°C. First melting was noted around -50°C indicating a $H_2O$-NaCl-$CaCl_2$ system for the trapped aqueous fluid (Shepherd et al. 1985)

Type-3 is aqueous two-phase inclusions ($L_{H2O}$+ $V_{H2O}$), consisting of around 5 vol.% vapor bubble in an aqueous liquid (Fig. 9c). These inclusions occur only in breunnerite that shows a recrystallised texture. The melting point of ice ($T_m$ ice) ranges from -2.1° to -3.1°C, corresponding to a salinity of 3.6 to 5.1 wt.% NaCl eq. (Bodnar, 2003). The homogenization temperature varies between 177° to 182 °C, to the liquid state.

## 6. Discussion

### 6.1. The TCA as a carbonatite-albitite-lamprophyre igneous complex

The carbonatites in the TCA occur as clearly intrusive dyke-like bodies in or near to the brecciated margins of the albitite, or as breccia matrix. Carbonate minerals dolomite and breunnerite make up over 90% of the carbonate rocks and this combined with the intrusive nature imply the rocks should be classified as carbonatites using the IUGS classification scheme (Le Maitre, 2002). This classification is supported by stable and radiogenic isotope analyses of the carbonatites. Dolomite from the carbonatite bodies has stable and radiogenic isotope compositions that indicate they were derived from a mantle source (mean $\delta^{18}O$ = +6.9‰; mean $\delta^{13}C$ = -8.1‰; mean δD = -65‰, mean εNd = +3.4 to +5.5; mean $^{87}Sr/^{86}Sr$ = 0.70356 to 0.70422; Bogoch et al. 1986, Azer et al. 2010). The isotopic composition of the breunnerite also shows a dominantly mantle source but with partial re-equilibration with surface derived fluids such as seawater (mean $\delta^{18}O$ = +18.8‰; mean $\delta^{13}C$ = -6.1‰; mean εNd = +2.2; mean $^{87}Sr/^{86}Sr$ = 0.70805; Azer et al. 2010). Besides the clear spatial association, an isotopic and geochemical association can also be observed between TCA albitite and carbonatites (Shimron, 1975; Bogoch et al. 1986; Blasy et al. 2001; Azer et al. 2010). The albitite has similar isotopic compositions that indicate a mantle source similar to the carbonatite and supporting the interpretation that these rocks are genetically linked (Azer et al. 2010). The lamprophyres occur dominantly within or near the brecciation zone but are undeformed implying that they intruded late in the evolution of the TCA. The stable isotope composition of dolomite and calcite ocelli in these rocks shows mantle values very similar to those of the carbonatites ($\delta^{18}O$ ranges 4 to 9.5‰, $\delta^{13}C$ ranges -4.5 to -6.5‰; Bogoch and Magaritz 1983). Normalised REE patterns for the albitite, the dolomite from the carbonatite and the lamprophyre are very similar indicating the possibility of a common source for these rocks (Fig. 7). We suggest that based on 1) the field relationships, 2) the isotopic compositions, and 3) the chemical compositions specifically of the REE, that the Wadi Tarr igneous complex should be classified as a carbonatite-albitite-lamprophyre igneous complex, and that these rocks come from a common mantle derived source.

### 6.2. Comparison with other carbonatite alkaline igneous complexes.

One of the most conspicuous features of the Tarr carbonatite is that it is depleted in trace elements (specifically Sr, Ba and REE) relative to average carbonatite (Table 1; Fig. 7c). REE-poor carbonatites have been previously reported from the Fen complex, Norway (Andersen, 1986), the Buhera district, Zimbabwe (Harmer et al. 1998), the Grønnedal-Ika complex, Greenland (Halama et al. 2005), and Beara Peninsula, Ireland (Brady and Moore, 2012). The low REE content in some of these examples has been attributed to post-magmatic loss due to hydrothermal recrystallisation of the carbonate (e.g. Andersen, 1986; Halama et al. 2005). However in others it is considered to be a primary feature of the magmatic source (e.g. Brady and Moore, 2012). Remobilised carbonate commonly shows LREE depletion (Bau and Moller, 1992) such as is observed in the breunnerite samples from the TCA (Table 1, Fig. 7c). The dolomite at Tarr shows a similar REE trend to classic carbonatites just with lower concentrations (Fig. 7c), and we suggest that this is a primary feature. Low REE content in carbonatites has been suggested to be a regional feature that is characteristic of the lithospheric mantle in that region (Brady and Moore, 2012). REE-poor carbonatites have been reported for a number of localities in the ANS (e.g. El-Haddad et al. 1984) and it is possible that this is a function of a regional scale REE-poor source area for the ANS.

In their review of carbonatite paragenetic types, Woolley and Kjarsgaard (2008) suggest that carbonatites associated with alkali silicate igneous rocks are most likely to have formed from differentiation from primary silicate magma generated in the upper lithosphere (Woolley and Kjarsgaard, 2008). Differentiation is suggested to have occurred though crystallisation fractionation (Watkinson and Wylie, 1969, 1971), or immiscibility (Harmer and Gittins, 1998; Stoppa et al. 2005). Other studies show carbonatites occurring together with silicate magmas may have had a separate source and that the spatial relationship observed is due to, for example crustal silicate magma entrainment in an ascending carbonatite body (e.g. Moore et al. 2009) or injection of carbonatite magma into a crustal magma chamber (e.g. Chazot et al. 2003, Valentini et al. 2010). In both of these cases the separate sources are observable by stable and radiogenic isotope compositions that show mixing between mantle and crustal end-members. Experimental studies have shown that immiscibility of carbonate and associated silicate rocks from a common parent may produce carbonatites with much higher sodium and/or potassium contents than are observed (Freestone and Hamilton, 1980; Lee and Wylie, 1996). One possible explanation is that carbonatite magmas were indeed alkali-rich but they lost the alkali content during cooling in the presence of a hydrothermal system. Fennitisation surrounding many intrusive carbonates is commonly cited as evidence for this alkali loss (e.g. Le Bas, 2008).

The similarity in isotopic and trace element compositions from the alkaline igneous rocks and carbonatites in the TCA imply that they have a common, mantle-derived source. Azer et al. (2010) suggest that the Tarr magmas were produced in the upper mantle in an intra-plate setting due to rifting, and separated through liquid immiscibility in a magmatic cupola at hypabyssal depths. The carbonatites have an extremely low alkali content (Table 1) but the existence of alkali-rich liquid is shown by the high salinity primary fluid inclusions that are preserved in the dolomite and breunnerite (Table 4, Fig. 9).

### 6.3. Fennitisation surrounding the TCA

Reports of the extent of fennitic alteration surrounding the TCA vary greatly from a zone of amphibolitisation and carbonation with associated enrichments of Fe, Mg, Na, Ti and P extending a few hundred meters outside the breccia zone (Shimron, 1975) to extensive alkali metasomatism of the albitite bodies at Tarr whereby the albitite itself is the product of the fennitisation of what was previously a plagiogranite (Bogoch et al. 1987). Neither study reports exact locations of where the fennitisation occurs relative to the TCA and so these localities could not be investigated in this study. In order to evaluate the extent and effects of any fennitic alteration surrounding the TCA we have carried out a mineralogical and geochemical investigation of the albitite, the carbonatite, the volcanic country rock and the breccia zone proximal to the intrusion. In the areas investigated in this study, secondary silicate minerals are dominantly constrained to the breccia zone surrounding the albitite. Actinolite, carbonate, chlorite, sericite and epidote occur in the both the albitite and volcanic country rock-hosted breccia (Fig. 5a to d). Reaction textures include primary biotite being completely altered to sericite, and albite being replaced by sericite and carbonate (Fig. 5a to d). Carbonates, which occur as fracture-filling cement or replacing primary feldspars, is more abundant in the volcanic-breccia compared to the albitite-breccia and they contain accessory rutile, apatite, iron-oxides, allanite zircon and xenotime (Fig. 5e, f). The metasedimentary country rock shows no indication of fennitisation. The rocks have clearly been metamorphosed containing cordierite and biotite but they contain no carbonate or actinolite that are conspicuous in the albitite and volcanic breccia samples. The lamprophyre samples that also occur in the breccia zone are strongly altered with sericitised and epidotized feldspar, clinopyroxenes altered to chlorite ± carbonate ± Fe-oxides, and primary hornblende altered along grain margins to actinolite ± tremolite (Fig. 4f). The carbonate in these samples is mostly dolomite with minor calcite.

None of the minerals commonly associated with fennitisation such as Na-rich amphiboles or pyroxenes, or alkali feldspar (Druppel et al, 2005; Le Bas, 2008) occur in the altered breccia zone samples or distal to the intrusion. Albite is clearly abundant in the albitite but its textural affinity (e.g. simple albite and carlsbad twins rather than characteristic checkerboard albite that is associated with fennitisation) is consistent with its occurrence as a primary igneous phase. Some samples contain veins of carbonate and albite (Fig. 5c) or recrystallisation of feldspar to sericite (Fig. 5d), which may indicate alkali remobilisation, but the extent of this is localized.

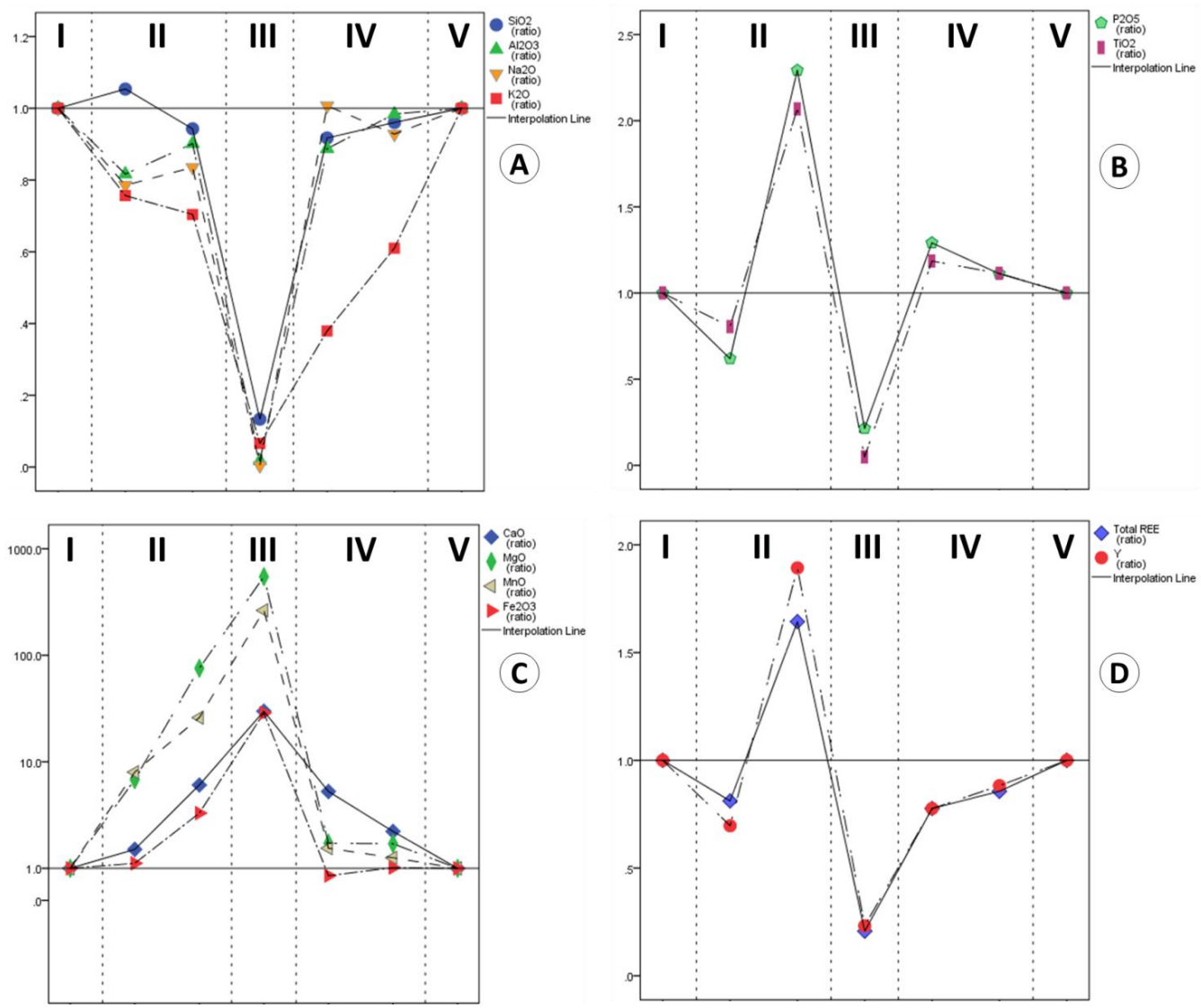


**Fig. 10** Plots of normalised elemental concentrations of albitite and volcanic breccia and carbonatite samples; I: fresh albitite, II: albitite-breccia, III: intrusive carbonate, IV: volcanic-breccia, V: least altered volcanics**. (a)** $SiO_2$, $Al_2O_3$, $Na_2O$ and $K_2O$**; (b)** CaO, MgO, $Fe_2O_3$ and MnO and $Fe_2O_3$, **(c)** $P_2O_5$ and $TiO_2$ and **(d)** REE. The albitite-breccia samples were normalised to fresh albitite (the mean of samples T7, T19 and T20), and the volcanic-breccia samples to least altered volcanic country rock (the mean of T28, T34, and T41). Carbonatites were normalized to fresh albitite so that they fit on the same diagram. The diagrams show that the alteration in the breccia zones is dominantly controlled by precipitation of carbonate.

The geochemical compositions also suggest that large-scale alkali metasomatism has not occurred. Normalised albitite breccia and volcanic breccia compositions are shown in figure 10. The albitite breccia samples have been normalised to the composition of fresh albitite (the mean of samples T7, T19 and T20), and the volcanic breccia samples have been normalised to the composition of least altered volcanic country rock (the mean of T28, T34, and T41). Carbonatites have also been included with their compositions normalised to fresh albitite so that they fit on the same diagram. Neither the metasedimentary rocks nor the lamprophyres have been included, as we do not know the composition of the unaltered protolith rock that would allow normalisation.

The diagrams show that the alteration in the breccia zones is dominantly controlled by precipitation of carbonate (Fig. 10). $SiO_2$, $Al_2O_3$, $Na_2O$ and $K_2O$ show lower concentrations in the albitite and volcanic breccia and in the carbonatites compared to their unaltered end member compositions (Fig. 10a), whereas CaO, MgO, $Fe_2O_3$ and MnO concentrations are higher in the albitite and volcanic breccia and in the carbonatites compared to the fresh albitite and volcanic country rock (Fig. 10b). The breccia samples plot on mixing lines between the fresh albitite and volcanic compositions and that of the carbonatites (Figs. 10a and 10b). In the albitite breccia the dilution and enrichment trends shown in figures 10a and 10b can be attributed dominantly to the occurrence of carbonates, but also to the precipitation of actinolite, epidote and chlorite (Fig. 5a, b). In the volcanic breccia the depletion and enrichment trends are attributed to hydrothermal alteration of K-feldspar and plagioclase to sericite + carbonate ± epidote leading to dilution of silica, $Al_2O_3$ and $K_2O$ (Fig. 5c, d). Enrichment of CaO, MgO occurring in some volcanic breccia samples, is attributed to diffusive veinlets of carbonates and albite (Fig. 5c). The degree of carbonate alteration is variable in volcanic breccia with some samples preserving the original volcanic textures and others partially to completely recrystallised.

In summary, alteration surrounding the TCA observed in this study is limited in scale occurring only in the zone of brecciation immediately surrounding the intrusion, and limited in degree being mainly controlled by carbonate precipitation. Previous investigations provide good evidence for fennitisation such as preservation of sedimentary textures in albitised conglomerates and the occurrence of checkerboard albite (Shimron, 1975; Bogoch et al. 1987), but the exact locations of where this fennitisation was observed is not reported. The style of alteration observed in this study is similar to that reported by Shimron (1975), although less extensive in the areas we investigated. We suggest that fennitisation has occurred but extent of this alteration is spatially variable and most likely lithologically controlled. The alteration is dominated by precipitation of carbonates of the same variety as observed in the intrusive carbonate dykes and we suggest that they come from the same magmatic source.

### 6.4. Conditions of carbonatite precipitation

The temperature and pressure at which the carbonatite in the TCA crystallised have been constrained using Zr-in-rutile thermometry of hydrothermal rutile in the breccia zone, and fluid inclusion microthermometry from the carbonatites themselves. The rutile crystals investigated occur within clusters of apatite + fluorapatite + allanite ± xenotime ± monazite ± zircon ± rutile hosted by carbonate (Fig. 8a, b). These minerals are hosted entirely by the carbonate in the breccia matrix and are interpreted to have crystallised from the carbonatitic liquid that invaded the breccia zone. The rutile crystallisation temperature of 565±38°C is higher than the temperature indicated by fluid inclusion thermometry in the carbonatites and the rutile therefore most likely crystallised prior to the carbonate. Fluid inclusion analysis shows that that carbonatite magma contained a high-salinity $H_2O$-$CO_2$-NaCl-$CaCl_2$ fluid. The occurrence of saline fluid inclusions suggests that the carbonatite magma had a significant initial alkali content.

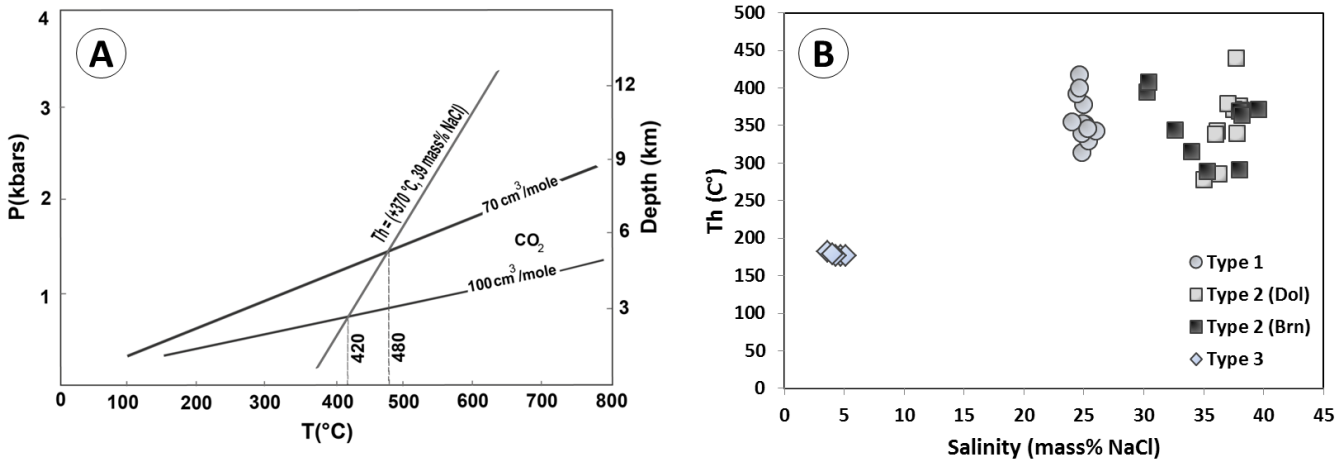


**Fig. 11 (a)** P-T diagram based on isochores intersection of low-density (type 1) and high-density (type 2) inclusions showing formation temperature between to 420° to 480°C and corresponding depth of 2.8-4.9 km, Depths calculated on basis of rock density of 2.6 g/cm$^3$; **(b)** Plot of homogenization temperature vs. salinity of type 1 (carbonic), type 2 (halite bearing) and type 3 (aqueous).

Fluid inclusion compositions show that this fluid unmixed into a low-density phase composed of $CO_2$ fluid (type 1 inclusions) and a high-density phase composed of a high-salinity (24-25 mass% NaCl+$CaCl_2$) aqueous fluid (type 2 inclusions). The compositions of these inclusions can be used to estimate the trapping conditions using the technique of intersecting isochores (Roedder, 1984). Microthermometric data for the $CO_2$ inclusions reveal molar volumes between about 70 to 100 cm$^3$/mole. Isochores for these molar volumes are constructed in figure 12a after Van den Kerkhof and Thiéry (2001). For the isochore representing the results from the halite-bearing aqueous inclusions data in Bodnar (2003) are used (Fig. 11a) for salinities around 39 wt.% NaCl eq. and total homogenization (to liquid) around 370°C. Intersections of the isochores for the lower and upper ends of the primary inclusions of this type with the lithostatic pressure of 0.75 to 1.3 kbar yield a formation temperature range from 420°-480°C and corresponding depth of 2.8-4.9 km (Fig. 11a). We suggest that the carbonatites crystallised at these conditions. Primary fluid inclusions reveal similar fluid characteristics for both dolomite and breunnerite implying that both carbonate phases preserve the original magmatic fluid signature. However breunnerite also contains secondary (type 3) fluid inclusions with a salinity of 3.6 to 5.1 mass% NaCl eq. and a homogenization temperature of around 180°C (Table 4, Fig. 11b). These inclusions suggest interaction with a surficial fluid such as meteoric water or seawater, which most likely led to the partial isotopic re-equilibration of breunnerite (Bogoch et al. 1986; Azer et al. 2010).

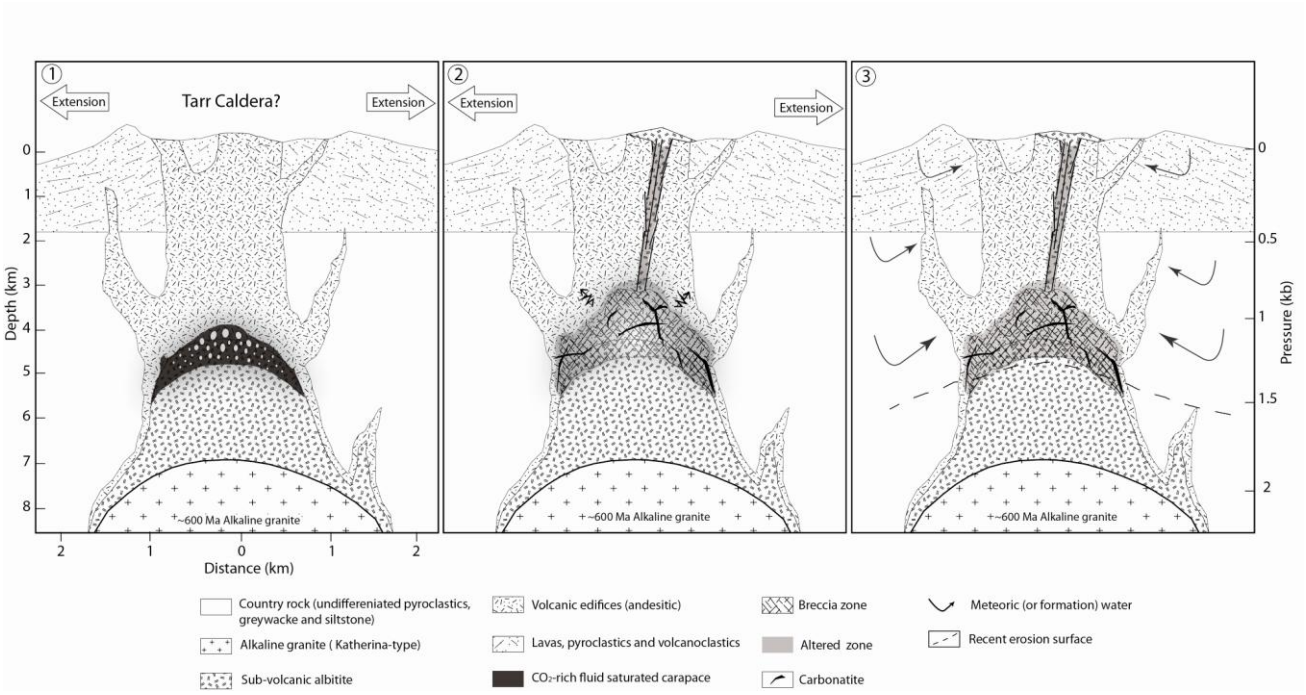


**Fig. 12** Schematic cross-sections of Tarr magmatic-hydrothermal system modified after Azer et al. (2010); **(1)** generation of a vapor saturated magmatic fluid carapace above subvolcanic crystalising albitite body; **(2)** immiscibility between silicate and carbonatite magma and brecciation form carbonatite dykes and breccia matrix. Crystallisation of the carbonatite occurs between 565±38°C and 420°-480°C; **(3)** post-crystallisation interaction with surface fluid such as meteoric, sea or formation water-caused alteration of carbonatite producing low-salinity, low temperature fluid inclusions (~180°C), and stable and radiogenic isotopic resetting.

Our data support the model proposed by Azer et al (2010) of immiscibility of a carbonatite and albitite melts in a shallow-level cupola culminating in explosive emplacement of the albitite breccia and carbonatite. We suggest that early crystallisation in the breccia zone occurred at 565±38°C as shown by Zr-in rutile thermometry, and that the carbonatites crystallised at 0.75 to 1.3 kbar and 420°-480°C and corresponding depth of 2.8-4.9 km (Fig. 12). The carbonatite magma contained a high-salinity $H_2O$-$CO_2$-NaCl-$CaCl_2$ fluid that most likely cause fennitisation in surrounding rocks (Fig. 12). The extent and degree of fennitisation in highly variable most likely due to heterogeneous fluid flow but is in general, lower than reported in many other carbonatite complexes. We suggest that the low trace element content of the carbonatite is a function of the composition of the source area for the mantle-derived melts. The spatial association and trace element and isotopic compositions of the lamprophyre strongly imply that these rocks were generated from the same mantle source at depth. Evidence for carbonatite immiscibility in these rocks in the form of dolomite ocelli (Bogoch and Margitz, 1983) indicates these rocks evolved similarly to the albitite as they ascended from the mantle source at depth.

## 7. Conclusions

We suggest based on field and petrographic observations, and geochemical and isotopic compositions, that the TCA should be classified as a carbonatite-albitite-lamprophyre igneous complex. The trace element concentrations of the carbonatite are low compared to "classic" carbonatites but trace element-poor carbonatites have been reported elsewhere, although they are uncommon, particularly those with a magnesian, dolomite-rich affinity (e.g. Andersen, 1986; Harmer et al. 1998; Hornig-Kjarsgaard, 1998; Halama et al. 2005; Brady and Moore, 2012). Trace element-poor carbonatites have been reported elsewhere in the ANS (e.g., El-Haddad et al. 1984), and we suggest that this is a function of the composition of the

mantle source region. Fennitic alteration surrounding the TCA carbonatites is variable in extent. In the areas investigated in this study alkali metasomatism is not observed and alteration is dominated by precipitation of carbonatite in the breccia zone surrounding the albitite with spatially associated actinolite, chlorite, sericite and epidote. Previous investigations suggest more pervasive fennitisation that caused albitisation of the intrusive and country rocks (Shimron, 1975; Bogoch et al. 1987). The carbonatite magma contained a high-salinity $H_2O$-$CO_2$-NaCl-$CaCl_2$ fluid that most likely caused the reported fennitisation in some areas. We suggest that fennitisation has occurred but extent of this alteration is spatially variable and most likely lithologically controlled. Crystallisation of the carbonatite in the dykes and the breccia zone occurred between 565±38°C and 420°-480°C, and at 0.75 to 1.3 kbar which corresponds to a depth of 2.8-4.9 km (Fig. 12). Small aggregates of rutile, apatite, allanite, xenotime, monazite, and zircon within the carbonatite breccia most likely crystallised early at 565±38°C. The carbonatite dykes crystallised later after cooling to around 420°-480°C. Our data support the model proposed by Azer et al (2010) of immiscibility of a carbonatite and albitite melts in a shallow-level cupola culminating in explosive emplacement of the albitite breccia and carbonatite.

## References


- Ali, B.H., Wilde, S.A., Gabr, M.M.A., 2009. Granitoid evolution in Sinai, Egypt, based on precise SHRIMP U–Pb zircon geochronology. Gondwana Research, 15, 38-48.
- Andersen, T., 1986. Magmatic fluids in the Fen carbonatite complex, S.E. Norway: Evidence of mid-crustal fractionation from solid and fluid inclusions in apatite. Contributions to Mineralogy and Petrology, 93, 491-503.
- Azer, M.K., Stern, R.J., Kimura, J.I., 2010. Origin of a Late Neoproterozoic (605±13 Ma) intrusive carbonate-albitite complex in Southern Sinai Egypt. International Journal of Earth Sciences, 99, 245-267.
- Bakker, R.J., Dubessy, J., and Cathelineau, M., 1996. Improvements in modelling: I. The $H_2O$-$CO_2$ system with various salts: Geochimica et Cosmochimica Acta, 60, 1657-1681.
- Bau, M. and Möller, P., 1992. Rare-earth element fractionation in metamorphogenic hydrothermal calcite, magnesite and siderite. Mineralogy Petrology, 45, 231-246.
- Be'eri-Shlevin, Y., Katzir, Y., Valley, J.W., 2009. Crustal evolution and recycling in a juvenile continent: oxygen isotope ratio of zircon in the northern Arabian Nubian Shield. Lithos, 107, 169-184.
- Bentor, Y.K., Eyal, M., 1987. The Geology of Southern Sinai, Its Implication for the Evolution of the Arabo-Nubian Massif. Israeli Academy of Sciences and Humanities, Jerusalem. 484 pp.
- Blasband, B., Brooijmans, P., Dirks, P., Visser, W., White, S., 1997. A Pan-African core complex in the Sinai, Egypt. Geol. Mijnbouw, 76, 247-266.
- Blasband, B., White, S., Brooijmans, P., De Boorder, H., Visser, W., 2000. Late Proterozoic extensional collapse in the Arabian–Nubian Shield. Journal of the Geological Society of London, 157, 615-628.
- Blasy, M., Baroudy, A.F., Kharbish, S.M., 2001. Geochemical characteristics of Wadi Tarr albitite, Southeastern Sinai, Egypt. Egyptian Journal of Geology, 42, 767-780.
- Bodnar, R.J., 2003. Introduction to aqueous-electrolyte fluid inclusions. In Samson, I., Anderson, A. and Marshall, D. (eds.) Fluid Inclusions: Analysis and Interpretation. Mineralogical Association of Canada, Short Course, 32, 81-99.
- Bogoch, R., Bahat, D., Kisch, H., 1987. The Tarr albitite: a metasomatic plagiogranite from mainly non-intrusive protoliths. Ofioliti, 12, 8-22.
- Bogoch, R., Eldad, H., Nathan, Y., 1984. Scandium-bearing carbonates of the Tarr albitite complex, Southeast Sinai. Geochimica et Cosmochimica Acta, 48, 885-887.
- Bogoch, R., Magaritz, M., 1983. Immiscible silicate–carbonate liquids as evidenced from ocellar diabase dykes, Southeast Sinai. Contributions to Mineralogy and Petrology, 83, 227-230.
- Bogoch. R., Magaritz, M., Michard, A., 1986. Dolomite of possible mantle origin, Southeast Sinai. Chemical Geology, 56, 281-288.
- Brady, A.E., Moore, K.R., 2012. A mantle-derived dolomite silicocarbonatite from the southwest of Ireland, Mineralogical Magazine, 76, 357-376.

- Brooijmans, P., Blasband, B., White, S.H., Visser, W.J., Dirks, P., 2003. Geothermobarometric evidence for a metamorphic core complex in Sinai, Egypt. Precam. Res. 123, 249-268.
- Chakhmouradian A.R., Böhm C.O., Demény A., Reguir E.P., Hegner E., Creaser R.A., Halden N.M. & Yang P., 2009. "Kimberlite" from Wekusko Lake, Manitoba: Actually a diamond-indicator-bearing dolomite carbonatite. Lithos, 112S, 347-357.
- Chazot, G., Bertrand, H., Mergoil, J., Sheppard, S.M.F., 2003. Mingling of immiscible dolomitic carbonatite and trachyte in tuffs from the Massif Central, France. Journal of Petrology, 44 (10), 1917-1936.
- Druppel, K., Hoefs, J., Okrusch, M., 2005. Fenitizing processes induced by Ferrocarbonatite Magmatism at Swartooisdrif, NW Namibia. Journal of Petrology, 46, 377-406.
- El-Haddad, M.A., Hashad, M.H., 1984. The major and minor elements chemistry of Gebel Tarbtie carbonatites South, Egypt. Bull Fac Sci Assuit Univ 13, 205-217.
- Eyal, M., Bartov, Y., Shimron, A.E., Bentor, Y.K., 1980. Sinai Geological Map, Geological Survey of Israel.
- Ferry, J.M., Watson, E.B., 2007. New thermodynamic models and revised calibrations for the Ti-in-zircon and Zr-in-rutile thermometers. Contrib Mineral Petrol 154, 429-437.
- Fowler, A., Hassen, I.S., Osman, A.F., 2010. Neoproterozoic structural evolution of SE Sinai, Egypt: II. Convergent tectonic history of the continental arc Kid Groupd. J. Afr. Earth Sci. 58, 526-546.
- Freestone, J.C., Hamilton, D.L., 1980. The role of liquid immiscibility in the genesis of carbonatites – an experimental study. Contributions to Mineralogy and Petrology, 73, 105-117.
- Halama, R., Vennemann, T., Siebel, W., Markl, G., 2005. The Grønnedal-Ika carbonatite–syenite complex, South Greenland: carbonatite formation by liquid immiscibility. Journal of Petrology, 46, 191-217.
- Harmer, R.E., Gittins, J., 1998. The case for primary, mantle-derived carbonatite magma. Journal of Petrology, 39, 1895-1903.
- Harmer, R.E., Lee, C.A., Eglington, B.M., 1998. A deep mantle source for carbonatite magmatism: evidence from the nephelinites and carbonatites of the Buhera district, SE Zimbabwe, Earth Planet. Sci Lett, 158, 131-142.
- Heinrich, E.W., 1985. Infinite variations on a fenite theme. Indian Mineral, Sukheswala, 151-162.
- Hornig-Kjarsgaard, I., 1998. Rare earth elements in sovitic carbonatites and their mineral phases. Journal of Petrology, 39, 2105-2121.
- Ibrahim M.E., Ragab, A.A., 2011. Geochemistry of lamprophyre dykes, Wadi Sikait area, South Eastern Desert, Egypt. Chinese Journal of Geochemistry, 30,323-331.
- Ibrahim M.E., Saleh G.M., Dawood N.A., and Aly G.M., 2010. Ocellar lamprophyre dyke bearing mineralization, Wadi Nugrus, Eastern Desert, Egypt: Geology, mineralogy and geochemical implications. Chinese Journal of Geochemistry, 29, 383-392.
- Khalaf, E.A., 2004. Volcaniclastic aggradation in El Tarr Area, southeastern Sinai, Egypt: petrological and geochemical evidence. JKAU, Earth Sci. 15, 51-96.
- Kinnaird, J.A., Bowden, P., 1991. Magmatism and mineralization associated with Phanerozoic Anorogenic Plutonic complexes of the African plate. In: Kampunzu A, Lubala RT (eds) The phanerozoic African plate. Springer, Berlin, pp 410-485.
- Le Bas, M.J. 1981. Carbonatite magmas. Mineralogical Magazine. 44, 133-140.
- Le Bas, M.J., 2008, Fenites associated with carbonatites: Canadian Mineralogist, 46, 915-932.
- Le Maitre, R.W., Streckeisen, A., Zanettin, B., Le Bas, M.J., Bonin, B., Bateman, P., Bellieni, G., Dudek, A., Efremova, S., Keller, J., Lameyre, J., Sabine, P.A., Schmid, R., Sorensen, H. and Woolley, A.R. 2002. Igneous Rocks: A Classification and Glossary of Terms. Recommendations of the International Union of Geological Sciences, Subcommission on the Systematics of Igneous Rocks. Cambridge University Press, Cambridge, UK. 236 pp.
- Le Maitre. R.W., Bateman, P., Dudek, A., Keller, J., Lameyre, J.. Le Bas, M.J., Sabine, P.A., Schmid, R., Sorensen, H., Streckeisen, A., Woolley, A.R. & Zanettin, B., 1989. A Classification of Igneous Rocks and Glossary of terms: Recommendations of the International Union of Geological Sciences Subcommission on the Systematics of Igneous Rocks. Blackwell Scientific Publications, Oxford, U.K.
- Lee,W.-H., Wyllie, P.J.,1996. Liquid immiscibility in the join $NaAlSi_3O_8$–$CaCO_3$ to 2.5 GPa and the origin of carbonatite magmas. Journal of Petrology, 37, 1125-1152.

- Moghazi, A.M., Ali, K.A., Wilde, S.A., Zhou, Q., Andersen, T., Andresen, A., Mahrous, A. E., Stern, R.J., 2012. Geochemistry, geochronology, and Sr-Nd isotopes of the Late Neoproterozoic Wadi Kid volcano-sedimentary rocks, Southern Sinai, Egypt: Implications for tectonic setting and crustal evolution. Lithos, 154, 147-165.
- Moore, K.R., Wall, F., Divaev, F.K. and Savatenkov, V.M. 2009. Mingling of carbonate and silicate magmas under turbulent flow conditions: Evidence from rock textures and mineral chemistry in subvolcanic carbonatite dykes, Chagatai, Uzbekistan, Lithos, 110, 65-82.
- Reymer, A.P.S., Yogev, A., 1983. Stratigraphy and tectonic history of the southern Wadi Kid metamorphic complex, southeastern Sinai. Israel Journal of Earth Sciences. 32, 105-116.
- Rock, N.M.S., 1991, Lamprophyres, Blackie, Glasgow, UK ISBN 978-0442303969.
- Roedder, E., 1984. Fluid inclusions. Mineralogical Society of America. Rev. in Mineral. 12, 644 pp.
- Samoilov, V.S., 1991. The main geochemical features of carbonatites. Journal of Geochemical Exploration, 40, 251-262.
- Shepherd, T.J., Rankin, A.H. and Alderton, D.H.M., 1985. A practical guide to fluid inclusion studies. Blackie, Glasgow
- Shimron, A.E., 1975. Petrogenesis of the Tarr albitite–carbonatite complex, Sinai Peninsula. Miner Mag, 40, 13-24.
- Shimron, A.E., 1980. Proterozoic island arc volcanism and sedimentation in Sinai. Precambrian Research, 12, 437-458.
- Soliman, K.A., Tolba, M.E., El-Manakhly, M.M., Madbouly, M.E., Hasan, M.M., Abd El Magid, E.A., Khyamy, A.A., Abd El Mola, A.F., Mohamed, H.A., 1992. Geology of the albitite rock, Wadi El-Tarr, Southern Sinai. Ann Geol Surv Egypt, 18, 29-37.
- Stern, R.J., 1981. Petrogenesis and tectonic setting of late Precambrian ensimatic volcanic rocks, central Eastern desert of Egypt. Precambrian Research, 16, 195-230.
- Stern, R.J., Gwinn, C.J., 1990. Origin of late Precambrian intrusive carbonates, Eastern Desert of Egypt and Sudan: C, O and Sr isotopic evidence. Precambrian Research, 46, 259-272.
- Stoppa, F., Rosatelli, G., Wall, F., Jeffries, T., 2005. Geochemistry of carbonatite-silicate pairs in nature: a case history from Central Italy. Lithos, 85, 26-47.
- Sun, S.S., McDonough, W.F., 1989. Chemical and isotopic systematics of oceanic basalts; implications for mantle composition and processes. In: Magmatism in the ocean basins. Saunders, A.D. and Norry, M.J. (Editors), Geological Society of London, London. 42, 313-345.
- Tomkins, H.S., Powell, R., Ellis, D.J., 2007. The pressure dependence of the zirconium-in-rutile thermometer. Journal of Metamorphic Geology, 25, 703-713.
- Valentini, L., Moore, K.R., Chazot, G., 2010. Unravelling carbonatite–silicate magma interaction dynamics: A case study from the Velay province (Massif Central, France), Lithos, 116, 53-64.
- Van den Kerkhof, A., Thiéry, R., 2001. Carbonic inclusions. Lithos, 55, 49-68.
- Watkinson, D.H., Wyllie, P.J., 1969. Phase equilibrium studies bearing on the limestoneassimilation hypothesis. Bulletin of the Geological Society of America, 80, 1565-1576.
- Watkinson, D.H., Wyllie, P.J.,1971. Experimental study on the join $NaAlSiO_4$–$CaCO_3$–$H_2O$ and the genesis of alkalic rock-carbonatite complexes. Journal of Petrology, 12, 357-378.
- Watson, E.B., Wark, D.A., Thomas, J.B., 2006. Crystallization thermometers for zircon and rutile. Contributions to Mineralogy and Petrology, 151, 413-433.
- Winchester, J. A., Floyd, P. A., 1977. Geochemical discrimination of different magma series and their differentiation products using immobile elements. Chemical Geology, 20, 325-343.
- Woolley, A.R., Kempe, D.R.C., 1989. Carbonatites: nomenclature, average chemical compositions, and element distribution. In: Bell, K. (Ed.), Carbonatites: Genesis and Evolution. Unwin Hyman, pp. 1-14.
- Woolley, A.R., Kjarsgaard, B.A., 2008. Carbonatite occurrences of the world: map and database. Geological Survey of Canada.
- Zack, T., Moraes, R., Kronz, A., 2004. Temperature dependence of Zr in rutile: empirical calibration of a rutile thermometer. Contributions to Mineralogy and Petrology, 148, 471-488.

# Paper II

# Regional carbonate alteration in the ophiolitic components of Meatiq area, Central Eastern Desert (CED), Egypt: Isotopic evidence and geochemical aspects

**Iain Pitcairn[1], Ahmad Boskabadi[1], Curt Broman1, Adrian Boyce[2], Damon Teagle[3], Matthew Cooper[3], Mokhles Azer[4], Fathy Mohamed[5], and Robert Stern[6]**

*(1) Department of Geological Sciences, Stockholm University, Stockholm, Sweden,*
*(2) Scottish Universities Environmental Research Centre, East Kilbride, UK,*
*(3) National Oceanography Centre Southampton, University of Southampton, UK,*
*(4) Geology Department, National Research Centre, Cairo, Egypt,*
*(5) Geology Department, Faculty of Science, Alexandria University, Alexandria, Egypt,*
*(6) Geosciences Department, University of Texas at Dallas, Texas, USA*

## Abstract

The Meatiq study area occurs within Najd shear zone and exposes the Meatiq core complex which is thought to represent the structurally lowest units in the Central Eastern Desert (CED), Egypt. The Meatiq core complex is exposed in a tectonic window through the Neoproterozoic cover nappes that comprise variably carbonatised ophiolitic sequences and metasedimentary rocks. This study investigates the mineralogy, geochemistry, isotopic compositions and fluid inclusion compositions of serpentinites, talc-rich rocks, carbonate veins and meta-volcanics with the goal of determining of chemical mobility, deciphering the fluid sources and investigating the condition of alteration in the ophiolitic sequences.

Based on field, microscopic and Raman micro-spectroscopy, two varieties of serpentinites lizardite- and antigorite-bearing have been distinguished in the study area. The serpentinites have been variably carbonate altered and both varieties are characterized by relatively high concentrations of fluid-mobile elements (FME: Li, As, Au, S, Pb, U, Ba, Sr, Sb, Cs). Antigorite (Atg) is stable at higher temperatures than lizardite (Lz; Evans, 2004, 2010; Schwartz et al. in press) indicating these samples underwent more intensive alteration/metamorphism. The Atg-serpentinites samples also contain higher abundances of carbonate than the Lz-serpentinites. A comparison between fluid-mobile element concentrations in two serpentine phases revealed that the Atg-serpentinites have been depleted in FME (Li, As, Au, S, Pb, U, Ba, Sr except Sb and Cs) relative to the lesser altered Lz-serpentinites indicating these elements have been remobilised during transition of lizardite to antigorite. This is the first time that gold has observed to be mobilising during transition of lizardite to antigorite. The talc-rich rocks have spatial and petrologic association with serpentinite protoliths. These rocks are the metasomatic products of intensive prograde metamorphism/alteration within the fault and shear zones.

Carbon, O and Sr isotopic compositions of carbonated serpentinites, metavolcanics and pure carbonate veins are used to constrain the origin of the carbonating fluid. Isotopic data of pure carbonate veins in shear zones show large flux of mantle $CO_2$-rich fluid in the form of pervasive carbonate veins and alteration in the ophiolitic rocks during Neoproterozoic. The C isotopic value of serpentinites indicates that they have undergone carbonation from mantle derived C-rich fluid while the radiogenic Sr and O values in serpentinites indicate later modification by surface fluid such as meteoric water, connate fluid or seawater. The Atg-serpentinites with intensive carbonate alteration represent isotopic values closer to mantle signature.

**Keywords**
Serpentinite, Carbonation, (C, O Sr) isotopes, Fluid-mobile elements, Gold, Central Eastern Desert

Fluid inclusion studies in carbonate veins contain abundant carbonic ($CO_2$±$CH_4$±$N_2$) and aqueous-carbonic ($H_2O$-NaCl-$CO_2$±$CH_4$) fluid inclusions with low salinity (<7 wt% NaCl eq.), similar to those reported from gold-rich vein deposits in CED showing the important role of low salinity $CO_2$-rich fluid in remobilising of gold in the ophiolitic rocks of Neoproterozoic. Based on fluid inclusion microthermometry, carbonate alteration occurred at temperature of 300 ± 30˚C and pressure of 0.7 to 1.6 kbar corresponding to a depth of ~2.6 to ~6 km. Based on isotopic data and element variations, we propose that FME redistribution during transition of lizardite to antigorite was strongly related to the large flux of $CO_2$ from the mantle. Pervasive carbonate veins and related alteration products in CED representing a natural analogue of mantle degassing and crustal $CO_2$ sequestration in Neoproterozoic.

## 1. Introduction

The migration of carbonate-rich solutions was common during the evolution of the Arabian-Nubian Shield (ANS), forming veins and dikes, and causing diffuse and pervasive carbonation of basement rocks (Stern and Gwinn, 1990). Ophiolitic peridotites are common in the ophiolitic fragments that occur in the CED (Sultan et al. 1986). They are commonly highly altered and sheared but studies of major element and relict mineral phases indicate that these were depleted harzburgite, which probably formed in a forearc ~740 Ma (Kröner et al. 1992; Stern et al. 2004). The pervasive carbonation that is focused along faults and shear zones is abundant in the ophiolitic ultramafic rocks implying huge fluxes of $CO_2$. Despite the abundance of this alteration, there have been few investigations into the source fluids that caused the alteration (Stern and Gwinn, 1990). The timing of these fluxes is also not clearly known but carbonation and deformation must have occurred sometime in the interval 740 Ma, the age of the ophiolites, and ~600 Ma when undeformed post-tectonic granites were emplaced (Andersen et al. 2009). Investigation of carbonation event can provide vital insight into the evolution of ANS. The carbonation of ophiolitic basement has a global association with gold mineralisation (e.g., Barnes et al. 1973; Buisson and Leblanc, 1985, 1986; Aydal, 1990; Koç and Kadıoğlu, 1996; Uçurum, 2000). This economic association has led to heightened interest in the carbonated ophiolitic basement of the ANS which hosts a number of gold deposits (Oweiss et al. 2001; Botros, 2002, 2004; Ramadan, 2002; Zoheir and Lehmann; 2011, Azer, 2013).

Previous isotopic investigations in Eastern Desert (ED) revealed that intrusive carbonates of the North Eastern Desert (NED) were derived from depleted mantle, whereas those of CED reflect mixing between remobilised sedimentary carbonates and mantle fluids (Stern and Gwinn 1990). The CED is also characterized by the widespread distribution of gold deposits (Kochin and Bassyni 1968; Botros, 2002, 2004). A significant proportion of gold deposits occurs in or near carbonate altered ultramafic rocks (Abd El-Rahman, et al. 2012; Botros, 2002). The source of the $CO_2$ rich fluid that caused this carbonate alteration and its association with the gold deposits clearly needs further investigation.

In this study, we present new field and geochemical, isotopic and microthermometric data in order to determine the origin of $CO_2$-rich fluids and the conditions of alteration in ophiolitic components of Meatiq area. We also present geochemical data to investigate the extent of element mobility that occurred during carbonate alteration in these two field areas. The present work also studies the first time gold concentrations and fluid-mobile element mobility in different serpentine minerals (lizardite and antigorite varieties).

## 2. Geological setting

Meatiq study area is located about 40 km west of Red Sea within the Najd mega shear zone in the CED, (Fig. 1). The rock assemblages of the Meatiq area commonly grouped under two major tectonostratigraphic units (Loizenbauer et al. 2001; Abdeen and Greiling 2005). These are the structurally lower *infrastructure*, which is composed of Um Ba'anib granitic gneiss and upper metasediments that crop out in dome structure (Habib et al. 1985; Neumayr et al. 1996, 1998), and the overlying *suprastructure*, which includes the Neoproterozoic ophiolitic assemblages and island arc-related metavolcanics (Loizenbauer et al. 2001). The suprastructure is also known the Pan-African Nappe complex (Bregar et al. 2002). The gneissic dome structure in Meatiq area has been interpreted to be an exposure of the deeper levels of the juvenile Neoproterozoic crust with no older continental crustal content (Sturchio et al. 1983; Kröner et al. 1994; Bregar et al. 2002; Andresen et al. 2009; Liégeois and Stern 2010; Lundmark et al. 2012). The eastern and western dome margins are bounded by sinistral strike-slip shear zones whereas the northern and southern margins are defined by prominent normal faults (Wallbrecher et al. 1993) (Fig. 1). Both infrastructure and suprastructure units were intruded by syn-tectonic Abu Ziran granitoid and Abu Fannani tonalite and the post-tectonic Arieki adamellite (Loizenbauer et al. 2001).

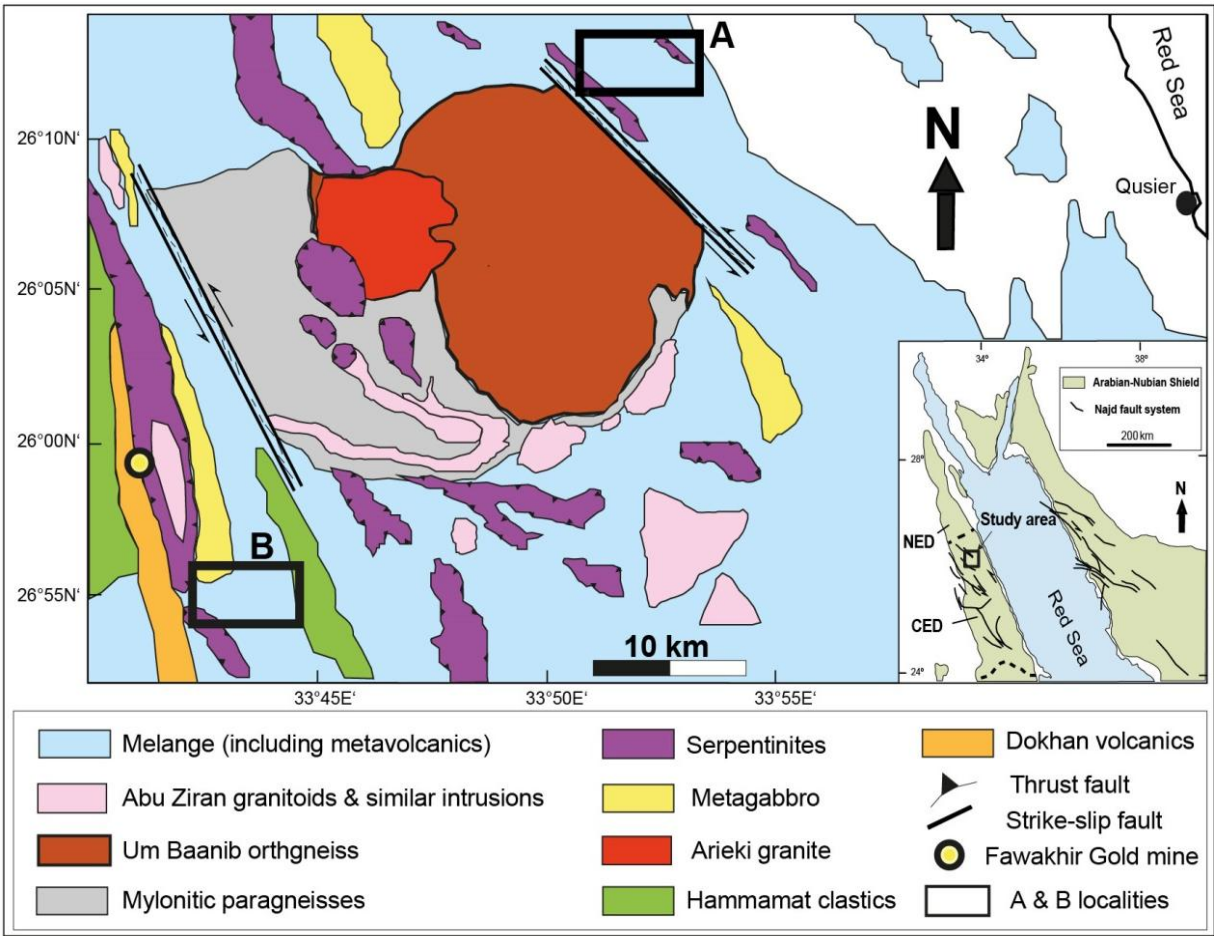


**Fig. 1** General geology map of Neoproterozoic basement in Meatiq study area (after El Gaby et al. 1984 and Loizenbauer et al. 2001), showing important lithologies, sample localities and strike-slip structures. Inset shows the location of the Meatiq area in the Central Eastern Desert (CED) of Arabian-Nubian Shield.

Neoproterozoic ophiolitic assemblages (suprastructure) are widely distributed in the Eastern Desert, especially in the CED (Stern and Hedge, 1985). The ophiolitic rocks in CED are spatially confined to the zones of major thrust faults demarcating the regional shear zones of the CED (El Gaby et al. 1988, 1990; Ali-Bik et al. 2012). These rocks in the CED are almost completely serpentinized and are typically altered to talc-carbonate bodies along shear zones (El-Sharkawi and El Bayoumi 1979; Azer and Stern 2007; Farahat, 2008; Ali-Bik et al. 2012). It is generally agreed that the ophiolitic serpentinites were derived from peridotite/harzburgite protolith (Ali-Bik et al. 2012).

## 3. Sampling

Ophiolitic rocks of the Meatiq area are the focus of this study and comprise mainly of serpentinites, talc-carbonates and amphibolites (meta-volcanics) which are in tectonic contact with the metasediments (Shackleton et al. 1980; Loizenbauer et al. 2001). Serpentinites form elongated ranges defining folded tabular bodies or sheets. The sheets of serpentinites represent the originally NW-SE brittle-ductile shear zones of the area (Fig. 1).

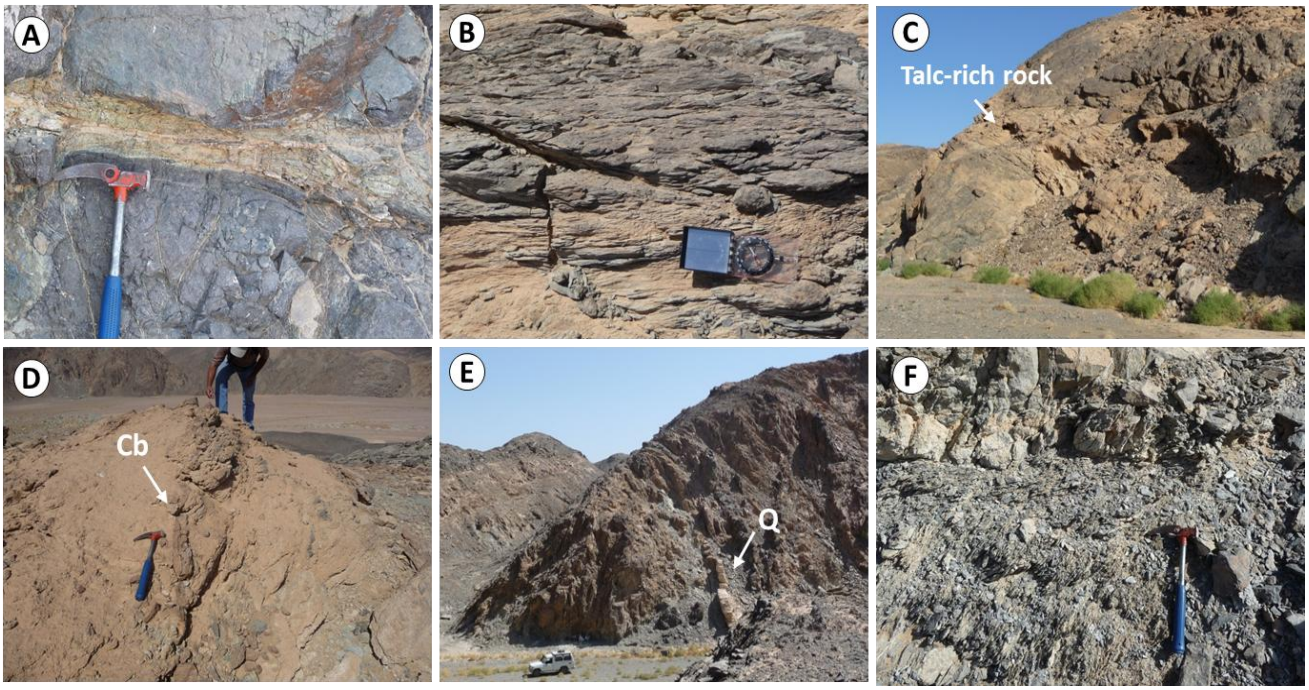


**Fig. 2** Field photographs of serpentinites and altered/sheared rocks in north and south of Meatiq Dome: (a) massive serpentinites with late chrysotile in admixture of schistose talc + magnesite; (b) sheared serpentinites; (c) talc-rich rock within the massive serpentinites; (d) magnesite/dolomite (Cb) veins within the talc-rich rocks; (e) large quartz (Q) vein cutting ophiolitic meta-volcanics and serpentinites; (e) schistose meta-volcanics

They constitute up to 10% of the total area and formed as obducted slices of oceanic lithosphere emplaced onto the island arc succession. The serpentinites occur as massive units that become sheared and foliated near contacts and along shear zones where the serpentinite is commonly altered to talc-carbonate and talc-amphibole schists (Fig. 2a, b). These rocks are variously called ‘talc-carbonate schists’, ‘Barramiya rocks’, or

'listwaenite' (Stern et al. 2004). In order to avoid confusion and considering talc as the main rock forming mineral, we call these rocks ''talc-rich''. The ophiolitic meta-volcanics of the Meatiq area have been metamorphosed at greenschist to amphibolite facies conditions (Zimmer et al. 1995; El-Sayed et al. 1999; Farahat, 2001; Stern et al. 2004). Two areas exposing fragmented ophiolitic rocks have been investigated in this study, one in the north (north locality-A) and one in the south (south locality-B) of the Meatiq dome (Fig. 1). These two localities have been selected based on different degree of serpentinites alteration, and on the availability of fresh material from quarries. The lithologies at two localities are mostly composed of serpentinite, meta-volcanic rocks, talc-carbonate and metasedimentary rocks with minor quartz and carbonate veins. Serpentinites from the south locality are black in color and "least" altered while those from the north locality are greenish grey in color and highly altered with abundant magnesite veins and talc. The talc-rich rocks are yellowish-white to greenish-cream in color contrasting strongly with the relatively darker ultramafic components (serpentinites, meta-gabbro and meta-volcanics), and are more abundant in north locality. In outcrop, they are mostly soft due to surface weathering, talcose and with schistose fabrics in places (Fig. 2c). Within the talc-rich rocks veins, nodules and irregular pockets of magnesite and dolomite with quartz and chlorite occur (Fig.2d). The quartz and carbonate veins generally have a NW-SE trend. Proximal to the southern locality large highly deformed quartz veins occur extending for 100 m within anastomosing shear zones. They are branched milky quartz veins of variable thickness (5 to 150 cm) that crosscut the other ophiolite components (Fig. 2e). The meta-volcanics are mostly massive greyish-green to black in color with foliation and schistosity in shear zones (Fig. 2f). In both localities these rocks show sharp contacts with the serpentinites.

In order to discern the source/condition of altering fluid and chemical changes during alteration/metamorphism, in Neoproterozoic ophiolitic components of Meatiq area, 26 samples of serpentinites, talc-rich rocks and meta-volcanics and associated quartz and carbonate veins were collected for the present study (Table 1).

## 4. Analytical Methods

### SEM

Polished thin sections of selected serpentinites, talc-rich rocks and meta-volcanics were also examined with a Philips XL30 FEG environmental scanning electron microscope (ESEM) at the Department of Geological Sciences, Stockholm University, operating at 20 kv and equipped with OXFORD energy dispersive analytical X-ray spectrometer. The spectrometer detects elements with atomic number > 4 (B and heavier elements).

### XRF

Twenty one samples were powdered using a hardened steel tema. Three samples (Me18, Me20 and Me27) analysed for major elements using ZSX Rigaku Primus II X-ray Fluorescence spectrometer at Geological Sciences Department, Stockholm University. The XRF analyses were carried out on fused-glass discs (flux-to-sample ratios of 5:2) for major elements. Loss on ignition (LOI) is determined by weight difference after ignition at 1000ºC. In-house standard (AGV-2) was also analysed to check the accuracy and precision of the method. The analytical precision and accuracy is better than ±1% for major elements. The results are reported in Table 2.

### LA-ICP-MS

After XRF analyses, the trace element analyses of the same fused glass discs (three samples) were performed by LA-ICP-MS, utilising an 193 nm ArF excimer laser coupled to a Thermo X-Series II quadruple ICP-MS at the PetroTectonics Facility, Stockholm University. Analytical conditions comprised a laser beam diameter of 150µm, laser frequency of 10 Hz and laser energy density of 7.5 J/cm$^2$. Nitrogen ($N_2$) gas with a flow rate of 3.0 ml/min was used to increase the sensitivity. Additionally to the external standard reference material NIST 612, BCR-2G was analyzed as known-unknown for control of the accuracy. The internal standard used was $^{29}$Si. Analysed trace elements were Sc, V, Cr, Co, Ni, Cu, Zn, As, Rb, Sr, Y, Zr, Nb, Ag, Sb, Cs, Ba, La, Ce, Pr, Nd, Sm, Eu, Gd, Tb, Dy, Ho, Er, Tm, Yb, Lu, Hf, Ta, Pb, Th and U).The XRF and LA-ICP-MS analyses results are listed in Table 2. The analytical precision and accuracy is better than ±5% for trace elements.

**Table 1** Different rock types of Meatiq study area

| Sample | Locality | Latitude | Longitude | Lithology |
|---|---|---|---|---|
| Me1 | north (A) | 26 08'05.0 | 033 55'35.4 | talc-rich rock |
| Me2 | north (A) | 26 08'05.0 | 033 55'35.4 | dolomite vein |
| Me3 | north (A) | 26 08'05.0 | 033 55'35.4 | quartz vein |
| Me4 | north (A) | 26 08'05.0 | 033 55'35.4 | meta-volcanic |
| Me5 | north (A) | 26 10'04.9 | 33 52'15.3 | antigorite-serpentinite |
| Me6 | north (A) | 26 10'04.9 | 33 52'15.3 | antigorite-serpentinite |
| Me7 | north (A) | 26 10'04.9 | 33 52'15.3 | antigorite-serpentinite |
| Me8 | north (A) | 26 10'04.9 | 33 52'15.3 | antigorite-serpentinite |
| Me9 | north (A) | 26 10'04.9 | 33 52'15.3 | antigorite-serpentinite |
| Me10 | north (A) | 26 10'13.4 | 33 52'12.7 | meta-volcanic |
| Me11 | north (A) | 26 10'13.4 | 33 52'12.7 | meta-volcanic |
| Me12 | north (A) | 26 10'13.4 | 33 52'12.7 | dolomite vein |
| Me14 | north (A) | 26 09'00.5 | 33 56'09.0 | talc-rich rock |
| Me15 | north (A) | 26 09'00.5 | 33 56'09.0 | talc-rich rock |
| Me16 | south (B) | 25 58'58.4 | 33 45'11.6 | quartz vein |
| Me17 | south (B) | 25 58'58.4 | 33 45'11.6 | talc-rich rock |
| Me18 | south (B) | 25 58'20.1 | 33 38'54.3 | meta-volcanic |
| Me19 | south (B) | 25 58'20.1 | 53 38'54.3 | meta-volcanic |
| Me20 | south (B) | 25 58'20.1 | 53 38'54.3 | meta-volcanic |
| Me21 | south (B) | 25 58'27.1 | 33 37'37.8 | lizardite-serpentinite |
| Me22 | south (B) | 25 58'27.1 | 33 37'37.8 | lizardite-serpentinite |
| Me23 | south (B) | 25 58'27.1 | 33 37'37.8 | lizardite-serpentinite |
| Me24 | south (B) | 25 58'27.1 | 33 37'37.8 | lizardite-serpentinite |
| Me26 | south (B) | 26 02'20.9 | 33 35'39.3 | chloritite |
| Me27 | north (A) | 26 10'10.4 | 33 52'18.1 | meta-volcanic |
| Me28 | north (A) | 26 10'10.4 | 33 52'18.1 | dolomite vein |

### ActLab whole rock analysis

Nineteen rock samples were analysed for major and trace elements using method of lithium metaborate/tetraborate fusion ICP Whole Rock (package code 4B) and a trace element ICP/MS (package code 4B2) at Activation Laboratories Ltd. (Actlabs), Canada. The results are reported in Table 2. The detection limits for major oxides are between 0.001 to 0.01wt.%, while the detection limits for trace elements are between 0.002 and 1ppm (except detection limits of As = 5 ppm and S = 10 ppm). Loss on ignition (LOI) is determined by weight difference after ignition at 1000ºC. Precision and accuracy was controlled by analysis of International reference materials and replicate analyses and are 1% for major elements and 2% to 5% for trace elements.

### Gold method

Gold analysis at Stockholm University was carried out using a Thermo XSeries 2 ICP-MS following the ultra-low detection limit method (<10 ppt) described in Pitcairn et al (2006). Analytical precision for Au analysis at

Stockholm was controlled through analysis of CANMET reference material TDB1 and Rocklabs reference materials OxA71 and SE44. Multiple analyses of TDB1 (n = 21), OxA71 (n =10) and SE44 (n = 4) yield values of 6.3 ± 1.7 ppb, 80 ± 8.5 ppb, and 599 ± 64 ppb respectively which compare favorably with certified values of 6.3 ± 1 ppb, 85 ± 6 ppb, and 606 ± 17 ppb. The results are listed in Table 3.

**Stable isotope (C and O)**

Carbon and oxygen isotope analysis (11 whole-rock samples and 3 dolomite veins) was undertaken using an automated triple-collector gas source mass spectrometer (Analytical Precision AP2003) linked to an automated gas preparation device at the Scottish Universities Environmental Research Centre, East Kilbride. For the C-isotope analyses, c. 2 mg of the powdered whole-rocks and carbonate veins samples were reacted with 103% phosphoric acid to produce carbon dioxide, which was then purified before analysis. Precision and accuracy were monitored by reference to long-term analysis of laboratory and international standards. Precision is better than 0.2‰ at 1σ for carbon and oxygen. Results are reported as δ‰ values relative to the V-PDB and V- SMOW scales for C- and O-isotopes, respectively (Table 4).

**Trace element and Sr isotope analyses**

Trace element and Sr isotope analysis was carried out at the National Oceanography Centre, Southampton, UK. Samples were dissolved in a hydrofluoric, perchloric and nitric acid mixture on a hot plate overnight and made up to mother solutions in hydrochloric acid. For trace element analysis the mother solutions were subsampled to produce a 4000x dilution daughter solution for ICP-MS analysis. The sub sample was dried down and then dissolved in 3% $HNO_3$ containing 5ppb In and Re and 20ppb Be to act as internal standards. The solution was analysed on a ThermoFisher Sicientific XSeries 2 ICP-MS using international rock standards to calibrate. The accuracy and precision was determined from repeated measurements of JA-2. The results are listed in Table 3.

The mother solutions were then subsampled to give approximately 1μg Sr and the Sr isolated using 50μl Sr-Spec resin columns, the column blanks were <0.1ng. The dried samples were loaded onto a single Ta filament with a Ta activator solution. $^{87}Sr/^{86}Sr$ was analysed using multidynamic peak jumping routines on ThermoFisher Scientific Triton Plus Thermal Ionisation Mass Spectrometers with a beam size of $^{88}Sr$ = 2V normalised to $^{86}Sr/^{88}Sr$=0.1194. The long term average for NBS987 on the instrument is 0.710244±0.000019 (2sd) on 138 analyses. The results are reported in Table 4.

**Fluid inclusion analysis**

Four carbonate samples (dolomite: Me2, Me12, Me28 and magnesite: Me9) and two quartz samples (Me3 and Me16) were selected from north and south localities for detailed fluid inclusion and Raman spectrometric analyses. The samples were prepared as 150 μm thick doubly polished sections. After careful documentation and selection of fluid inclusions, microthermometric and Raman spectrometric analyses were made at the Department of Geological Sciences, Stockholm University.

Microthermometric analyses were carried out in the temperature range -180° to 600°C with a Linkam THM 600 heating and cooling stage mounted on a Nikon microscope utilising a 40x long working-distance objective. The reproducibility was ±0.1°C for temperatures below +40°C and ±0.5°C for temperatures above 40°C. The stage was calibrated with synthetic fluid inclusion standards (SynFlinc®) and well-defined natural inclusions in Alpine quartz. The results are listed in Table 5.

**Raman spectrometry**

Raman spectrometric analyses were performed using a laser Raman confocal spectrometer (Horiba instrument LabRAM HR 800) equipped with a multichannel air cooled CCD detector. An Ar-ion laser ($\lambda$=514 nm) was used as the excitation source with an output power at the sample of 8 mW. The instrument was integrated with an Olympus microscope and the laser beam was focused to a spot of 1 µm with a 100x objective. The spectral resolution is about 0.3 $cm^{-1}$. The instrument was calibrated using a neon lamp and the Raman line of a silicon wafer (520.7 $cm^{-1}$). Instrument control and data acquisition was made with LabSpec 5 software.

## 5. Results:

### 5.1. Petrography and mineralogy

Two varieties of serpentinites, Lz-serpentinite (lizardite-serpentinite) and Atg-serpentinite (antigorite-serpentinite) have been identified in the study area by microscopic observations and confirmed by Raman microspectroscopy and published reference Raman spectra (Downs, 2006; the RRUFF Project).

The south locality serpentinites (Lz-serpentinite): The serpentinites are composed essentially of lizardite, chrysotile with minor carbonate and traces of talc and chlorite. In places, serpentinite minerals retain the crystal habit of the original mafic minerals. Chrysotile occurs as long fiberous veinlets cross-cutting the lizardite matrix, indicating late development of serpentinisation (Fig. 3a). Carbonates (mostly dolomitic in composition) are stained with iron-oxide and occur as scattered blocky aggregates or filling the mesh texture of original mafic mineral (Fig. 3b). Talc is rare and occurs as fine-grained aggregate associated with carbonate. The opaque minerals in the serpentinites are represented by chrome spinel and pentlandite (millerite) with traces of primary magnetite. The pentlandite (1-2% by volume) is rounded and altered to garnierite and magnetite along margins (Fig. 3c). The chrome-spinels (1-3% by volume) occur as deep-red grains with sub-rounded or irregular outlines. Magnetite occurs as primary scattered anhedral grains and as secondary rims around chromite or defines olivine and orthopyroxene relicts.

*The north locality serpentinites (Atg-serpentinite)*: this group of serpentinite composed of antigorite, talc, carbonate and minor chlorite. Antigorite is the dominant serpentine mineral and occur as flakes and shreds. In places, antigorite grains are mostly associated with carbonate and talc aggregates (Fig. 3d, e). The carbonate is mostly magnesite occurs as cryptocrystalline veinlets, crystal clusters and infilling cracks. Similar magnesite veins have been reported in CED serpentinites (Salem et al. 1997; Ghoneim et al. 1999; Azer and Stern, 2007; Ali-Bik et al. 2012). The opaque minerals are chrome-spinel and magnetite. The chrome spinel (1-4% by volume) in this group of serpentinites occurs as disseminated subhedral zoned grains Cr-magnetite outer rims (Fig. 3f). Chlorite occurs as aureoles around altered chrome spinels, indicating that this mineral formed after serpentinization. SEM-EDS analysis show that the chlorite is chrome-rich type (Kämmererite) and observed around almost chrome spinel grains as greyish-green to grey faint flakes.

*Talc-rich rocks:* These rocks comprise talc, amphibole (tremolite, anthophyllite), carbonate, chlorite, chrome-spinel, magnetite and traces of rutile. Talc mostly occurs as fine shreds, microcrystalline fibers and rarely as coarse- to medium-grained flakes with tremolite/anthophyllite and chlorite. In the study area, highly foliated amphibole-talc schists (e.g. Me15 and Me17) are distinctive within the fault zones. Syn-kinematic characteristics of these rocks are including asymmetric foliation and formation of amphibole neoblast at high angel to the mylonitic textures (Fig. 3g). The opaque minerals are mostly relicts of primary chrome-spinels

and secondary Cr-magnetite which have experienced brittle brecciation. Chlorite is mostly encloses chrome spinel with subordinate embedded in the talc groundmass (Fig. 3h).

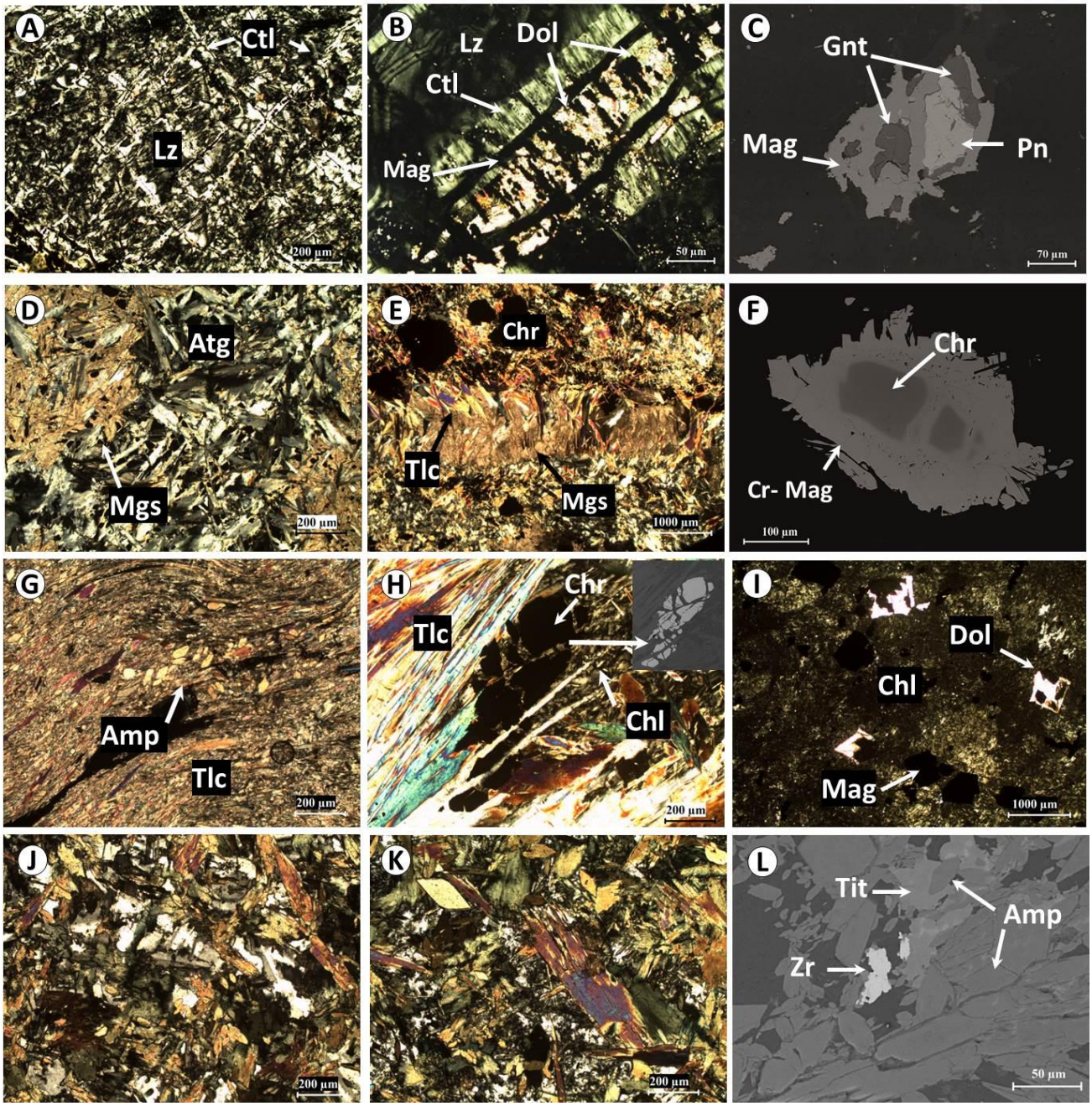


**Fig.3** Photomicrographs (a, b, d, e, g, h, I, j and k) and back-scattered electron (BSE) images (c, f and l) of the investigated ophiolitic rocks in Meatiq area. (a) serpentine dominated by lizardite (Lz) and later chrysotile (Ctl) veins in south locality; (b) late chrysotile and carbonate diffusive veinlets invaded lizardite-rich serpentinite; (c) alteration of primary pentlandite (Pn) to garnierite (Gnt) and magnetite (Mag) in Lz-serpentinite; (d) antigorite (Atg) serpentinite with magnesite (Mgs), north locality; (e) antigorite-rich serpentinite invaded by magnesite vein with talc (Tlc); (f) chrome-spinel alteration to Cr-magnetite (light-grey) with preservation of unaltered chromite (Chr) in core (dark-grey); (g) dynamically crystallised talc to amphibole (Amp) in highly schistose talc-rich rocks; (h) brecciated chromite in talc-rich rock embedded in Cr-rich chlorite (Chl) and talc; (i) Chloritite sample, mostly composed of chlorite with minor dolomite (Dol) and magnetite; (j) least altered meta-volcanic with albite-twinned plagioclase and amphibole; (k) highly metamorphosed meta-volcanic with tremolite and hornblende in groundmass of fine grained recrystallised albite; (l) titanite (Tit) and zircon (Zr) embedded in amphibole-rich meta-volcanics.

*Carbonate veins:* the carbonate veins are mostly dolomite and magnesite with minor ankerite. The carbonates are variably stained with iron oxides. Some relicts of talc flakes are enclosed between carbonate aggregates. The presence of the talc relict indicates a progressive talc replacement by carbonates. The opaque minerals in carbonate veins include magnetite and chromite, which occur as disseminated aggregates of fine to medium grain size. Traces of accessory zircon and monazite have been also observed in dolomite veins.

*Chloritite:* is a monomineralic dark green rock composed of mostly chlorite and minor magnetite. Sample Me26 is composed of very fine-grained clinochlore with euhedral magnetite and minor of dolomite (Fig. 3i).

*Meta-volcanics:* The meta-volcanics have been variably metamorphosed/altered under greenschist to lower amphibolite facies conditions. They consist mostly of medium- to fined-grained amphibole, plagioclase, chlorite and epidote. In least metamorphosed/altered variety, the plagioclase with albite-twining is present while in the high metamorphosed/altered verity the untwined recrystallised albite occupies the groundmass (Fig. 3j). In highly metamorphosed variety (amphibole-rich; e.g. hornblende actinolite/tremolite), primary texture has widely obliterated, preventing the determination of protolith (Fig. 3k). Accessory phases in meta-volcanics are presented mainly by fine-grained zircon and titanite with trace pyrite (Fig. 3l).

## 5.2. **Petrochemistry**

### Major elements variations

The chemical composition of different ophiolitic sequences in Meatiq area; including two groups of serpentinites, talc-rich rocks, meta-volcanics, and chloritite are reported in Table 2. Some major elements of analysed ophiolitic components of study area are also plotted comparatively in harker-type diagrams showing their chemical variations (Fig. 4, 5).

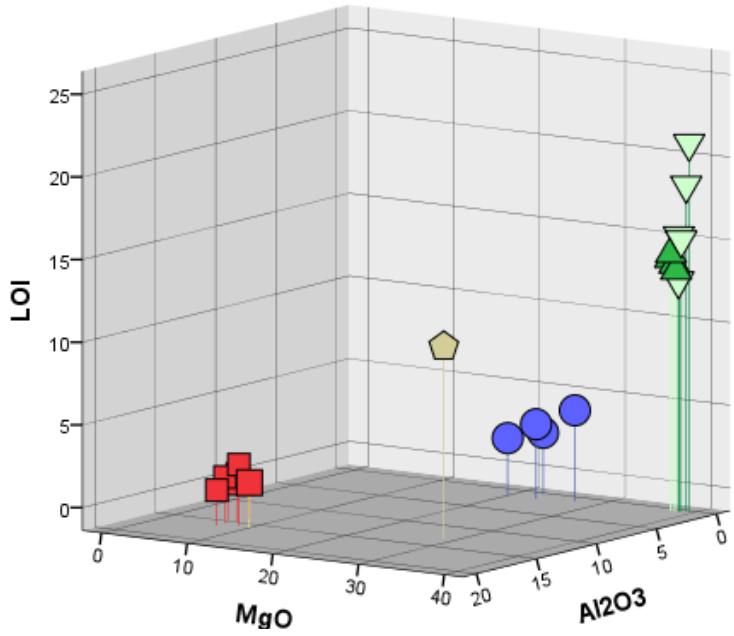


**Fig.4** Three-dimensional representation of LOI, MgO and $Al^2O^3$, showing their distribution in different ophiolitic sequences of study area; including: serpentinites (green triangle for Lz-serpentinite and light-green triangle for Atg-serpentinite), talc-rich rocks (blue circle), chloritite (green polygon) and meta-volcanic rocks (red square).

Both types of serpentinites contain abundant volatiles with LOI ranging from ~13.2 to 14.2 wt% for Lz-serpentinites and ~12.5 to 20.8 wt% for Atg-serpentinites (Fig. 4). Lz-serpentinites contain 37.7 to 40.4 wt% $SiO_2$, 0.48 to 0.55 wt% $Al_2O_3$, 37.4 to 38.2 wt% MgO, 6.7 to 7.8 wt% total Fe as $Fe_2O_3$ and 0.27 to 1.1 wt% CaO with traces of other major oxides. The Atg-serpentinites show relatively similar range of majors except for $SiO_2$ which ranges from 32.7 to 40.2 wt%.

The talc-rich rocks are another group of ophiolitic components which contain 2.1 to 4.1 wt% LOI, 55.5 to 59.2 wt% $SiO_2$, 0.38 to 1.6 wt% $Al_2O_3$, ~20.1 to 27.1 wt% MgO, ~4.8 to 8 wt% total Fe as $Fe_2O_3$, 2.7 to 12.6 wt% CaO, and traces of other major oxides.

The meta-volcanics of study area contain 43.4 to 52.6 wt% $SiO_2$, 14.8 to 16.3 wt% $Al_2O_3$, ~6 to ~10 wt% MgO, 8.1 to 13.8 wt% Fe as $Fe_2O_3$, 8 to ~13 wt% CaO, 1.8 to 4.4 $Na_2O$, 0.5 to 1.5 wt% $TiO_2$ and traces of other oxides. These major element characteristics suggest basalt to andesitic composition for the meta-volcanics of Meatiq area, comparable to the mean composition for the ANS ophiolitic volcanics (Stern et al. 2004).

Chloritite sample (Me26) contains 10.2 wt% LOI, 27.1 wt% $SiO_2$, ~13.1 wt% $Al_2O_3$, 28.7 wt% MgO, ~17.4 $Fe_2O_3$, 13.8 wt% CaO, ~1.6 wt% $TiO_2$ and traces of other oxides which indicate the monomineralic nature of this rock.

**Table 2** Whole chemical composition of different rock types and carbonate veins in Meatiq study area

| Lithology | Lz-serpentinite | | | | Atg-serpentinite | | | | | Talc-rich rocks | | | |
|---|---|---|---|---|---|---|---|---|---|---|---|---|---|
| sample | Me21 | Me22 | Me23 | Me24 | Me5 | Me6 | Me7 | ME8 | Me9 | Me1 | Me14 | Me15 | Me17 |
| $SiO_2$ (wt%) | 40.43 | 39.29 | 38.6 | 37.76 | 40.26 | 36.97 | 34.37 | 37.12 | 32.75 | 55.5 | 59.23 | 58.95 | 57.92 |
| $Al_2O_3$ | 0.51 | 0.5 | 0.48 | 0.55 | 0.48 | 0.51 | 0.31 | 0.51 | 0.12 | 1.66 | 1 | 0.38 | 1.57 |
| $Fe_2O_3$(T) | 6.78 | 7.28 | 7.49 | 7.81 | 7.63 | 9.07 | 7.36 | 6.3 | 5.86 | 7.6 | 4.8 | 5.33 | 7.98 |
| MnO | 0.07 | 0.084 | 0.082 | 0.1 | 0.065 | 0.087 | 0.136 | 0.089 | 0.114 | 0.155 | 0.06 | 0.118 | 0.117 |
| MgO | 38.22 | 37.99 | 37.47 | 37.68 | 38.43 | 38.52 | 39.11 | 38.81 | 39.18 | 20.16 | 27.08 | 22.52 | 23.36 |
| CaO | 0.27 | 0.76 | 1.11 | 1.13 | 0.02 | 0.02 | 0.03 | 0.02 | 0.05 | 12.6 | 2.71 | 11.24 | 6.55 |
| $Na_2O$ | 0.01 | 0.01 | 0.01 | 0.01 | 0.01 | 0.01 | 0.01 | 0.01 | 0.01 | 0.08 | 0.03 | 0.05 | 0.09 |
| $K_2O$ | 0.01 | 0.01 | 0.01 | 0.01 | 0.01 | 0.01 | 0.01 | 0.01 | 0.01 | 0.01 | 0.01 | 0.01 | 0.01 |
| $TiO_2$ | 0.002 | 0.001 | 0.003 | 0.002 | 0.002 | 0.001 | 0.002 | 0.001 | 0.001 | 0.025 | 0.006 | 0.014 | 0.033 |
| $P_2O_5$ | 0.01 | 0.01 | 0.02 | 0.01 | 0.01 | 0.01 | 0.01 | 0.01 | 0.01 | 0.01 | 0.01 | 0.01 | 0.01 |
| LOI | 13.19 | 13.55 | 13.85 | 14.19 | 12.55 | 15.28 | 18.34 | 15.06 | 20.84 | 2.1 | 4.1 | 2.34 | 3.13 |
| Total | 99.48 | 99.46 | 99.11 | 99.22 | 99.43 | 100.5 | 99.67 | 97.92 | 98.92 | 99.89 | 99.01 | 101 | 100.8 |
| Sc (ppm) | 7 | 7 | 6 | 6 | 8 | 8 | 8 | 8 | 3 | 5 | 5 | 5 | 24 |
| V | 49 | 52 | 67 | 29 | 36 | 41 | 31 | 35 | 19 | 53 | 27 | 47 | 71 |
| Cr | 3020 | 2970 | 2520 | 2160 | 2650 | 2990 | 2360 | 2290 | 1650 | 1670 | 1990 | 230 | 1830 |
| Co | 99 | 100 | 89 | 91 | 85 | 92 | 114 | 70 | 93 | 74 | 75 | 46 | 60 |
| Ni | 2330 | 2150 | 2000 | 2210 | 2110 | 2070 | 2250 | 2230 | 2370 | 1600 | 2020 | 619 | 371 |
| Cu | 1 | 1 | 1 | 5 | 5 | 1 | 1 | 1 | 1 | 22 | 1 | 1 | 1 |
| Zn | 34 | 32 | 31 | 28 | 30 | 29 | 36 | 32 | 30 | 54 | 55 | 23 | 39 |
| Rb | _ | _ | _ | _ | _ | _ | _ | _ | _ | 1 | 1 | 1 | 1 |
| Sr | _ | _ | _ | _ | _ | _ | _ | _ | _ | 25 | 2 | 5 | 8 |
| Y | 0.8 | 0.8 | 2.1 | 0.5 | 0.5 | 0.5 | 0.5 | 0.5 | 0.5 | 0.6 | 0.5 | 0.5 | 0.9 |
| Zr | 2 | 1 | 1 | 1 | 1 | 1 | 1 | 1 | 1 | 1 | 2 | 1 | 3 |
| Nb | 0.2 | 0.2 | 0.2 | 0.2 | 0.2 | 0.2 | 0.2 | 0.2 | 0.2 | 0.2 | 0.2 | 0.2 | 0.2 |
| Sb | _ | _ | _ | _ | _ | _ | _ | _ | _ | 0.2 | 0.2 | 0.2 | 0.2 |
| Cs | _ | _ | _ | _ | _ | _ | _ | _ | _ | 0.1 | 0.1 | 0.1 | 0.1 |
| Ba | 3 | 3 | 4 | 4 | 3 | 3 | 3 | 3 | 3 | 3 | 3 | 3 | 3 |
| La | 1.27 | 0.72 | 0.98 | 0.22 | 0.14 | 0.28 | 0.07 | 0.16 | 0.18 | 0.17 | 0.16 | 0.22 | 0.34 |
| Ce | 2.34 | 1.48 | 1.82 | 0.26 | 0.19 | 0.4 | 0.08 | 0.2 | 0.23 | 0.26 | 0.27 | 0.42 | 0.67 |
| Pr | 0.29 | 0.19 | 0.22 | 0.03 | 0.01 | 0.04 | 0.01 | 0.02 | 0.02 | 0.06 | 0.03 | 0.05 | 0.08 |
| Nd | 1.13 | 0.68 | 0.75 | 0.05 | 0.05 | 0.05 | 0.05 | 0.05 | 0.05 | 0.2 | 0.05 | 0.05 | 0.24 |
| Sm | 0.14 | 0.09 | 0.1 | 0.01 | 0.01 | 0.01 | 0.01 | 0.01 | 0.01 | 0.03 | 0.01 | 0.01 | 0.04 |
| Eu | 0.031 | 0.017 | 0.035 | 0.007 | 0.005 | 0.005 | 0.005 | 0.005 | 0.005 | 0.073 | 0.005 | 0.006 | 0.038 |
| Gd | 0.17 | 0.11 | 0.15 | 0.01 | 0.01 | 0.01 | 0.01 | 0.01 | 0.01 | 0.09 | 0.01 | 0.04 | 0.1 |
| Tb | 0.02 | 0.02 | 0.03 | 0.01 | 0.01 | 0.01 | 0.01 | 0.01 | 0.01 | 0.01 | 0.01 | 0.01 | 0.02 |
| Dy | 0.14 | 0.1 | 0.2 | 0.02 | 0.01 | 0.02 | 0.01 | 0.01 | 0.02 | 0.07 | 0.03 | 0.06 | 0.11 |
| Ho | 0.02 | 0.02 | 0.06 | 0.01 | 0.01 | 0.01 | 0.01 | 0.01 | 0.01 | 0.02 | 0.01 | 0.01 | 0.03 |
| Er | 0.05 | 0.04 | 0.22 | 0.02 | 0.01 | 0.01 | 0.01 | 0.01 | 0.01 | 0.05 | 0.03 | 0.05 | 0.09 |
| Tm | 0.005 | 0.005 | 0.03 | 0.005 | 0.005 | 0.005 | 0.005 | 0.005 | 0.005 | 0.006 | 0.005 | 0.009 | 0.014 |
| Yb | 0.03 | 0.02 | 0.17 | 0.02 | 0.01 | 0.01 | 0.01 | 0.01 | 0.01 | 0.03 | 0.02 | 0.08 | 0.1 |
| Lu | 0.005 | 0.003 | 0.025 | 0.003 | 0.002 | 0.002 | 0.002 | 0.002 | 0.002 | 0.003 | 0.003 | 0.016 | 0.017 |
| Hf | 0.1 | 0.1 | 0.1 | 0.1 | 0.1 | 0.1 | 0.1 | 0.1 | 0.1 | 0.1 | 0.1 | 0.1 | 0.1 |
| Ta | 0.01 | 0.01 | 0.01 | 0.01 | 0.01 | 0.01 | 0.01 | 0.01 | 0.01 | 0.01 | 0.01 | 0.01 | 0.01 |
| Pb | 3 | 3 | 3 | 3 | 3 | 4 | 3 | 3 | 3 | 4 | 3 | 3 | 4 |
| Th | 0.1 | 0.05 | 0.05 | 0.05 | 0.05 | 0.05 | 0.05 | 0.05 | 0.05 | 0.05 | 0.05 | 0.05 | 0.05 |
| U | _ | _ | _ | _ | _ | _ | _ | _ | _ | 0.04 | 0.02 | 0.03 | 0.03 |
| As | _ | _ | _ | _ | _ | _ | _ | _ | _ | 66 | 5 | 5 | 5 |
| S (%) | _ | _ | _ | _ | _ | _ | _ | _ | _ | 0.001 | 0.002 | 0.001 | 0.001 |
| Au (ppb) | _ | _ | _ | _ | _ | _ | _ | _ | _ | 1.02 | 0.30 | 1.41 | 0.24 |
| (Eu/Eu*)n | 0.6 | 0.5 | 0.9 | 2.1 | 1.5 | 1.5 | 1.5 | 1.5 | 1.5 | 4.3 | 1.5 | 0.9 | 1.8 |
| (La/Sm)n | 5.9 | 5.2 | 6.3 | 14.2 | 9.0 | 18.1 | 4.5 | 10.3 | 11.6 | 3.7 | 10.3 | 14.2 | 5.5 |
| (La/Yb)n | 30.4 | 25.8 | 4.1 | 7.9 | 10.0 | 20.1 | 5.0 | 11.5 | 12.9 | 4.1 | 5.7 | 2.0 | 2.4 |
| (La/Lu)n | 27.2 | 25.7 | 4.2 | 7.9 | 7.5 | 15.0 | 3.8 | 8.6 | 9.6 | 6.1 | 5.7 | 1.5 | 2.1 |
| Total REE | 5.6 | 3.5 | 4.8 | 0.7 | 0.5 | 0.9 | 0.3 | 0.5 | 0.6 | 1.1 | 0.6 | 1.0 | 1.9 |

** Samples analysed at Stockholm University; *** samples analysed at NOC, University of Southampton; other analysed at Activation Laboratories, Canada.

**Table 2 continued**

| Lithology | Meta-volcanics | | | | | | | Chloritite | Dolomite veins*** | | |
|---|---|---|---|---|---|---|---|---|---|---|---|
| sample | Me4 | Me10 | Me11 | Me18** | Me19 | Me20** | Me27** | Me26 | Me2 | Me12 | Me28 |
| $SiO_2$ (wt%) | 52.12 | 49.56 | 49.19 | 56.96 | 52.91 | 55.08 | 43.41 | 27.14 | _ | _ | _ |
| $Al_2O_3$ | 13.84 | 14.85 | 16.3 | 15.53 | 15.63 | 14.87 | 15.87 | 13.08 | _ | _ | _ |
| $Fe_2O_3$(T) | 12.15 | 13.43 | 12.19 | 8.18 | 9.66 | 10.15 | 13.81 | 17.38 | _ | _ | _ |
| MnO | 0.207 | 0.195 | 0.202 | 0.16 | 0.14 | 0.19 | 0.30 | 0.18 | _ | _ | _ |
| MgO | 7.02 | 5.99 | 6.73 | 6.62 | 8.37 | 7.14 | 9.94 | 28.70 | _ | _ | _ |
| CaO | 8.31 | 8.54 | 9.83 | 9.94 | 8.27 | 8.01 | 12.98 | 0.31 | _ | _ | _ |
| $Na_2O$ | 3.81 | 4.39 | 4.28 | 2.00 | 2.85 | 3.39 | 1.82 | 0.01 | _ | _ | _ |
| $K_2O$ | 0.19 | 0.42 | 0.37 | 0.10 | 0.07 | 0.12 | 0.77 | 0.01 | _ | _ | _ |
| $TiO_2$ | 1.556 | 1.216 | 0.813 | 0.52 | 0.67 | 1.02 | 1.10 | 1.58 | _ | _ | _ |
| $P_2O_5$ | 0.13 | 0.07 | 0.06 | 0.00 | 0.07 | 0.04 | 0.00 | 0.19 | _ | _ | _ |
| LOI | 0.83 | 0.83 | 0.75 | 1.40 | 2.28 | 1.51 | 1.33 | 10.25 | _ | _ | _ |
| Total | 100.2 | 99.5 | 100.7 | 101.4 | 100.9 | 101.5 | 101.3 | 98.81 | _ | _ | _ |
| Sc (ppm) | 50 | 41 | 40 | 40 | 38 | 45 | 50 | 51 | 3.9 | 6.8 | 3.3 |
| V | 357 | 364 | 374 | 225 | 273 | 288 | 416 | 290 | 3.0 | 0.2 | 0.1 |
| Cr | 130 | 40 | 30 | 134 | 410 | 52 | 53 | 1030 | 7.5 | 3.6 | 3.3 |
| Co | 54 | 39 | 45 | 32 | 36 | 40 | 52 | 85 | 0.7 | 12.5 | 9.5 |
| Ni | 52 | 42 | 31 | 60 | 104 | 41 | 40 | 263 | 4.2 | 33.0 | 33.6 |
| Cu | 31 | 275 | 192 | 61 | 38 | 46 | 4 | 1 | 0.6 | 11.2 | 0.2 |
| Zn | 79 | 77 | 75 | 56 | 54 | 68 | 77 | 39 | _ | _ | _ |
| Rb | 2 | 2 | 2 | _ | _ | _ | 11 | 1 | _ | _ | _ |
| Sr | 196 | 393 | 669 | 68 | 108 | 86 | 674 | 2 | _ | _ | _ |
| Y | 32.2 | 27.7 | 18.6 | 12.9 | 17.4 | 25.8 | 22.4 | 18.8 | 20.9 | 46.9 | 18.1 |
| Zr | 88 | 74 | 35 | 26 | 45 | 65 | 44 | 93 | _ | _ | _ |
| Nb | 3.9 | 2 | 0.2 | 1.3 | 1.2 | 1.4 | 1.1 | 3.2 | 0.036 | 0.017 | 0.016 |
| Sb | 0.2 | 1.3 | 1.3 | 0.8 | 0.7 | 0.3 | 1.1 | 0.5 | _ | _ | _ |
| Cs | 0.1 | 0.2 | 0.1 | 0.2 | 0.1 | 0.2 | 3.7 | 0.1 | 0.004 | 0.003 | 0.007 |
| Ba | 45 | 206 | 193 | 27.4 | 21.0 | 30.8 | 386.6 | 3 | 4.78 | 0.97 | 1.57 |
| La | 4.24 | 3.46 | 2.12 | 2.07 | 2.42 | 3.24 | 3.10 | 0.92 | 16.41 | 4.71 | 2.36 |
| Ce | 11.7 | 9.75 | 5.17 | 3.03 | 6.28 | 6.32 | 5.93 | 3.48 | 33.73 | 15.33 | 7.72 |
| Pr | 1.89 | 1.58 | 0.82 | 0.51 | 0.96 | 1.16 | 1.08 | 0.69 | 4.32 | 2.63 | 1.32 |
| Nd | 9.75 | 8.62 | 4.27 | 3.05 | 4.83 | 6.74 | 6.34 | 4.64 | 18.34 | 14.19 | 7.09 |
| Sm | 3.16 | 2.83 | 1.55 | 1.22 | 1.61 | 2.55 | 2.38 | 2.2 | 3.94 | 4.89 | 2.49 |
| Eu | 1.15 | 1.04 | 0.692 | 0.77 | 0.68 | 0.73 | 0.95 | 0.331 | 1.46 | 1.54 | 0.96 |
| Gd | 4.69 | 3.85 | 2.33 | 1.63 | 2.33 | 3.27 | 2.98 | 3.28 | 3.78 | 6.79 | 3.24 |
| Tb | 0.94 | 0.78 | 0.47 | 0.29 | 0.44 | 0.60 | 0.53 | 0.65 | 0.51 | 1.13 | 0.51 |
| Dy | 5.65 | 4.95 | 3.04 | 2.24 | 2.81 | 4.49 | 4.12 | 3.84 | 2.66 | 7.27 | 3.03 |
| Ho | 1.24 | 1.07 | 0.67 | 0.49 | 0.62 | 0.99 | 0.87 | 0.79 | 0.49 | 1.53 | 0.58 |
| Er | 3.54 | 3.09 | 2.03 | 1.47 | 1.85 | 2.92 | 2.63 | 2.19 | 1.25 | 4.30 | 1.48 |
| Tm | 0.586 | 0.504 | 0.34 | 0.230 | 0.297 | 0.452 | 0.412 | 0.317 | 0.17 | 0.59 | 0.19 |
| Yb | 3.55 | 3.14 | 2.18 | 1.53 | 1.96 | 2.98 | 2.71 | 1.92 | 1.05 | 3.72 | 1.16 |
| Lu | 0.578 | 0.533 | 0.365 | 0.220 | 0.323 | 0.426 | 0.376 | 0.308 | 0.14 | 0.52 | 0.16 |
| Hf | 2.2 | 1.8 | 0.9 | 0.8 | 1.0 | 1.8 | 1.3 | 2.2 | 0.008 | 0.020 | 0.008 |
| Ta | 0.22 | 0.01 | 0.01 | 0.18 | 0.01 | 0.10 | 0.06 | 0.14 | 0.003 | 0.008 | 0.003 |
| Pb | 4 | 3 | 3 | 0.9 | 3.0 | 0.3 | 3.6 | 6 | 0.882 | 3.176 | 4.908 |
| Th | 0.34 | 0.33 | 0.25 | 0.16 | 0.30 | 0.23 | 0.30 | 0.33 | 0.019 | 0.009 | 0.006 |
| U | 0.64 | 0.13 | 0.16 | 0.05 | 0.11 | 0.06 | 0.12 | 0.11 | 0.0149 | 0.0007 | 0.0004 |
| As | 5 | 5 | 5 | 2.2 | 5.0 | 2.1 | 1.5 | 6 | _ | _ | _ |
| S (%) | 0.009 | 0.006 | 0.008 | _ | 0.002 | _ | _ | 0.002 | _ | _ | _ |
| Au (ppb) | 20.79 | | 1.56 | 2.73 | 0.29 | 0.34 | _ | 0.15 | _ | _ | _ |
| (Eu/Eu*)n | 0.9 | 1.0 | 1.1 | 1.7 | 1.1 | 0.8 | 1.1 | 0.4 | 1.2 | 0.8 | 1.0 |
| (La/Sm)n | 0.9 | 0.8 | 0.9 | 1.1 | 1.0 | 0.8 | 0.8 | 0.3 | 2.7 | 0.6 | 0.6 |
| (La/Yb)n | 0.9 | 0.8 | 0.7 | 1.0 | 0.9 | 0.8 | 0.8 | 0.3 | 11.3 | 0.9 | 1.5 |
| (La/Lu)n | 0.8 | 0.7 | 0.6 | 1.0 | 0.8 | 0.8 | 0.9 | 0.3 | 12.6 | 1.0 | 1.6 |
| Total REE | 52.7 | 45.2 | 26.0 | 18.8 | 27.4 | 36.9 | 34.4 | 25.6 | 88.3 | 69.1 | 32.3 |

** Samples analysed at Stockholm University; *** samples analysed at NOC, University of Southampton; other analysed at Activation Laboratories, Canada.

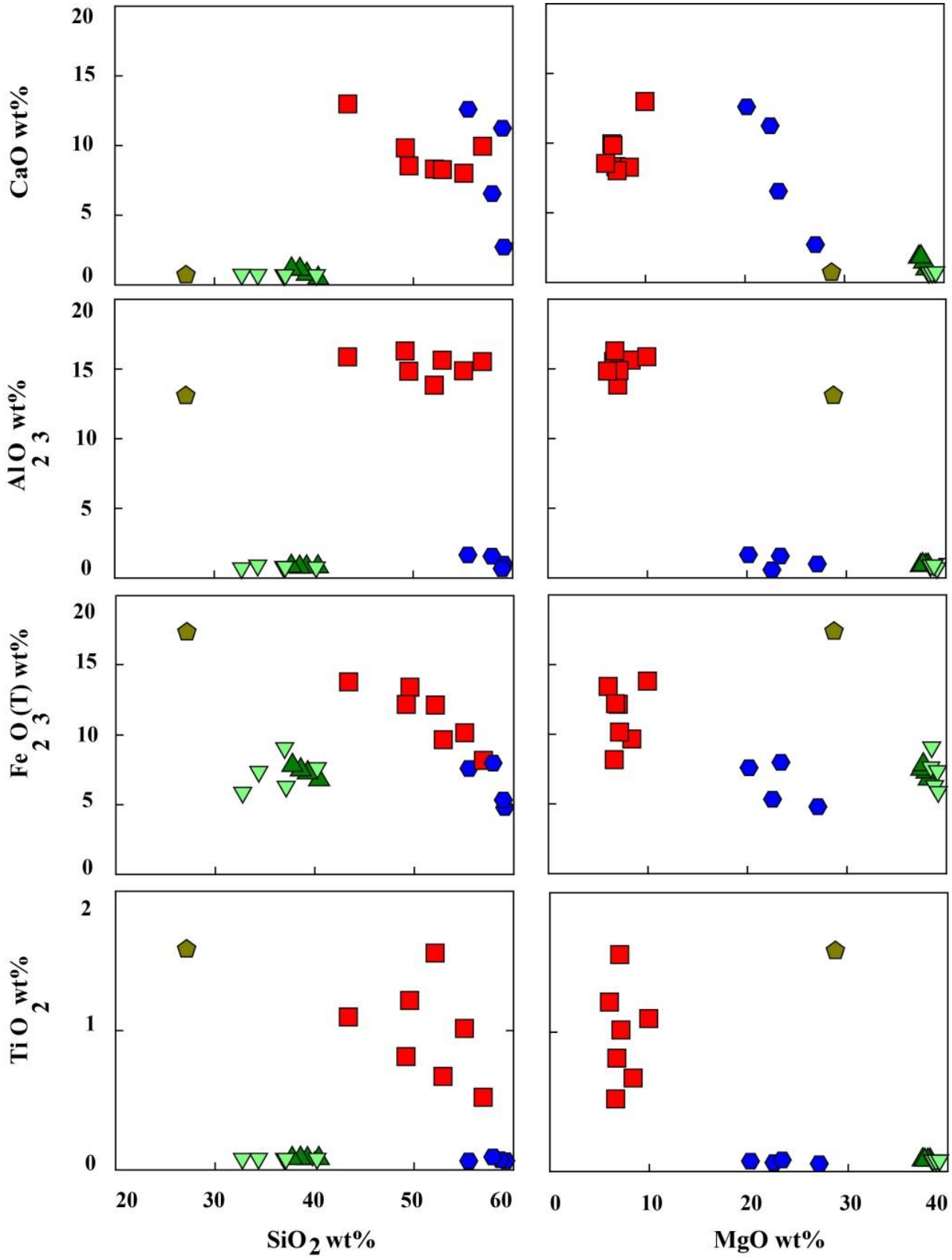


**Fig. 5** Harker-type diagrams showing major elements variations in different altered/metamorphosed ophiolitic sequences. The symbols are the same as for Fig. 4.

### Trace element variations

The results for the trace elements have been divided into three different subgroups; 1) HFSE and Cr, Ni,Co and Y, 2) fluid mobile elements (FME); Li, As, S, Sb, Pb, U, Ba, Sr, Cs and Au and 3) REE. The results are reported in Table 2 and 3. The FME comprise a group of large ion lithophile and chalcophile elements that have shown to be mobile during alteration of serpentinites (e.g. Hattori and Guillot, 2003, 2007; Deschamps et al. 2010, 2011, 2012). Gold is also included in this group due to its common association with As and S. Of the FME group, elements such as Li, Pb, U, Ba, Sr and Cs have been analysed on both types of serpentinites at NOC, University of Southampton while the analysis of As, S and Sb of serpentinites, talc-rich rocks, meta-volcanics and chloritite sample have been carried out at Activation Laboratories, Canada. The gold analysis has been analysed at Stockholm University.

### HFSE and Cr, Ni and Co

In Meatiq study area, serpentinites show relatively high absolute concentrations of Cr, Ni and Co. The mean Cr, Ni and Co concentrations of Lz-serpentinites are ~2670 ppm, ~2170 ppm and ~95 ppm, respectively. These values in Atg-serpentinites are ~2390 ppm for Cr, 2200 ppm for Ni and 90 ppm for Co. The meta-volcanics contain lowest Cr (~121 ppm), Ni (~53 ppm) and Co (~43 ppm) content while the talc-rich rocks and chloritite sample show concentrations between the two end members (Fig. 6). Meta-volcanics and chloritite sample contain the highest concentrations of incompatible high field strength elements (e.g., Zr, Hf, Nb and Ta) and Y if compared with the other ophiolitic rocks. Zirconium (and Hf, Nb and Ta) and Y show broad variations in meta-volcanics and range from ~25 to 88 ppm and ~12 to 47 ppm, respectively while the serpentinites and talc-rich rocks show distinctly lowest concentrations (mostly <1ppm) (Fig. 6). The chloritite sample contains 93 ppm Zr which is the highest value in the samples analysed in this study.

### Fluid-mobile elements

The Lz-serpentinites contain 573 to 5697 ppb Li, 5 to 64 ppm As, ~280 to ~730 ppm S, 0.2 to 0.7 ppm Sb, 97 to 439 ppb Pb, 4.05 to 503.6 ppb U, 645.5 to 2483 ppb Ba, 5.8 to 69.8 ppm Sr, 2.65 to 44.9 ppb Cs and 3.6-11.2 ppb Au. The Atg-serpentinites contain relatively lower concentrations of 407.1 to 566.5 ppb Li, 5 ppm As, 10 to 30 ppm S, 28.8 to 52.8 ppb Pb, 0.87 to 46.7 ppb U, 167.7 to 522.2 ppb Ba, 0.23 to 0.44 ppm Sr and 0.8-7.7 ppb Au but higher concentrations of 0.8 to 1.9 ppm Sb and 18.9 to 157 ppb Cs if compared to Lz-serpentinites. The talc rich, meta-volcanics and chloritite sample have not been analysed for Li, Pb, U, Ba, Sr and Cs at NOC and thus the other FME (As, S and Au) will be discussed here. The talc-rich rocks contain 5 ppm As, 10 to 20 ppm S and 0.24 to 1.4 ppb Au. The meta-volcanics contain 1.5 to 5 ppm As, 20 to 90 ppm S and 0.28 to 2.72 ppb Au with anomalous concentrations of gold in sample Me4 (~20.8 ppb). The chloritite sample (Me26) contains 6 ppm As, 20 ppm S and 0.15 Au.

### REE

Chondrite-normalised rare earth element patterns of different ophiolitic rocks, using the normalising values of McDonough and Sun (1995), are presented in figure 7. Total REE concentration in two serpentinite phases reveal that Lz-serpentinites contain relatively higher REE concentrations ($\Sigma$REE = 0.67-5.64 ppm) if compared to Atg-serpentinites ($\Sigma$REE = 0.29-0.86 ppm).

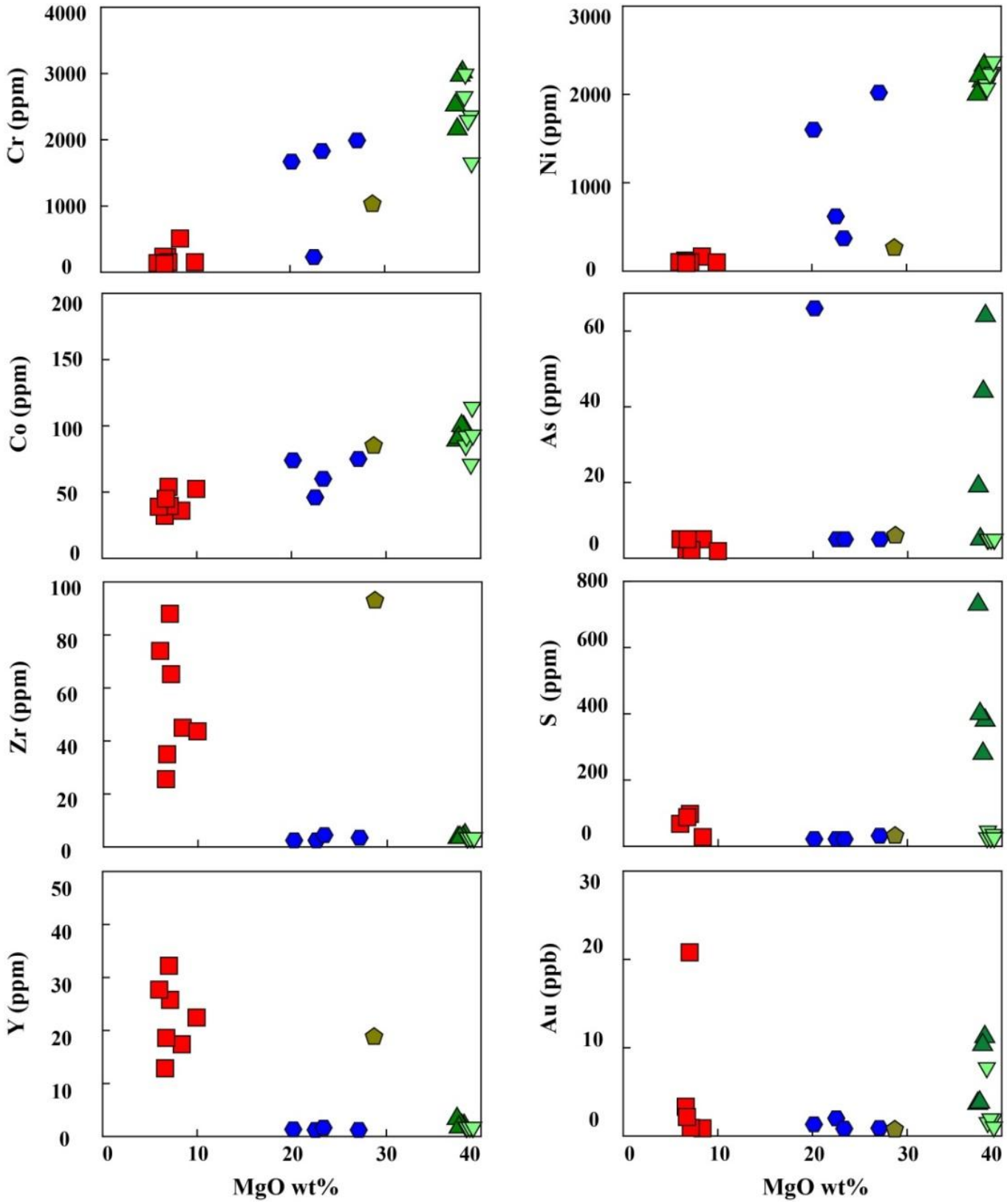


**Fig. 6** Harker-type diagrams showing chemical variation in trace elements of different altered/metamorphosed ophiolitic sequences. The symbols are the same as for Fig. 4.

**Table 3** Fluid-mobile elements composition of different serpentinites in Meatiq study area.

| Litholoogy | Lz-serpentinite | | | | Atg-serpentinite | | | | |
|---|---|---|---|---|---|---|---|---|---|
| Sample | Me21 | Me22 | Me23 | Me24 | Me5 | Me6 | Me7 | Me8 | Me9 |
| Au* (ppb) | 11.2 | 10.3 | 3.7 | 3.8 | 7.7 | 1.4 | 1.8 | 1.8 | 0.9 |
| Li (ppb) | 5697.0 | 5027.0 | 4533.0 | 573.3 | 479.2 | 430.4 | 413.4 | 407.1 | 566.5 |
| Ba (ppb) | 645.5 | 1512.0 | 2483.0 | 2174.0 | 0.0 | 225.9 | 341.1 | 167.7 | 522.2 |
| Pb (ppb) | 109.8 | 97.2 | 103.3 | 439.5 | 52.8 | 44.4 | 41.5 | 43.4 | 28.8 |
| U (ppb) | 254.5 | 374.6 | 503.6 | 4.05 | 46.7 | 39.1 | 0.87 | 1.54 | 5.69 |
| Cs (ppb) | 44.4 | 32.3 | 44.9 | 2.65 | 157.0 | 63.4 | 65.44 | 83.23 | 18.92 |
| Sr (ppm) | 5.82 | 18.5 | 69.8 | 56.4 | 0.23 | 0.42 | 0.31 | 0.40 | 0.45 |
| Sb**(ppm) | 0.7 | 0.5 | 0.2 | 0.2 | 1.9 | 1.3 | 1.7 | 0.8 | 0.8 |
| As** (ppm) | 64.0 | 44.0 | 19.0 | 5.0 | 5.0 | 5.0 | 5.0 | 5.0 | 5.0 |
| S**(ppm) | 380 | 280 | 730 | 400 | 10 | 30 | 20 | 10 | 10 |

*Samples analysed at Stockholm University; **samples analysed at Activation Laboratories, Canada; other analysed at NOC, University of Southampton.

Both serpentinite phases show relative enrichment in LREE over HREE, whereby the Lz-serpentinites are characterized by more enrichment ($La_N/Yb_N$ = 4.13-30.36) in comparison with the Atg-serpentinites ($La_N/Yb_N$ = 5.02-20.08). The Lz-serpentinites exhibit slightly negative to no Eu anomalies [~(Eu/Eu*) = 1.03] except for sample (Me21) which shows positive Eu anomaly [(Eu/Eu*) = 2.14]. This sample is also distinct from the other Lz-serpentinites considering lower REE enrichment and fractionation in HREE similar to Atg-serpentinites.

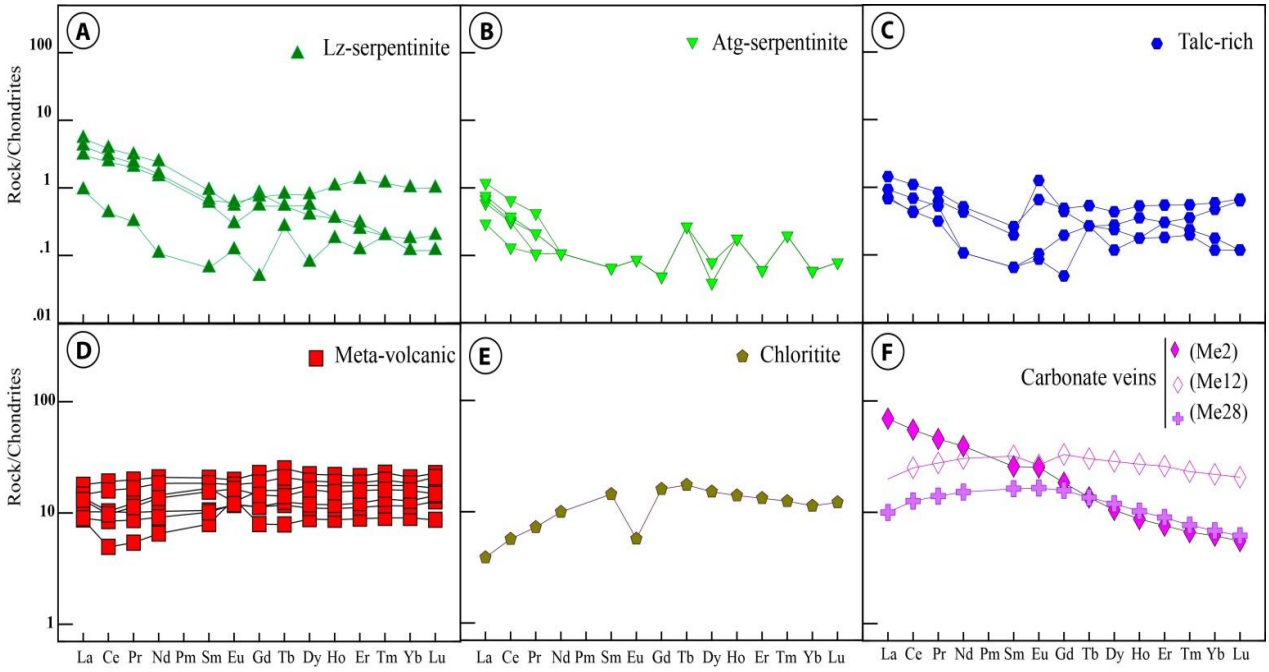


**Fig. 7** Chondrite-normalised REE concentration patterns of different ophiolitic rocks (after McDonough and Sun, 1995). Lz-serpentinites have higher concentrations of total REE than Atg-serpentinites and both phases are enriched in LREE over HREE. The talc-rich rocks are slightly enriched in LREE over HREE. Meta-volcanics show flat REE patterns with relatively wide range of total REE concentrations. The chloritite sample is depleted in LREE and shows relatively smooth HREE pattern. Carbonate veins exhibit different REE concentration patterns.

The talc-rich samples are slightly enriched in LREE ($La_N/Sm_N$ = 5.5–14.2) with no to relatively positive Eu anomalies [~(Eu/Eu*) = 2.14]. $_{The}$ general LREE pattern is similar to Atg-serpentinites but slightly higher concentrations specifically in HREE with flat pattern.

The meta-volcanics REE patterns are characterized with a wide range of absolute REE concentrations defining relatively uniform $_{flat}$ patterns ($La_N/Sm_N$ = 0.81–1.09) with no Eu anomaly ([(Eu/Eu*) = 0.77-1.07]. The chloritite sample (Me26) is depleted in LREE and has negative Eu anomaly with relatively smooth pattern in HREE. The carbonate veins exhibit different REE concentration patterns, from relatively high concentration in LREE in sample Me2 ($La_N/Lu_N$ = 12.5) to smooth REE pattern in (Me12), while they contain no Eu anomaly [(Eu/Eu*) = 0.81-1.15]. Two dolomite veins (Me2 and Me28) show clear depletion in HREE whereby the Me12 is not depleted in HREE if compared to other carbonate veins.

## 5.3. **Isotopic signature of Meatiq carbonate altered rocks and veins**

The carbon and oxygen isotope analysis, Rb and Sr concentrations and $^{87}Sr/^{86}Sr$ ratios for 12 whole-rock samples (9 serpentinites and 3 meta-volcanics) and three carbonate veins are listed in Table 4 and plotted in figure (8a-c). Radiogenic Sr data have been corrected for 600 Ma (Table 4). As this is the best estimate of when pervasive carbonation occurred in the study area.

**Table 4** Geochemical and isotopic data from north and south localities, Meatiq study area

| | Concentrations (ppm)[a] | | | | | $\delta^{18}O$ | $\delta^{13}C$ |
|---|---|---|---|---|---|---|---|
| Sample | Rb | Sr | Rb/Sr | $87Sr/^{86}Sr$ | $(^{87}Sr/^{86}Sr)_{600}$[b] | (SMOW) | (PDB) |
| Atg-serpentinites | | | | | | | |
| Me05 | 0.03 | 0.23 | 0.12 | 0.70697 ± 17 | 0.70 | 11.00 | -5.40 |
| Me06 | 0.03 | 0.42 | 0.06 | | | 10.60 | -5.90 |
| Me07 | 0.02 | 0.31 | 0.07 | | | 11.00 | -5.60 |
| Me08 | 0.03 | 0.40 | 0.08 | 0.70779 ± 15 | 0.71 | 10.30 | -5.60 |
| Me09 | 0.01 | 0.45 | 0.02 | | | 11.50 | -5.30 |
| Lz-serpentinites | | | | | | | |
| Me21 | 0.11 | 5.82 | 0.02 | 0.70669 ± 16 | 0.71 | 15.10 | -4.20 |
| Me22 | 0.09 | 18.49 | 0.01 | 0.70461 ± 13 | 0.70 | 14.00 | -4.10 |
| Me23 | 0.12 | 69.75 | 0.00 | 0.70432 ± 16 | 0.70 | 12.30 | -4.20 |
| Me24 | 0.03 | 56.37 | 0.00 | 0.70422 ± 14 | 0.70 | 13.70 | -4.20 |
| Carbonate veins | | | | | | | |
| Me02 | 0.04 | 1135.00 | 0.00 | 0.70344 ± 12 | 0.70 | 6.40 | -8.10 |
| Me12 | 0.01 | 502.50 | 0.00 | 0.70281 ± 13 | 0.70 | 9.40 | -6.80 |
| Me28 | 0.00 | 2365.00 | 0.00 | 0.70293 ± 13 | 0.70 | 10.50 | -6.80 |
| Meta-volcanics | | | | | | | |
| Me18 | 1.03 | 59.79 | 0.02 | 0.70341 ± 16 | 0.70 | 9.40 | -10.00 |
| Me19 | 0.59 | 103.80 | 0.01 | 0.70323 ± 12 | 0.70 | _ | _ |
| Me20 | 1.25 | 70.84 | 0.02 | 0.70336 ± 15 | 0.70 | 11.10 | -9.30 |

a Blank-corrected concentrations.
b Isotopic composition at 600 Ma.

The isotopic data display relatively wide range of $\delta^{18}O$ values from +6.4‰ to +15.1‰ while $\delta^{13}C$ varies between -10.0‰ to -4.1‰. The nine samples of serpentinite have relatively highest C and O values and show two distinct groups (Table 4, Fig. 8b). Three sample of carbonate veins (Me2, Me12 and Me28) display a relatively wide range of $\delta^{18}O$ from +6.4‰ to +10.5‰ while $\delta^{13}C$ values show much less variation, range from -8.1‰ to -6.8‰. These veins constitute a tight cluster of $^{87}Sr/^{86}Sr$ ratios ranging from 0.7028 to 0.7034. The

carbonate veins contain low concentrations of Rb from 0.001 to 0.04 ppm (mean = 0.015 ppm) while Sr contents are relatively high and vary widely, from 502 to 2365 ppm (mean = 1334 ppm). Rb/Sr ratios are extremely low, invariably less than 0.00001 (Table 4).

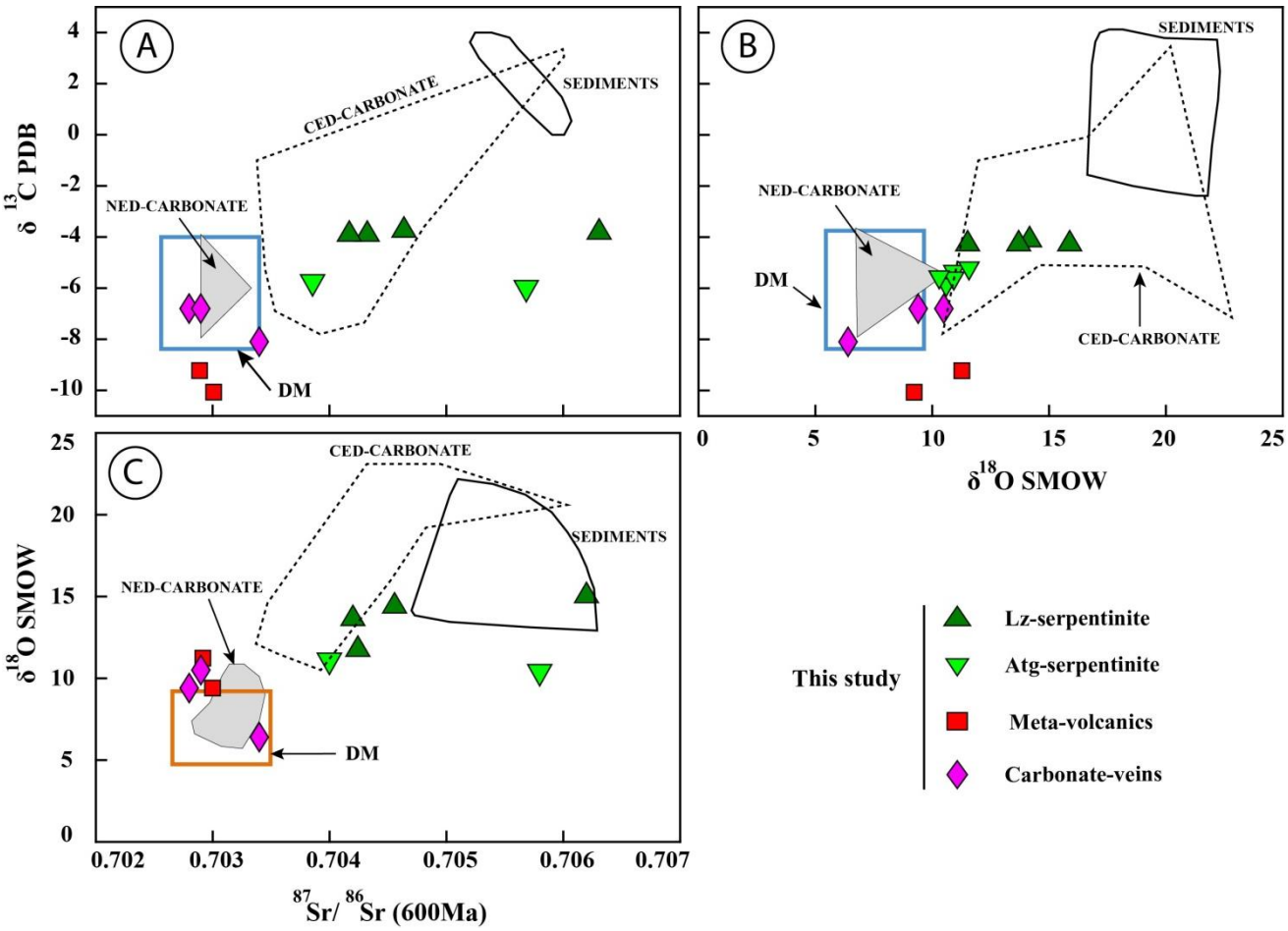


**Fig 8** plots of O, C and Sr isotope data for Meatiq ophiolitic rocks and carbonate veins. Data for (CED) carbonates, sedimentary and NED are shown as dashed-line, solid-line and grey area respectively (data are adopted from Stern and Gwinn, 1990); **(a)** $\delta^{13}C$ vs. $^{87}Sr/^{86}Sr$ at ~600Ma. Field of late Precambrian mantle-derived carbonates (blue boxes) is taken from C-isotopic data of Taylor et al. (1967) and Deines (1989), and Sr-isotopic data for Egyptian basement rocks (brown box) are from Stern and Hedge (1985); **(b)** $\delta^{13}C$ vs. $\delta^{18}O$ from the same samples, with similar fields displayed; **(c)** $\delta^{18}O$ vs. $^{87}Sr/^{86}Sr$ at 600Ma with similar reference fields outlined.

The Lz-serpentinites (Me21 to Me24) range in $\delta^{18}O$ from +12.3‰ to +15.1‰ with fairly uniform $\delta^{13}C$ values range between -4.2‰ to -4.1‰. The Lz-serpentinites $^{87}Sr/^{86}Sr$ ratios span relatively a wide range from 0.7042 to 0.7062. They contain low concentrations of Rb from 0.033 to 0.12 ppm (mean = 0.88 ppm) with Sr concentrations ranging from 5.8 to 70 ppm (mean = 37.6 ppm) and Rb/Sr ratios mostly less than 0.01.

The Atg-serpentinites (Me5 to Me9) constitute another tight cluster, with δ18O = +10.3‰ to +11.5‰ and δ13C = -5.3‰ to -5.9‰. The 87Sr/86Sr ratios of Atg-serpentinites range from for the 0.7039 to 0.7058. This group of serpentinites contain similarly low concentrations of Rb from 0.009 to 0.031 ppm (mean = 0.023 ppm) while Sr contents are relatively low and vary from 0.23 to 0.45 ppm (mean = 0.36 ppm). Rb/Sr ratios vary from 0.02 to 0.12.

The meta-volcanics define another distinct group with the lowest δ13C range from - 10.0‰ to -9.3‰ and δ18O from +9.4‰ to +11.1‰. Meta-volcanics have a restricted 87Sr/86Sr ratio in Meatiq area which varies from 0.7029 to 0.7031. This group of rocks contain relatively higher Rb concentrations ranging from 0.5 to 1.2 ppm (mean = 0.9 ppm) and Sr varies from 60 to 104 ppm (mean = 78 ppm).

### 5.4. Microthermometry

Three coexisting fluid inclusion types (type1 to 3) have been identified based on their different composition and phases (liquid-vapor-solid) present at room temperature and phase transitions observed during heating and cooling (Fig. 9, Table 5). The investigated samples have been deformed and the quartz and carbonate veins are partly recrystallised with the development of subgrain boundaries (Fig. 10a, b). Many fluid inclusions occur mostly along pseudosecondary and secondary trails (crosscutting grain boundaries), cluster in the recrystallised grains or define subgrain boundaries (Fig. 10c, d). Numerous inclusions are elongated in the direction of the trails and necking down is commonly seen (Fig. 10e). However, all analyses were made on fluid inclusions without clear signs of post-entrapment modifications.

**Table 5** Microthermometric data of fluid inclusions from the Meatiq study area

| Sample | Fluid inclusion | TmCO2 | Tm ice | Tm,cla | ThCO2 | Salinity | Th total |
|---|---|---|---|---|---|---|---|
| Host vein | | (°C) | (°C) | (°C) | (°C) | (mass% NaCl) | (°C) |
| | **Aqueous type** | | | | | | |
| Dol-Me2 | Mg-Na-Cl-H20 | | -2.6 to -0 | | | 0.0 to 4.3 | 239 to 265 |
| Dol-Me2 | Ca-Na-Cl-H2O | | -16.4 to -4.0 | | | 6.4 to 16.9 | 225 to 383 |
| Dol-Me2 | Mg-Na-Cl-H20 secondary | | -1.3 to 0.0 | | | 0.0 to 2.2 | 161 to 255 |
| Qtz-Me3 | Mg-Na-Cl-H20 | | -3.5 to -0.1 | | | 0.2 to 5.7 | 225 to 266 |
| Qtz-Me3 | Mg-Na-Cl-H20 secondary | | -3.5 to -0.1 | | | 0.2 to 5.7 | 177 to 234 |
| Mgs-Me9 | Mg-Na-Cl-H20 | | -2.4 to -0.5 | | | 0.9 to 5.0 | 210 to 335 |
| Dol-Me12 | Mg-Na-Cl-H20 | | -2.9 to -0.8 | | | 1.4 to 4.8 | 253 to 302 |
| Qtz-Me16 | Mg-Na-Cl-H20 | | -4.0 to -1.8 | | | 3.0 to 6.4 | 224 to 259 |
| Qtz-Me16 | Mg-Na-Cl-H20 secondary | | -4.8 to -1.8 | | | 3.0 to 7.6 | 113 to 237 |
| Dol-Me28 | Mg-Na-Cl-H20 | | -3.3 to -1.0 | | | 1.7 to 5.5 | 262 to 315 |
| | **Aqueous-carbonic type** | | | | | | |
| Qtz-Me3 | CO2±(CH4, N2)-H2O-NaCl | -57.7 to -56.6 | | 7.7 to 9.5 | 26.8 to 28.0 | 1.0 to 4.7 | 305 to 331<br>324 to 365 (g) |
| Dol-Me12 | CO2±(CH4, N2)-H2O-NaCl | nd | | 7.5 to 9.8 | | 0.2 to 4.9 | 252 to 276 |
| Qtz-Me16 | CO2±(CH4, N2)-H2O-NaCl | -58.2 to -56.6 | | 6.6 to 9.9 | 20.3 to 28.6 | 0.7 to 3.1 | 265 to 363<br>332 to 398 (Tc) |
| Dol-Me28 | CO2±(CH4, N2)-H2O-NaCl | -57.3 to -56.6 | | 6.6 to 10 | 26.8 to 29.2 | 0.0 to 6.8 | 242 to 331 |
| | **Carbonic type** | | | | | | |
| Qtz-Me3 | CO2±(CH4, N2) | -57.3 to -56.6 | | | 26.8 to 29.5 | | |
| Qtz-Me16 | CO2±(CH4, N2) | -58.2 to -56.6 | | | 6.6 to 27.2 | | |

Tm,CO2 = melting of the CO2; Tm,cla = melting of CO2 hydrate, Th,CO2 = homogenization of the CO2 phases to liquid (l); Tm,ice = final melting of ice; Salinity = wt.% NaCl calculated from Tm,ice or Tm,cla; Th,total = total homogenization to the liquid phase or gas phase (g); Tc = critical homogenization temperature; Dol = dolomite; Qtz = quartz; Mgs = magnesite; nd = not detected.

TypeI: Type I are aqueous two-phase inclusions ($LH_2O$+ $VH_2O$) occurring at random as single inclusions, in clusters or along pseudosecondary and mostly secondary trails which crosscut grain boundaries and are characterized by variable degrees of fill (~5-60 vol% gas). Many of these inclusions are elongated; with rectangular to negative crystal shapes and ranging in size from 4 to 40 µm. A few inclusions are single phased and consist of solely vapor $H_2O$. In a late vein of dolomite (Me2) the aqueous inclusions are the only type of inclusions observed.

TypeII: Type II inclusions are three phase ($LH_2O+LCO_2+VCO_2$) aqueous-carbonic with low degree of fill (~30 to 70 vol% gas). This type of inclusions is less common than type-1 and occurs randomly distributed, in clusters or along pseudosecondary trails. The inclusions vary in shape from negative crystal shaped to spindle or irregular shapes. The inclusions range in size from 5 to 15 µm.

Type III: Type III inclusions are carbonic, containing liquid $CO_2$ + vapor $CO_2$ at room temperature (Fig. 9). They are generally small (<10 µm), rounded isometric or negative crystal in shape and occur in cluster or along pseudosecondary trails. Type III inclusions are only present in quartz veins (Me3 and Me16) only.

**Fluid inclusions hosted by talc-rich (east part of locality A):**

Two representative samples (Me2, Me3) were collected for microthermometry. Sample Me2 is from a dolomite vein whereas sample Me3 is collected from lenses of quartz within the altered talc-rich rock. Both samples show deformation and subgrain boundaries due to recrystallisation are well developed.

All inclusions in sample Me2 are aqueous type 1 inclusions. Based on different salinity and salt composition, two aqueous inclusion assemblages have been identified in sample Me2 (low and moderate salinity in Table 5). The main part of fluid inclusions occurs in primary clusters and in pseudosecondary trails, but the low salinity type appeared in secondary trails as well. The temperature of first ice-melting (Tfmice) range from -28° to -35°C for the low salinity and from -49° to -52°C for the moderate salinity inclusions. These temperatures which may be interpreted to reflect the most likely principal salts in solution (even though lesser amounts of other salts can be present) are similar to the eutectic temperature of the $H_2O$-salt systems dominated by NaCl-$MgCl_2$ and $CaCl_2$-NaCl respectively (Shepherd et al. 1985).

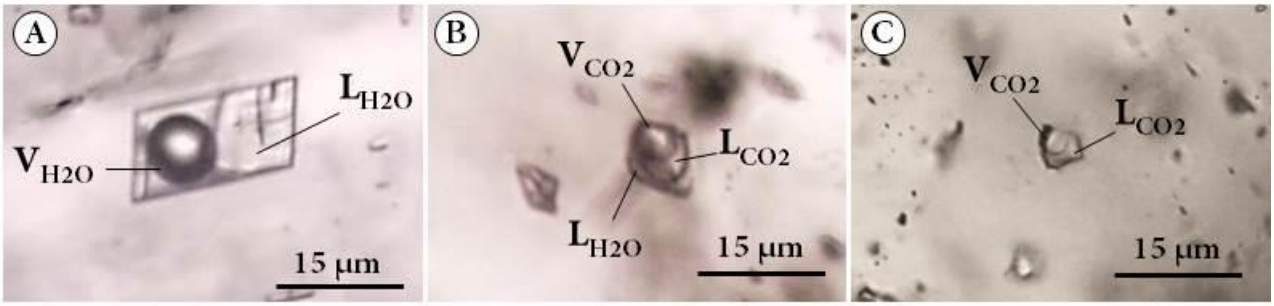


**Fig. 9** Photomicrographs of typical fluid inclusions in quartz/carbonate veins: **(a)** type 1 aqueous inclusion, ($LH_2O+VH_2O$); **(b)** Type 2, aqueous-carbonic, ($LH_2O+LCO_2+VCO_2$); **(c)** Type 3 carbonic inclusion ($LCO_2+VCO_2$).

The final ice-melting temperatures (Tmice) range from 0° to -2.6°C (secondary between 0° and -1.3°C) which gives a salinity of 0 to 4.3 mass % NaCl eq. (low salinity inclusions) and from -4.0° to -16.4°C which corresponds to a salinity of 6.4 to 16.9 mass % NaCl eq. (moderate salinity inclusions). The salinities (Fig. 11) are calculated using data in Bodnar (2003). Homogenisation temperature of all inclusions occurred between 161° and 383°C to liquid. The inclusions in clusters and in pseudosecondary trails homogenised in the range from 239° to 365°C (low saline inclusions) and from 225° to 383°C (moderately saline inclusions) (Fig. 11). The secondary low salinity inclusions homogenised in the range 161° to 255°C (Table 5). More than 50% of inclusions in Me3 are carbonic type III, with 35 percent of aqueous-carbonic type II and 15 percent belonging to the aqueous type I inclusions.

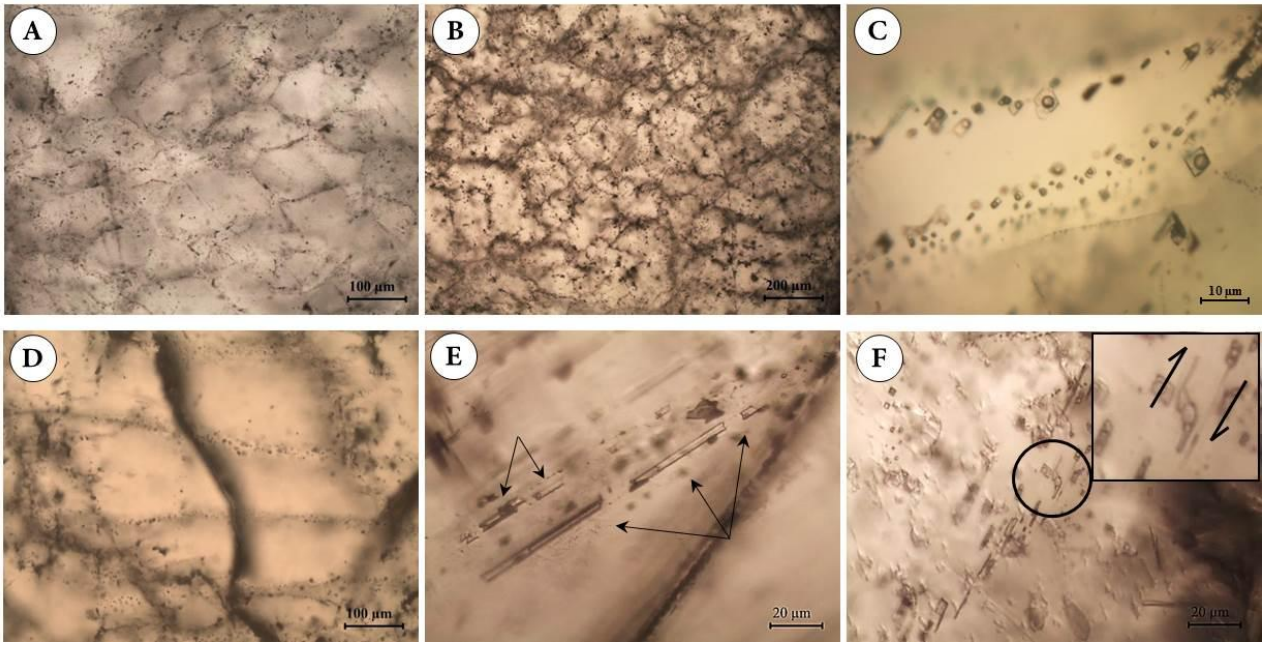


**Fig. 10** Deformation textures in quartz/carbonate veins of study area. **(a)** cryptocrystalline magnesite with fluid inclusion in grain boundaries; **(b)** recrystallisation in quartz veins showing grain boundary bulging; **(c)** pseudosecondary trails of inclusions in dolomite veins; **(d)** trails of secondary inclusion crossing grain boundaries; **(e)** elongation of inclusions in the direction of the trails and necking down; **(f)** fluid inclusion with shear sense in magnesite (Me9).

The inclusions occur as single inclusions, in clusters, in pseudosecondary or secondary trails. First observed melting of the aqueous type I inclusions (Tfmice) range from -28° to -35°C which suggests a predominant NaCl-$MgCl_2$ composition. Final ice-melting temperatures (Tmice) range from -3.5° to -0.1°C corresponding to a salinity of 0.2 to 5.7 mass% NaCl eq. (Bodnar 2003). There was no difference depending on their occurrences. Total homogenisation for the main part of inclusions occurred at temperature ranging from 225° to 266°C (to liquid, Fig. 11) except for the secondary inclusions which homogenised between 177° and 234°C (to liquid). Type II and III inclusions yield melting temperature for solid $CO_2$ ($TmCO_2$) from -57.7° to -56.6°C, followed by homogenisation of $CO_2$ to liquid, between +26.8° to +29.5°C. The difference in melting temperature compared to the pure $CO_2$ triple point (-56.6°C), indicate the presence of additional volatile species like $CH_4$ and/or $N_2$. Based on the data in van den Kerkhof and Thiéry (2001), the corresponding molar volumes of the $CO_2$ inclusions range from about 65 to 90 $cm^3$/mole (Fig. 12). Melting of $CO_2$ clathrate (Tmclath) occurred at temperatures between +7.7 to +9.5°C which indicates the salinity range of 1.0 to 4.7 mass% NaCl eq. (Fig. 11). Few inclusions showed melting temperatures higher than +10°C which can be attributed to the presence of $CH_4$ (Collins, 1979). Total homogenisation to liquid aqueous phase occurred in a relatively limited range of temperature, between 305° to 331°C with a few inclusions with homogenisation to the $CO_2$ phase at higher temperature between 324 to 365°C (Table 5 and Fig. 11).

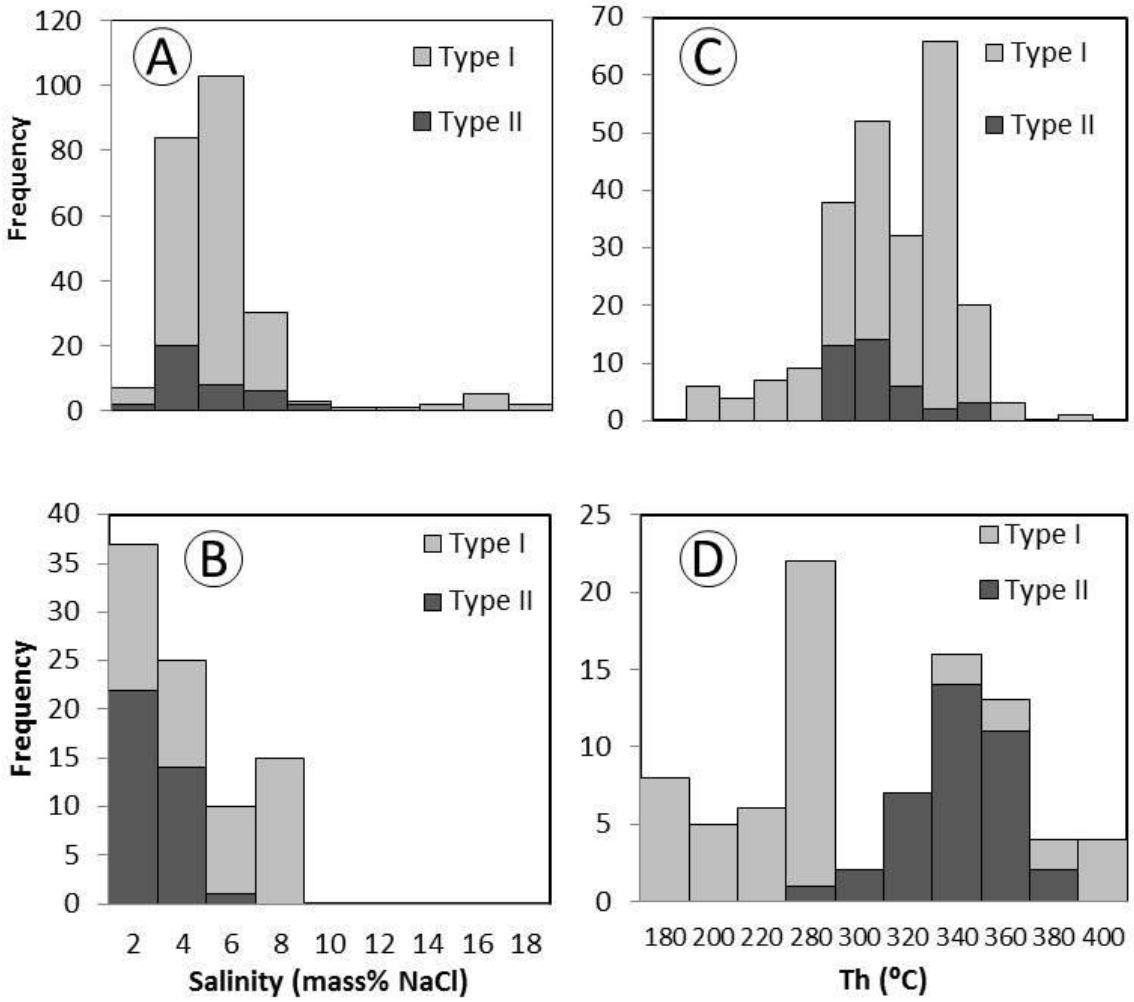


**Fig. 11** Histograms representing the microthermometric data of primary and pseudosecondary inclusion from unmineralised carbonate and quartz veins of Meatiq study area. **(a)** and **(b)** calculated salinity (mass% NaCl) of the two types of inclusion in carbonate and quartz veins, respectively; **(c)** and **(d)** total homogenisation (Th) of the two types inclusion in carbonate and quartz veins, respectively.

**Fluid inclusions hosted by serpentinite and talc-rich (west part of locality A):**

The fluid inclusions were studied in three samples of two different types of carbonate veins hosted by the Atg-serpentinite and talc-rich rocks. Two samples (Me12 and Me28) have been collected from dolomite veins, while the sample Me9 is from a magnesite vein. The aqueous Type I inclusions are predominant (>90 percent) in the magnesite vein (Me9) whereas the aqueous-carbonic Type II are less frequent (<10%). In dolomite veins (Me12 and Me28), abundances of Type II inclusion are more than 60 percent and Type I constitute for the remaining 40% of the total inclusions. The inclusions occur along twin planes as pseudosecondary inclusions in bands. A few inclusions occur in secondary trails. Determining of age relationship between intersecting secondary trails is difficult, but it is deduced that these inclusions formed more or less contemporaneously, either during or shortly after deformational event that were accompanied by carbonate crystallisation. Some fluid inclusions in both types of carbonates show deformation, necking down and shear sense (Fig. 10e, f).

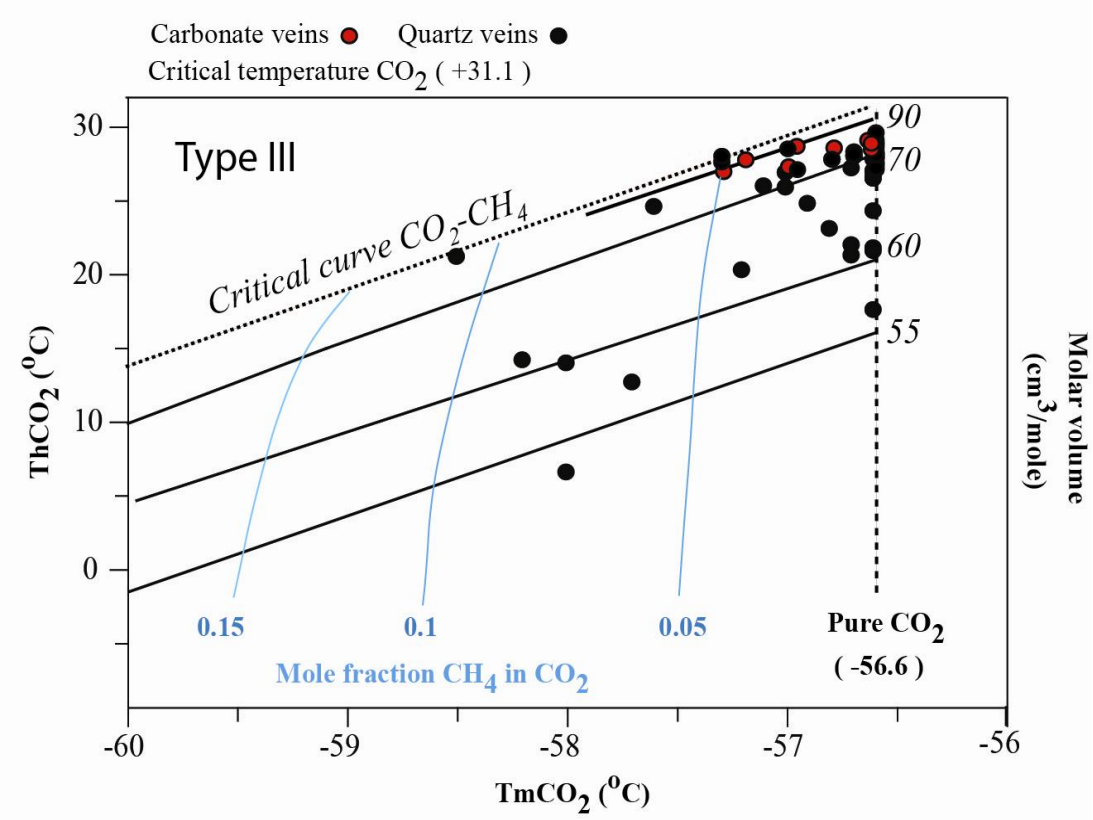


**Fig. 12** Plot of homogenisation temperature (to liquid) versus melting temperature of the CO2-rich phase in fluid inclusions from the Meatiq area. In the diagram the influence of molar volume and mole fraction $CH_4$ (blue) on various combinations of homogenisation and melting temperatures are given (after data from van den Kerkhof and Thiéry, 2001). The melting temperature of pure $CO_2$ is -56.6°C and the critical temperature +31.1°C.

First observed melting of the aqueous Type 1 inclusions (Tfmice) was observed between -30° and -35°C which suggests a salt composition dominated by NaCl and $MgCl_2$ (Shepherd et al. 1985). Final ice-melting temperatures (Tmice) range from -3.3° to -0.5°C corresponding to a salinity of 0.9 to 5.5 mass% NaCl eq. (Bodnar, 2003) (Fig. 11). Total homogenisation to the liquid phase occurs at temperature between 231° to 335°C for the Type I inclusions (Table 5 and Fig. 11). An exception was one inclusion in sample Me 9 that homogenised at 210°C. For the aqueous-carbonic inclusions, Type II, in sample Me 28 melting of the frozen $CO_2$ solid phase occurred between -57.3° to -56.6°C and homogenisation of the $CO_2$-phases to the liquid phase took place at temperatures between +26.8° and +29.2°C. The samples Me 9 and Me 12 contained no separate $CO_2$ phase. $CO_2$ clathrate melting (Tmclath) in samples Me 12 occurred in the range from 7.5 to 9.8 and in sample Me 28 was observed at temperatures between +6.6° and +10.0°C which indicates a salinity of 0.2 to 4.9 mass% NaCl and 0.0 to 6.8 mass% NaCl respectively (Fall et al. 2011) (Fig. 11). Total homogenisation to liquid phase for Type II inclusions in sample Me 12 occurred in the temperature range from 252° to 276°C and in sample Me 28 between 242° and 323°C (Fig. 11). For this type of inclusions, heating above 330 often led to decrepitation.

**Fluid inclusions hosted by talc-rich (locality B):**

Sample Me16 has been collected from a large quartz vein within the altered talc-rich rocks. The quartz vein is milky in color, highly deformed and boudinaged. In sample Me16, carbonic (Type III) inclusions constitute more than 50 percent of inclusions whereas the aqueous-carbonic Type II inclusions account for 40% and the

aqueous Type I inclusions make up 10 percent. The inclusions occur as single inclusions, in clusters, in pseudosecondary or secondary trails. First ice-melting temperatures (Tfmice) for all aqueous Type I inclusions in sample Me16 range from -33° to -24°C, implying the predominance of NaCl and $MgCl_2$ (Shepherd et al. 1985). Final ice-melting temperatures (Tmice) range from -4.8° to -1.8°C, corresponding to a salinity of 3.0 to 7.6 mass% NaCl eq. (Bodnar, 2003) (Fig. 11). The data show a weak trend with somewhat higher salinities for the inclusions in the secondary trails. Total homogenisation temperatures (to the liquid phase) in single inclusions, in clusters and in pseudosecondary trails range from 224° to 259°C and for the secondary inclusions between 113° and 237°C (Table 5 and Fig. 11). Type II and III inclusions display melting temperature for solid $CO_2$ from -58.2° to -56.6°C, followed by homogenisation of $CO_2$ to liquid, between +6.6° to +28.6°C. Based on the data in van den Kerkhof and Thiéry (2001), the corresponding molar volumes of the $CO_2$ inclusions range from about 55 to 90 $cm^3$/mole (Fig. 12). For Type II inclusions, melting of $CO_2$ clathrate (Tmclath) occurred at temperature between +6.6° to +9.9°C which indicates the salinity range of 0.7 to 3.1 mass% NaCl (Fall et al. 2011) (Fig.11). Total homogenisation temperature of the Type II inclusions to liquid range from 265° to 363°C, however some inclusions show critical homogenisation (Tc) at 332 to 398°C. In fact, inclusions with a low degree of fill (~75 vol% gas) decrepitated at temperatures above 340°C, before total homogenisation was reached (Table 5).

### 5.5. Laser Raman spectroscopy

Analysis with Raman spectroscopy shows that the $CO_2$-rich gas phase in the aqueous-carbonic type II and carbonic type III fluid inclusions from the samples Me3, Me16 and Me28 contain $CH_4$ and $N_2$ in addition to $CO_2$. The spectra are illustrated in figure 13, bands at 1282 $cm^{-1}$ and 1385 $cm^{-1}$ are from $CO_2$, at 2912 $cm^{-1}$ from $CH_4$ and at 2326 $cm^{-1}$ from $N_2$. Raman data confirm the compositional variation; mixed $CO_2$-$CH_4$-$N_2$ to pure $CO_2$ compositions (Fig. 13) indicated by microthermometry with depression of $CO_2$ melting points from -56.6° (melting point of pure $CO_2$) to -58.2°C demonstrating a $CO_2$ phase with up to 15 mole % $CH_4$ and/or $N_2$. Raman data reveal semi-quantitative compositions from around 88-90 mole % $CO_2$, <5 mole % $CH_4$ and <10 mole % $N_2$ to a pure $CO_2$ composition. Additional gases like sulfur compounds and higher weight hydrocarbons were not recognized by the Raman instrument.

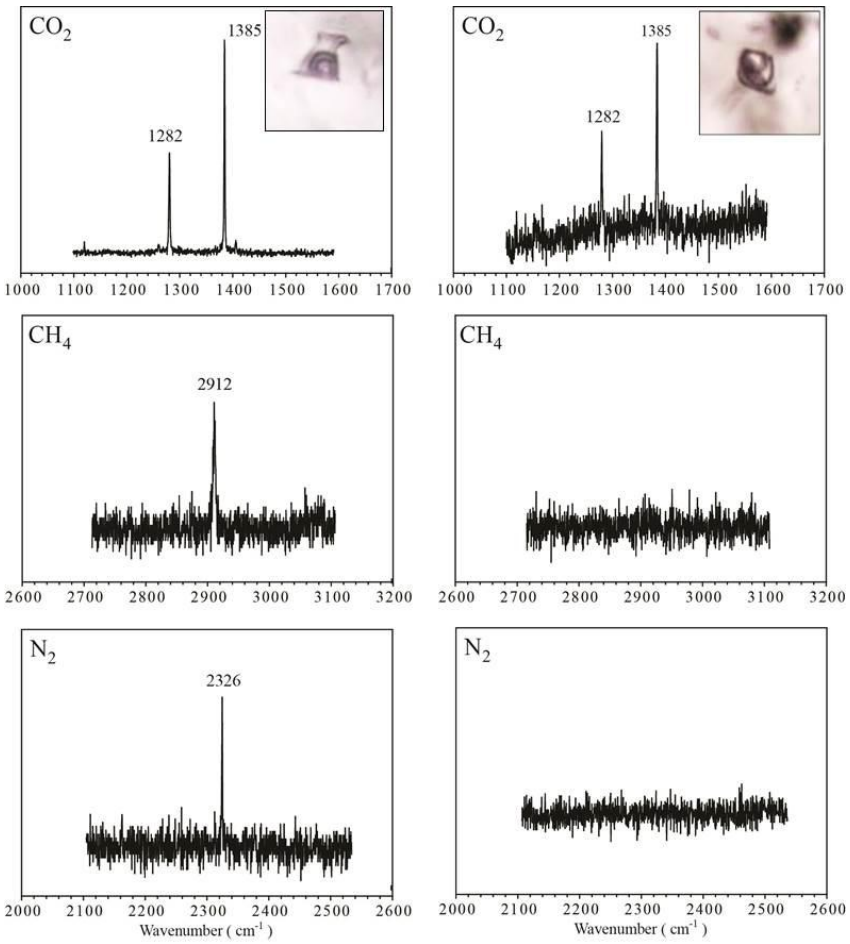


**Fig. 13** Raman spectra of the carbonic phase in fluid inclusions in sample Me3 with $TmCO_2$ at -56.6˚C (right, pure $CO_2$) and in sample Me16 with $TmCO_2$ at about -58.2˚C (left, mixed $CO_2$-$CH_4$-$N_2$ composition).

## 6. Discussion

### 5.1. Tectonic settings of serpentinite protolith:

Most recent studies show that the Egyptian ophiolitic basements are dismembered serpentinized mantle peridotite slices of ANS which formed in a suprasubduction (SSZ) setting (El-Sayad et al. 1999; Stern et al. 2004; El Gaby, 2005; Ahmed et al. 2006; Azer and Stern, 2007). These rocks are interpreted as formed due to seafloor spreading that opened Mozambique Ocean between the West and East Gondwana supercontinent (Stern et al. 2004). The SSZ settings, however are still controversial while some workers suggesting formation at spreading centers in forearc (Shervais et al. 2004; Stern et al. 2004; Azer and Stern, 2007; Hamdy et al. 2013) a back-arc convergent margin (El-Sayed et al. 1999; Abdel Aal et al. 2003; Farahat et al. 2004; El Gaby 2005; El Bahariya, 2008; Ali et al. 2009) and both back-arc and forearc tectonic settings (Abd El-Rahman et al. 2012).

The relationship between Al, Mg and Ca has been used to constrain tectonic settings of peridotites (Coleman, 1977). The $Al_2O_3$-MgO-CaO diagram has been used to constrain the tectonic setting of peridotites and on this diagram our samples plot within the field of metamorphic peridotites associated with ophiolites (Fig. 14a). The very low abundance of alumina (0.44± 0.1 wt%) plots in the field of oceanic trench peridotites as defined by Bonatti and Michael (1989) and on the $Al_2O_3$ versus CaO diagram, they show strong depletion in $Al_2O_3$

and CaO, similar to harzburgites recovered from modern intra-oceanic forearcs (Fig. 14b). In comparison to moderate depleted protolith of abyssal serpentinites (Al/Si weight ratios> 0.03), the forearc serpentinites are highly refractory with low Al/Si <0.03 ratios and having U-shape REE pattern (Hattori and Guillot, 2007; Deschamps et al. 2010, 2011; Kodolányi et al. 2012; Barnes et al. in press). The Al/Si weight ratios for both types of Meatiq serpentinites are <0.013 and REE compositions show slightly LREE enrichments, specifically for Lz-serpentinites (Fig. 7a, b).

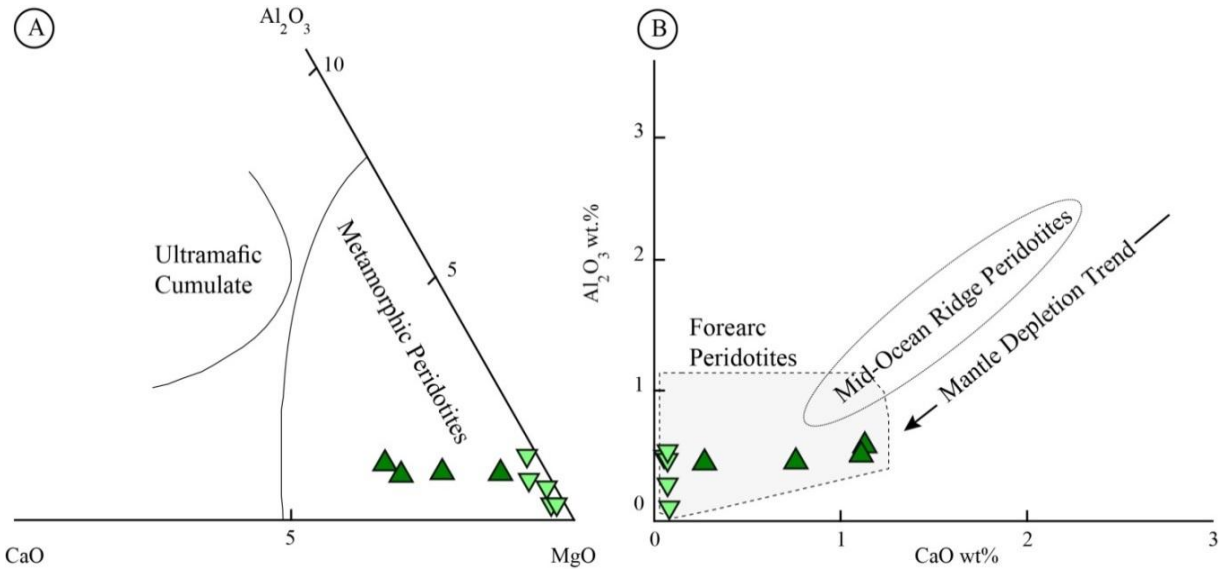


**Fig. 14 (a)** $Al_2O_3$-MgO-CaO diagram for the studied serpentinites (Coleman, 1977); **(b)** $Al_2O_3$ versus CaO diagram, comparing Meatiq peridotites with peridotites from other tectonic settings (after Ishii et al. 1992). The symbols are the same as for Fig. 4.

Cr-spinels have also been used to constrain tectonic setting with those from forearc serpentinites having high Cr# up to 0.80 (Ohara and Ishii 1998; Stern et al. 2004) compared to back-arc serpentinites with Cr# ≤0.55 (Dick and Bullen 1984; Ohara et al. 2002; Ohara 2006). Cr-spinels from the Fawakhir serpentinites in the vicinity of study area (15 km south west of study area) indicate Cr# (~0.66 to 0.80) similar to spinels of forearc peridotites (Hamdy et al. 2013). In summary, our data support a forearc setting.

## 5.2. Alteration/metamorphism of Meatiq ophiolitic rocks:

The ultramafic rocks associated with ANS ophiolites are generally highly altered, but it is unclear whether this alteration occurred before, during, or after emplacement. These rocks are largely converted to serpentinite or to mixtures of serpentine, talc, tremolite, magnesite, chlorite, magnetite, and carbonate (Stern et al. 2004).

### 5.2.1. Serpentinites: Lizardite-antigorite transition

Lizardite and chrysotile are usually present in low-grade serpentinites from the oceanic lithosphere and from low-grade metamorphic ophiolites (Andréani et al. 2007; Evans, 2004, 2010) while the antigorite is mostly dominated serpentine variety in high-grade metamorphic terranes (Auzende et al. 2002, 2006; Debret et al. 2013; Evans and Tromsdorff, 1978; Groppo and Compagnoni, 2007; Guillot et al. 2009; Li et al. 2004; Mellini et al. 1987; Padron-Navarta et al. 2008; Scambelluri et al. 1995; Trommsdorff et al. 1998). Lizardite

serpentinites form on low-temperature environments (50–300°C) (Kodolányi and Pettke, 2011). Recent study Schwartz et al. (in press) shows that, below 300°C, lizardite and locally chrysotile are the dominant species and between 320 and 390°C, lizardite is progressively replaced by antigorite whereas above 390°C, antigorite is the sole stable serpentine mineral.

Both lizardite (Basta and Kader, 1969) and antigorite (Akaad and Noweir, 1972) have been reported as the main constituent of CED serpentinites, but the significance of these variations has not been investigated. In this study the main mineral constituent of serpentinite in south locality is lizardite/chrysotile (Fig. 15a, c) whereas the main mineral constituent of serpentinite in north locality is antigorite (Fig. 15b, d). Based on lizardite-antigorite phase transition, two levels of serpentinite alteration/metamorphism can be distinguished in Meatiq serpentinites with the Atg-serpentinites having been altered/metamorphosed at higher temperatures than the Lz-serpentinites. The proportion of carbonate is considerably greater in the Atg-serpentinites. The Lz-serpentinites contain rare disseminate carbonate (Fig. 15c) whereas the Atg-serpentinites are characterized by intensive carbonate alteration in form of carbonate veins and pervasive patchy carbonate (Fig. 15d). The higher temperature alteration of the Atg-serpentinites is supported by the textural evolution of Cr-spinels, with the Cr-spinel of Atg-serpentinites has been heavily altered while the Cr-spinel in Lz-serpentinites shows no considerable textural changes (Fig. 15e, f). The degree of Cr-spinel alteration indicates greenschist facies conditions based on textures evolution reported in Ahmed et al. (2001), Saleh (2006) and Farahat (2008).

Based on phase relationship between lizardite-antigorite and texture of Cr-spinel, we suggest that the Lz-serpentinites have experienced alteration at 100 to 250 ˚C whereas the Atg-serpentinites have been altered at around 350 to 400 ˚C. The occurrence of high proportions of carbonate within the Atg-serpentinite samples implies that the fluid that precipitated the carbonate may have aided phase transition from lizardite to antigorite. We suggest that the Atg-serpentinites in Meatiq area may have formed through hydrothermal alteration of Lz-serpentinites due to influx of a $CO_2$-rich fluid at temperature >300˚C. Whether this occurred in a sub-arc region or during regional metamorphism is not clear.

**Major element variations during lizardite-antigorite transition**

The intensive carbonate alteration in Atg-serpentinites relative to Lz-serpentinites reflected in slightly higher MgO (38.8±0.3 wt%) and LOI (16.4±2.8) of Atg-serpentinite in comparison with lower MgO (37.8±0.3 wt%) and LOI (13.7±0.3 wt%) of Lz-serpentinite (Fig. 4 and 5). The other majors show no significant variations between two serpentine phases.

**Trace element mobility during transition of lizardite to antigorite**

The relatively restricted concentrations of Cr, Ni and Co show no considerable changes between two serpentine phases, suggesting these elements were immobile during transition of Lz-serpentinite to Atg-serpentinite (Fig. 6). The slight decrease in Cr content from Lz-serpentinite (~2670 ppm) to Atg-serpentinite is attributed to alteration/metamorphism of Cr-spinels (Fig.15e, f). Some of the Cr dissolved from chromite core has entered the chlorite in the vicinity of Cr-spinels forming Cr-chlorite. Similarly, high field strength incompatible elements (e.g. Nb, Zr, Hf) and Y show no changes between lizardite and antigorite phases, indicating immobile characteristics of these elements during alteration/metamorphism (Fig. 6).

Regarding the FME, As and S show different concentrations (Table 3 and Fig. 6) in the two serpentinites rock types. Lz-serpentinites contain higher concentrations of As (33±22 ppm) and S (447±170 ppm) compared to Atg-serpentinites (As = 5 ppm and S = 16±8 ppm). The only sulfide minerals occurring in the Lz-serpentinites are nickel-sulfides (e.g., pentlandite and millerite), which co-exist with relatively unaltered Cr-spinels (Fig. 3c, 15e). No sulfides are observed in the Atg-serpentinites. We suggest that that As and S concentrations are

depleted in the Atg-serpentinites due to breakdown of primary sulfide phases during transition of lizardite to antigorite.

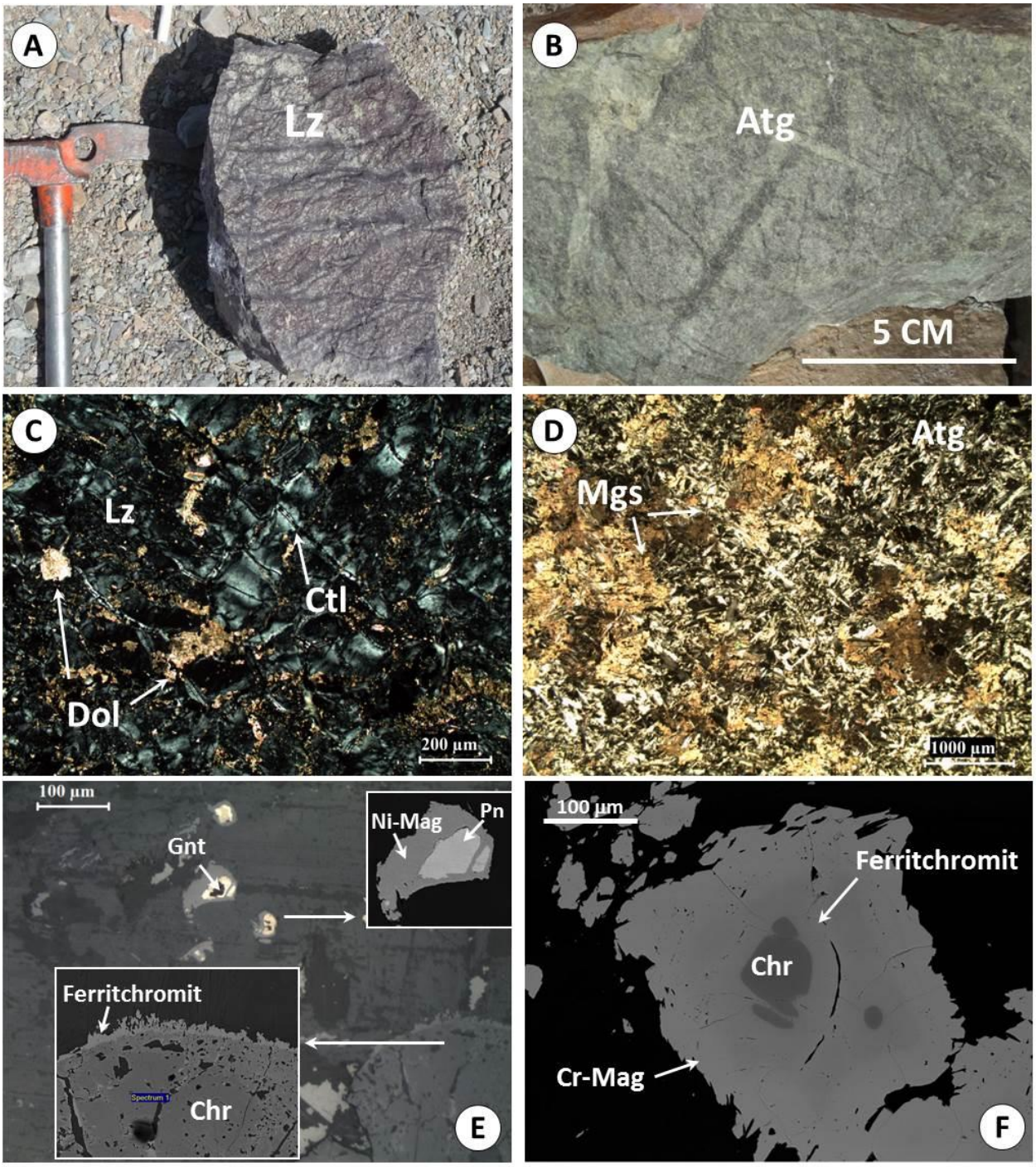


**Fig. 15** Field, photomicrograph and back-scattered electron (BSE) images showing different alteration/metamorphism stages in serpentinites of north and south localities: **(a)** Lz-serpentinite from south locality; **(b)** Atg-serpentinite from north locality; **(c)** serpentinite from south locality containing abundance lizardite and chrysotile with minor disseminated dolomite; **(d)** serpentinite from north locality containing antigorite with pervasive magnesite disseminated in the rock or making network of veinlets; **(e)** and **(f)** showing different Cr-spinels alteration patterns in both serpentinite phases: **(e)** mostly unaltered Cr-spinels with large chromite core and narrow ferritchromite rim with Ni-sulfide (pentlandite) converted to garnierite and Ni-rich magnetite in Lz-serpentinites; **(f)** highly altered Cr-spinels with small chromite core and ferritchromite zone (dark grey) and Cr-magnetite rim (light grey).

Lz-serpentinites contain higher concentrations of gold (averaging 7.25±3.53 ppb) compared with the Atg-serpentinites (averaging 2.71±2.53 ppb) (Table 3, Fig. 6). The gold concentrations in Lz-serpentinites ranging from 3.6 to 11.2 ppb is higher than estimated gold contents in Neoproterozoic serpentinized mantle peridotites which ranging between 3 to 5 ppb (Buisson and Leblanc, 1987). The gold contents of both serpentine phases are also higher than 1 ppb Au proposed for depleted mantle composition (Salters and Stracke, 2004). This may be related to secondary enrichment of mantle peridotite during serpentinization (Buisson and Leblanc, 1987). The close association of gold with higher concentrations of As and S indicates that the gold may reside in nickel-sulfides in Lz-serpentinites (Fig. 6). The occurrence of gold in Ni-sulfides and Ni-arsenides from ophiolitic serpentinites of Pan-African belt has been reported by previous workers (Takla and Surour, 1996, Khalil et al. 2003). A study on serpentinites in the vicinity of Fawakhir gold mine (south west of study area, Fig. 1) showed that the Ni-sulfides carry Au up to 0.64 wt% (Takla and Surour, 1996). The latter workers suggested that serpentinized ultramafic rocks may have been an important source of gold. The decrease of whole rock gold concentrations during transition of lizardite to antigorite most likely represents liberation of gold from Ni-sulfides by the $CO_2$-rich fluid that caused carbonation. This is the first time that gold has been observed to be remobilised during transition of transition of lizardite.

The serpentinites (especially the Lz-serpentinites) are characterized by significant enrichment in As, Sb, Au and Cs compared to primitive mantle (McDonough and Sun, 1995) and depleted mantle values (Salters and Stracke, 2004) (Table 3, Fig. 16). Similar enrichment in FME have been observed in both abyssal and forearc settings serpentinites (Hattori and Guillot, 2003, 2007; Scambelluri et al. 2004a,b; Li and Lee, 2006; Deschamps et al. 2011, 2012; Kodolányi et al. 2012; Barnes et al. in press). The Lz-serpentinites contain higher concentrations of Li, Pb, U, Ba, and Sr relative to Atg-serpentinites suggesting that as with As, S and Au; these elements are depleted during the lizardite-antigorite transition (Fig. 16). The high Sr in Lz-serpentinites may explain by higher CaO (in form of dolomite disseminated) in these rocks compared to Atg-serpentinites with abundances of magnesite. However, not all of the FME are depleted during the lizardite-antigorite transition as the Atg-serpentinites are enriched in Sb and Cs compared to the Lz-serpentinites, and indeed to primitive and depleted mantle values. This may indicate preferential incorporation of Sb and Cs into antigorite (Deschamps et al. 2011) (Fig. 16).

In summary, with the exception of Sb and Cs, we observe that the FME (Li, As, S, Pb, U, Ba, Sr, and Au) have been depleted during transition of lizardite to antigorite. This is inconsistent with other previous works which show no loss of FME during prograde metamorphism from abyssal to subduction environments (Deschamps et al. 2011, 2012). However this might be related to $CO_2$-rich nature of fluid causing the EMF remobilisation during transition of lizardite to antigorite.

Rare Earth Element (REE) abundances in two serpentine phase show slightly decreasing trend from Lz-serpentinite to Atg-serpentinite (Fig. 7a, b). The Lz-serpentinites have higher concentrations of absolute REE (~3.65 ppm) than Atg-serpentinites (~0.54 ppm). It is generally accepted that the mobility of REE is limited during hydrothermal alteration of mafic rock (Humphris and Thompson, 1978; Gillis et al. 1992).

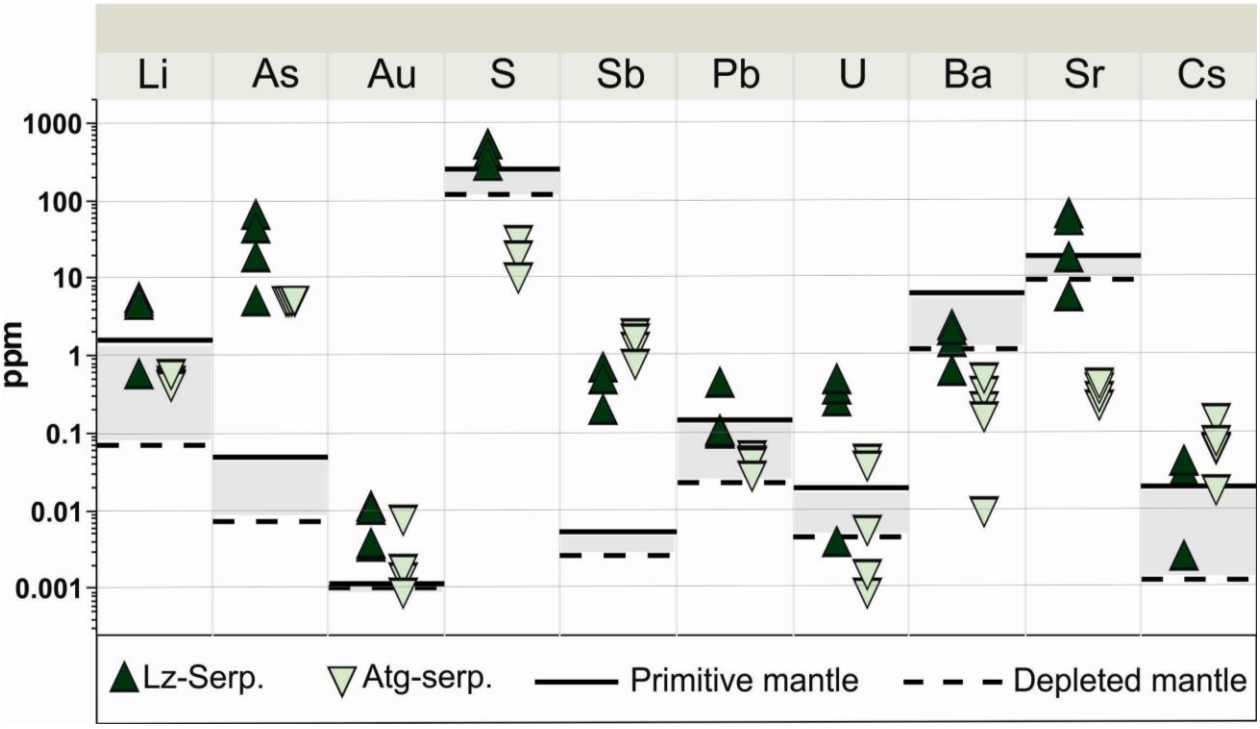


**Fig.16** Plots of concentration of fluid-mobile elements (Li, As, Au, S, Sb, Pb, U, Ba, Sr and Cs) in two serpentine phases from Meatiq study area. Values of primitive mantle after McDonough and Sun (1995) and depleted mantle after Salters and Stracke (2004) are also reported (thick and dashed black lines). Grey boxes represent the ranges between primitive and depleted mantle.

### 5.2.2. Talc-rich rocks:

**Progressive alteration/metamorphism and deformation**

The talc-rich rocks are spatially associated with serpentinized peridotite and dominated within the fault and shear zones (Fig.17a). These rocks show varying degrees of metasomatic alteration to talc, amphibole (tremolite, anthophyllite) and chlorite assemblages. The Cr-spinels are highly brecciated and extensively converted to Cr-magnetite and Cr-rich chlorite (Fig. 3h, 17b, c). Microscopic observations show the talc, amphibole and Cr-spinel show large variation on degree of deformation (Fig. 3h, 17b). The strongly foliated talc-rich rocks (Me15 and Me17) are the most distinctive fault rocks. They show mylonitic texture characterized by strong foliation shape preferred orientations parallel to the orientation of shear zones (Fig. 17d). With progressive deformation, the lens-shaped domains become increasingly elongate and talc-rich rims form a well-developed schistosity (Fig. 17a). Sample Me14 lacks penetrative high-strain deformation fabric. This sample is dominated by static crystallisation of tremolite and anthophyllite, which variably replace fine-grained talc minerals (Fig. 17e). The assemblages anthophyllite, tremolite, talc in ultramafic rocks are indicative of at least greenschist facies metamorphism in the presence of carbon dioxide bearing altering fluids (Robinson et al. 1982). Great proportions of carbonates (magnesite and dolomite) are spatially associated with talc-rich rocks in the form of distinct veins showing the presence of $CO_2$-rich fluid (Fig. 2d). The talc and magnesite assemblages imply Mg-enriched ultramafic precursor evolved at the expense of serpentinites (Bucher and Frey, 1994; Simandl and Ogden, 1999) according to the following interactions:

$$Mg_3Si_2O_5(OH)_4(serp) + 2SiO_{2\,aq} = Mg_3Si_4O_{10}(OH)_2(talc) + H_2O$$

$$Mg_3Si_2O_5(OH)_4(serp) + 3CO_2 = Mg_3Si_4O_{10}(OH)_2(talc) + 3MgCO_3(magnesite) + 3H_2O$$

The involvement of $SiO_2$ could be attributed to meta-volcanics and other silicate-rich country rocks in the vicinity. The occurrence of carbonate in the anthophyllite-bearing variety indicating that equilibrium temperatures and $H_2O$ pressures have been lowered by $CO_2$ in the fluid phase (Robinson et al. 1982).

**Major element variations**

The talc-rich are strongly metasomatised serpentinites having higher density, consistently higher values of $SiO_2$ (57.9 ± 1.4 wt%), $Al_2O_3$ (1.15 ± 0.5 wt%), CaO (8.27 ± 3.9 wt%) and $TiO_2$ (0.02 ± 0.1) and lower MgO (23.2 ± 2.4 wt%), total Fe ($Fe_2O_3$ = 6.4 ± 1.3 wt%) and water content than the serpentinite protoliths (Fig. 5). The talc-rich rocks contain an average of 2.9 wt% LOI compared to 15.2 wt% in the serpentinite and indicate that serpentinite have undergone dehydration to form talc-rich rocks (Fig. 4).

**Trace element variations**

The petrographic relationship of talc-rich rock with serpentinite is also supported by high concentrations of trace element such as Cr, Ni and Co. as Cr-spinel) also support the serpentinite indicative of precursory peridotites. However lower Cr, Ni and Co content compared to serpentinites show intensive metasomatism in fault and shear zones (Fig. 6). Incompatible elements (HFSE; e.g., Zr, Hf, Nb, Ta and Y) show no significant depletion in talc-rich rocks compared to serpentinite protoliths and are inferred to be immobile during alteration/metasomatism. Similar to Atg-serpentinite, the talc-rich rocks show depletion in As (except Me1 = 66 ppm As) and S if compared to Lz-serpentinite. The average gold concentration is less that 1 ppb (0.74 ppb) in these rocks which is clearly lower that both serpentinite phases. Chondrite-normalised REE pattern show depletion in talc-rich rocks compared to Lz-serpentinite but similar LREE patterns relative to the Atg-serpentine (Fig. 7c). Compared to non-metasomatic protoliths, the talc-rich rocks show a slight general enrichment in HREE relative to both serpentine phases (Fig. 7c). In summary, we observe that some of FME (As, S and Au) in talc-rich rocks show depletion if compared to lizardite and antigorite serpentinites.

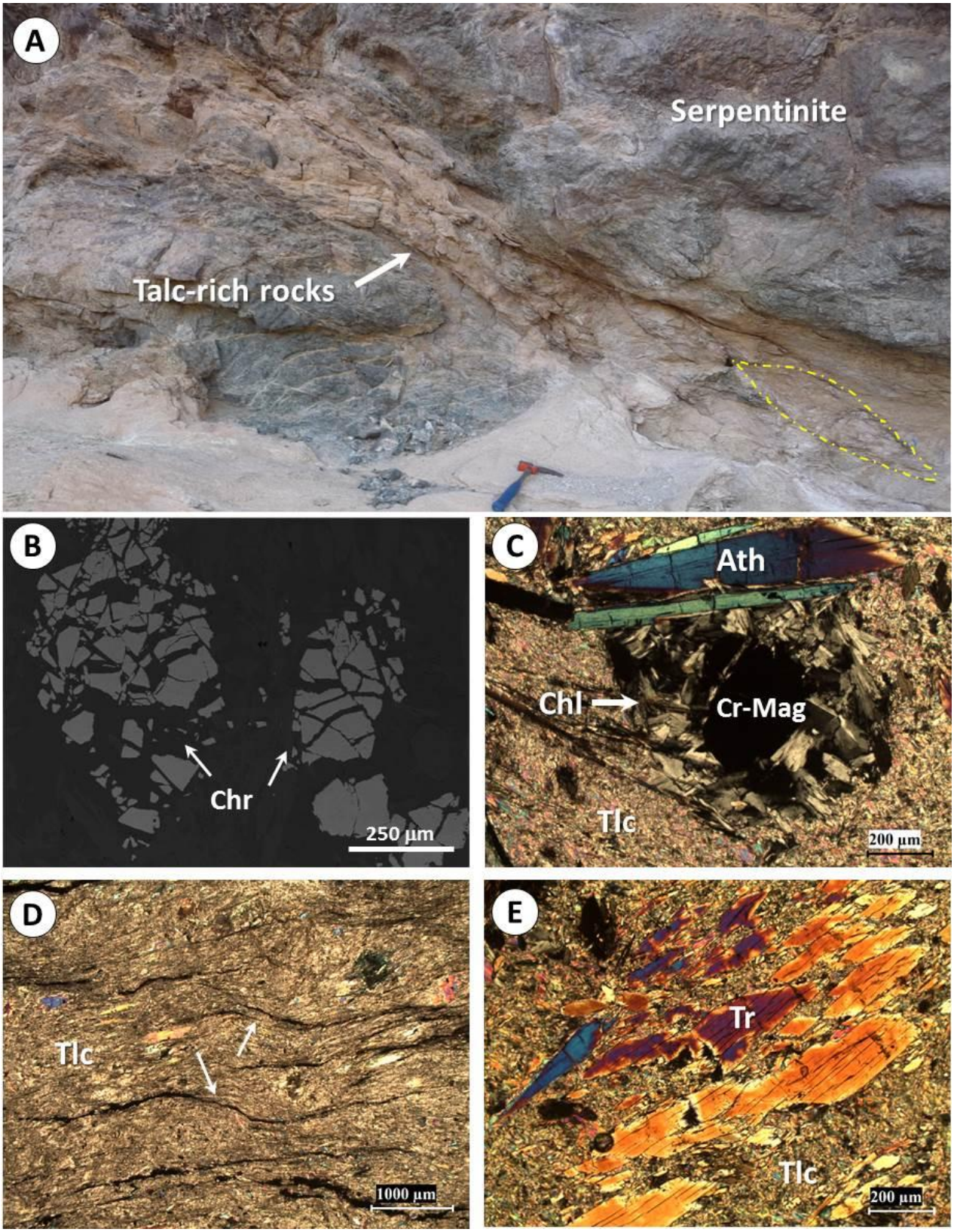


**Fig. 17** Different deformation and mineralisation of investigated talc-rich rocks: **(a)** progressive deformation evidenced by elongated lens-shape structures in shear zone; **(b)** highly brecciated Cr-spinel; **(c)** conversion of Cr-spinel to Cr-magnetite and Cr-rich chlorite rim with anthophyllite (Ath); **(d)** heterogeneous mylonitic texture in highly foliated talc-rich rocks; **(e)** static crystallisation of tremolite (Tr) and anthophyllite, replacing fine-grained talc minerals.

### 5.2.3. Meta-volcanic rocks:

Microscopic observations and assemblages of tremolite/actinolite, chlorite and recrystallised plagioclase show that the volcanic rocks in the study area have experienced greenschist to lower amphibolite facies. Based on geochemistry data, no considerable major elements distributions observed from least metamorphosed varieties to highly metamorphosed rocks. They show same range of CaO, $Al_2O_3$ and MgO with no considerable variations (Fig. 5). Furthermore, these rocks show no evidence of carbonate alteration similar to serpentine phases and talc-rich rocks, indicating the altering fluid has not interacted with these rocks. This is also supported by sharp tectonic contacts of meta-volcanics with other ophiolitic sequences (serpentinites and talc-rich rocks).

Trace elements like Cr and Ni show lower concentrations of ~121 ppm and ~52 ppm compared to the average of ANS basaltic rocks (e.g. Cr = ~372 ppm, Ni = ~140 ppm) while V (~328 ppm) shows relatively higher concentration in comparison to reported composition of ANS volcanics (V= ~230) (Stern et al. 2004). These elements show no variation in different meta-volcanics (Fig. 6). Petrographic studies reveal that some of meta-volcanic samples with higher Zr, Hf, Ti, Y, and REE concentrations correspond to samples with abundances of hydrothermal anhedral zircon, rutile and titanite crystals (e.g. Me10 and Me27) (Fig. 3l). The zircon and titanite have been known as a host of REE and HFSE in other ophiolitic sequences (Boschi et al. 2006). Elements such as Sb, Cs, S and As show no considerable concentrations in meta-volcanics. Meta-volcanics contain very low concentrations of Au (1.23 ± 1 ppb) except sample Me4 with anomalous Au concentrations (20.78 ppb, Table 3, Fig. 6). Gold shows no clear correlation with S and As in these rocks.

### 5.2.4. Chloritite:

The chloritite sample (Me26) is mostly inferred to be the metasomatic interaction at the contact zone of meta-volcanic rocks with ophiolitic rocks. Similar rocks were described as “black wall” (Phillips and Hess, 1936, Fowler et al. 1981). The origin of these rocks in Eastern Desert is controversial and diverse; some workers considered them as a paraschists, belonging to geosynclinals metasediments (El-Ramly and Akaad, 1960; Akaad and Noweir, 1980), while others believed that part of Egyptian chloritites are related to ultramafic rocks (Basta and Kader, 1969; Abdel Kader, 1974; Takla and Noweir, 1980; Takla et al. 1991 and 1992). The lack of preserved preliminary minerals and texture make it difficult to unravel the effects of possible interaction of mixed lithologies. The metasomatic interaction at contact zone of two different lithologies is evidenced by relatively high MgO and low $SiO_2$ and CaO similar to serpentinites while the $TiO_2$ and $Fe_2O_3$, $Al_2O_3$ are at the range of meta-volcanics (Fig. 5). Consistently, Cr and Co contents (and to lesser Ni) of chloritite sample are close to serpentinites and distinctly higher than meta-volcanics whereas Sb, Cs, S, As, HFSE, Y and gold concentrations are in the range of meta-volcanics and talc-rich rocks which representing the interaction of mix lithologies (Fig. 6). The lower LREE concentrations are presumably related to monomineralic (chlorite) characteristic of this rock type.

## 5.3. Source of vein and disseminated carbonate

The $\delta^{13}C$ (mean = -7.2‰) and $\delta^{18}O$ (mean = +8.7‰) values of carbonate veins (Me2, Me12 and Me28) are within the range of mantle-derived carbonatite fluids (Taylor et al. 1967, Demény et al. 1998) (Fig. 8a, b). The $\delta^{18}O$ values of these veins (ranging from +6.4 to 10.5 ‰) shows an increase from depleted-mantle value (+5.5‰ ±0.2‰, Elier, 2001) to heavier values, possibly due to partial re-equilibration with meteoric water. The restricted range of initial $^{87}Sr/^{86}Sr$ in carbonate veins (mean = 0.7030±0.0003) are indistinguishable from

the initial ratio for mantle-derived volcanics from Egyptian basement and Neoproterozoic igneous rocks of the Arabian-Nubian Shield (Engel et al. 1980; Fitches et al. 1983; Stern and Hedge, 1985; Stern and Gwinn, 1990) (Fig. 18). The Sr, O and C values of carbonate veins fall within or close to mantle-derived carbonates veins of NED (Fig. 8b, 18).

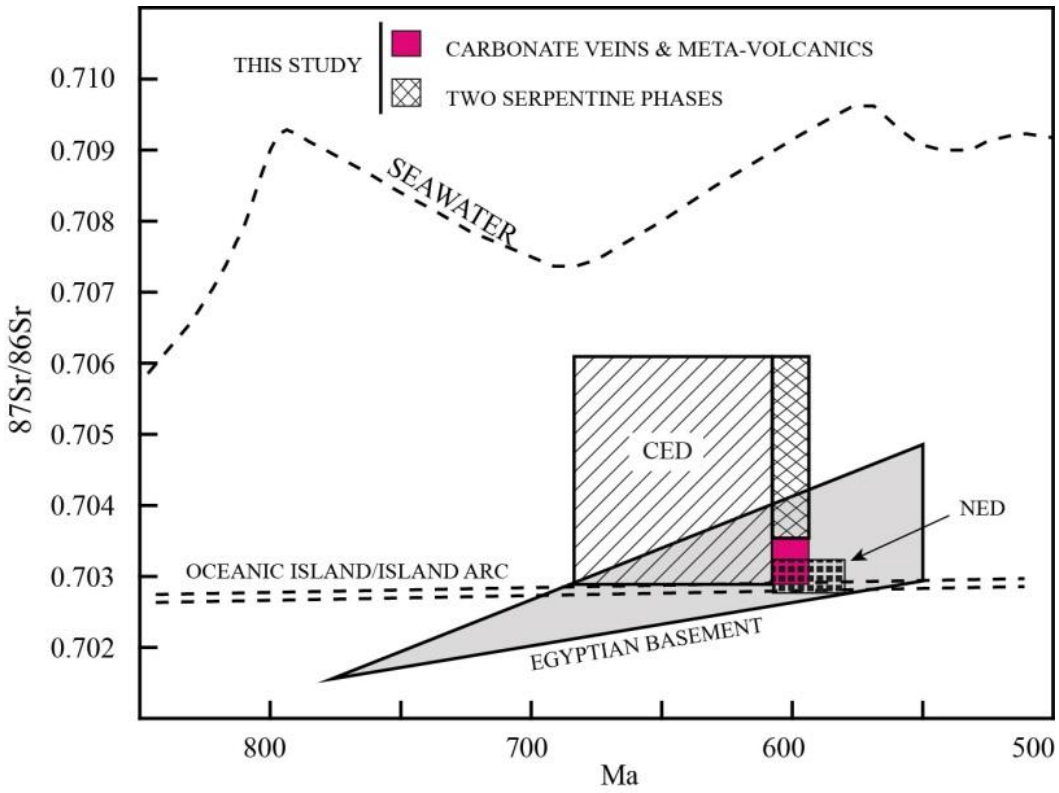


**Fig. 18** Sr composition of carbonate veins and altered serpentinites in the Meatiq are compared to values from late Precambrian intrusive carbonates from northeast of ANS. The ages of emplacement for the intrusive carbonates are estimated from the age of the surrounding basement units (after Cavanagh, 1979; Stern and Hedge, 1985; Reischmann, 1986; Kröner et al. 1987; Stern and Gwinn, 1990). Field of initial $^{87}Sr/^{86}Sr$ for the Egyptian basement is shown after Stern and Hedge (1985); this field represents an upper limit for the isotopic composition of Sr in the depleted mantle beneath northeast Africa at that time. Fields of initial $^{87}Sr/^{86}Sr$ for the CED and NED is shown after Stern and Gwinn (1990). Isotopic composition of late Precambrian seawater is also shown, after Veizer et al. (1983). Note that the field of Meatiq carbonates veins composition and meta-volcanics is close to the Egyptian basement and show the same range of NED while the field of Lz-serpentinites and Atg-serpentinites composition indicates broad range of radiogenic Sr similar to CED.

Dissimilated alteration from the Lz- and Atg-serpentinites have relatively homogenous $\delta^{13}C$ (mean = -4.95‰) very close to the fresh mantle peridotite value ($\delta^{13}C$ ~-5‰; Dasgupta and Hirschamp, 2010) and other mantle-derived rocks (Des Marais and Moore 1984, Exley et al. 1986, Ohmoto, 1986, Dienes, 2002). The bulk rock $\delta^{18}O$ values of serpentinites lie higher than the known range of compositions of oceanic serpentinites (Wenner and Taylor, 1973; Sheppard, 1980; Sakai et al. 1990; Agrinier et al. 1995; Früh-Green et al. 1996; Mével, 2003; Früh-Green et al. 2004) and MORB/mantle values (~+5.7‰, Muehlenbachs, 1987) (Fig. 8b). This indicates that the mantle peridotites have interacted with an external fluid. Submarine weathering and low temperature hydrothermal alteration of ultramafic rocks can induce a general enrichment in $\delta^{18}O$ of bulk rock, whereas high temperature interactions deplete the rock in $\delta^{18}O$ (Alt et al. 1986; Muehlenbachs, 1987; Früh-Green et al. 1996). The Lz-serpentinites show consistently higher $\delta^{18}O$ in comparison to Atg-serpentinites (the

highest $\delta^{18}O$ values in this study, ranging from 12.1 to 15.1‰), suggesting they interacted with low temperature meteoric water. A possible interpretation is that the relatively heavier $\delta^{13}C$ values (-4.2‰) of Lz-serpentinites over Atg-serpentinites ($\delta^{13}C$ = -5.5‰) might reflect interactions with fluid having relative low C/O ratio which led to shift in $\delta^{18}O$ with little change in $\delta^{13}C$ (-1.3‰ higher). The isotopic data of different samples shows a very clear mantle signature with later modification.

### 5.4. Condition of altering fluid:

Fluid inclusion analysis (Table 5) suggests that the carbonate veins were formed after reactions involving aqueous and carbonic fluids. The characteristics of the inclusions suggest a heterogeneous system with coexisting, immiscible fluid phases at the time of carbonate deposition (possibly shear zone). Entrapped inclusions of these fluid phases in the carbonate veins show a large scatter in phase ratios from pure aqueous to pure carbonic end-member types of inclusions and between them inclusions that have trapped various volume proportions of the two phases. The carbonic phase (in Me16) has a $CO_2$-rich composition with small amounts (0 to 10 mole %) of dissolved $CH_4$ and $N_2$, probably present as a result of serpentine mineral alteration reactions or variations in oxygen fugacity. The aqueous phase in both carbonate and quartz veins has an Mg-Na-Cl dominated composition with a low salinity below about 7 eq. mass% Mg-Na-Cl (Fig. 11a, b). Some aqueous inclusions in sample Me2 have higher salinities (up to 17 eq. mass% NaCl) and a more Ca-Na-Cl dominated composition. These may represent an occasional local input of a more saline fluid modified during fluid/wall rock interactions with more Ca-rich minerals.

Total homogenisation temperatures of the samples show a large scatter with values from 113° to 398°C (Table 5), but many of the studied samples (Me 2, Me 3, Me 9 and Me 16) contain secondary aqueous fluid inclusions in healed microfractures. These represent the last stage of fluid activity after carbonate vein formation and give evidence for a long-lived cooling and fluid circulation in fault and shear zones (homogenisation temperatures from 113° to 255°C, Table 5). For the interpretation of the carbonate vein emplacement conditions the secondary inclusions are therefore excluded leaving a more limited range of total homogenisation temperatures from 224° to 398°C (Table 5, Fig 11c, d). Total homogenisation temperature for fluid inclusions trapped under conditions of immiscibility is equal to the original formation temperature (Diamond 2003; Bodnar 2003).

The trapping temperature and pressure conditions can only be estimated from compositions of the two end-members, as intermediate composition fluid inclusions could give homogenisation temperatures above their trapping conditions (Diamond 2003). Trapping conditions for immiscible fluids can be determined by using the technique of intersecting isochores (Roedder, 1984) and at the intersecting point in the PT-diagram the two end-members have temperature and pressure that are identical. The isochore to be used for the aqueous end-members (in the present study inclusions with the lowest homogenisation temperature) in the samples is based on the data in Bodnar (2003) for aqueous fluid inclusions with homogenisation temperature of about 225°C and a salinity of 0-7 eq mass% NaCl. The isochores for the carbonic end-member (after data in Van den Kerkhof and Thiéry 2001, Fig 19) are for molar volumes of 55, 65 and 90 $cm^3$/mole.

The intersection of the aqueous and carbonic isochores in the PT diagram gives trapping conditions for carbonate veins of the study area within a temperature interval from 270° to 305°C and at a pressure of 0.7 to 1.1 kbar. The more extended range of molar volumes for the carbonic phase from the quartz veins implies somewhat higher PT conditions; from 280° to 335°C and 0.8 to 1.6 kbar. The between pressure interval of 0.7 to 1.6 for both carbonate and quartz veins corresponding to depths of 2.6 to 6 km (Fig. 19).

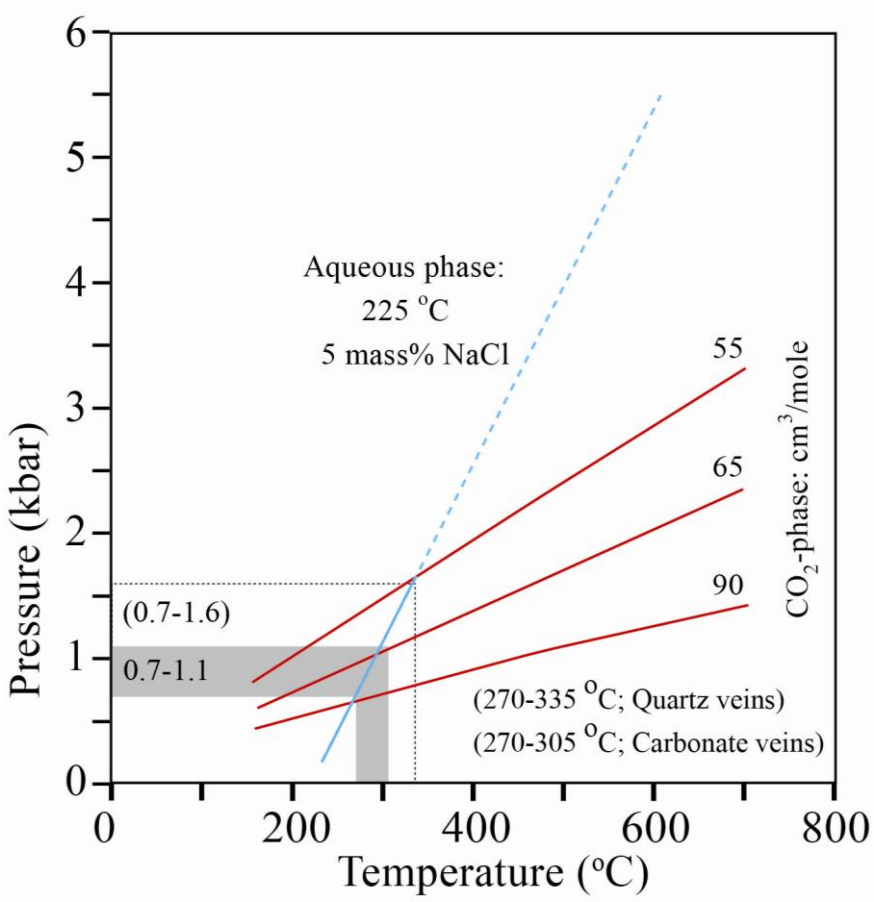


**Fig. 19** P-T diagram based on intersecting isochores of aqueous fluid inclusions with homogenisation of 225˚C and a salinity of 5 mass% NaCl and $CO_2$ inclusions with molar volumes of 55, 65 and 90 $cm^3$/mol. The diagram shows estimated trapping condition for the carbonate veins at 270-305˚C and 0.7-1.1 kbar and for the quartz veins at 270-335˚C and 0.7-1.6 kbar respectively; corresponding to depths of 2.6 to 6 km. Depths calculated on the basis of rock density of 2.6 g/$cm^3$.

In summary, the carbonate veins represent abundant carbonic ($CO_2$±$CH_4$±$N_2$) and aqueous-carbonic ($H_2O$-NaCl-$CO_2$±$CH_4$) fluid inclusions with low salinity (<7 wt% NaCl eq.), similar to those reported from gold-rich vein deposits in CED (Botros, 2002; Zoheir and Lehmann, 2011).

## 7. Conclusions

The field relationships and petrological, geochemical, microthermometic and isotopic compositions of ophiolitic rocks from the north and south of Meatiq area (CED) provide new insights into the source of fluid that has caused abundant pervasive carbonation of these rocks, the conditions under which the alteration occurred, and element mobility associated with this process.

Two serpentine assemblages, lizardite/chrysotile and antigorite occur in Meatiq area. Petrological and geochemical results indicate that antigorite underwent more intensive prograde alteration/metamorphism than the lizardite. However it is not clear whether the transition of lizardite to antigorite occurred in subduction setting or during regional greenschist facies metamorphism in the area. Fluid-mobile elements (Li, As, Au, S, Pb, U, Ba, Sr except Sb and Cs) have also been remobilised due to this transition. This is the first time that gold has observed to be mobilising during transition of lizardite to antigorite. This may suggest lizardite to

have been an important source for gold in vein-type related deposit in CED. The talc-rich rocks have spatial association and clear petrologic relationship with serpentinite protoliths. These rocks mark the zone of faulting and shearing in the ophiolitic rocks of Meatiq area and provide evidence of channeled fluid flow and mass transfer during the deformation history and prograde metamorphism.

Fluid inclusion studies in carbonate veins are comparable to some of other gold-rich vein deposits in the CED showing the important role of low salinity $CO_2$-rich fluid in remobilising of gold in the ophiolitic rocks of Neoproterozoic. Based on fluid inclusion microthermometry, carbonate alteration occurred at temperature of $300 \pm 30^{\circ}C$ and pressure of 0.7 to 1.6 kbar corresponding to a depth of ~2.6 to ~6 km. Isotopic data of carbonate veins in shear zones show large flux of mantle $CO_2$-rich fluid in the form of pervasive carbonate veins and alteration in the ophiolitic rocks during Neoproterozoic. The C isotopic value of serpentinites indicates that they have undergone carbonation from mantle derived C-rich fluid while the radiogenic Sr and O values in serpentinites indicate later modification by surface fluid such as meteoric water, connate fluid or seawater. The Atg-serpentinites are intensively altered and has a greater proportion of carbonate which is evidenced by isotopic values closer to mantle signature.

Pervasive carbonate veins and related alteration products in CED representing a natural analogue of mantle degassing and crustal $CO_2$ sequestration in Neoproterozoic. This natural analogue can provide valuable insights into the mechanism of carbonation, chemical (or elements mobility) controls, paleoclimate, ending glaciation and life diversity on the scale and the rate of carbonation during Neoproterozoic orogeny.

**References:**


- Abd El-Rahman, Y., Polat, A., Dilek, Y., Kusky, M.T., El-Sharkawi, M., Said, A., 2012. Cryogenian ophiolite tectonics and metallogeny of the Central Eastern Desert of Egypt. International Geology Review, iFirst, 1-15.
- Abdeen,M.M., and Greiling, R.O., 2005, A quantitative structural study of Late Pan-African compressional deformation in the Central Eastern Desert (Egypt) during Gondwana assembly. Gondwana Research, 8, 457-471.
- Abdel Aal A.Y., Farahat, E.S., Hoinkens, G., El-Mahalawi, M.M., 2003. Ophiolites from the Egyptian Shield: a case for a possible inter-arc origin. Österreichischen Geologischen Gesellschaft, 148, 81-83
- Abdel Kader, Z., 1974. Mineralogical and geochemical studies on some Egyptian Mg-rich layer silicates (chloritites, serpentinites and talcs). PhD thesis, Cairo University, 270 p.
- Agrinier, P., Hékinian, R., Bideau, D., Javoy, M., 1995. O and H stable isotope compositions of oceanic crust and upper mantle rocks exposed in the Hess Deep near the Galapagos Triple Junction. Earth and Planetary Science Letters, 136, 183-196.
- Ahmed, A. H., Hanghøj, K., Kelemen, P. B., Hart, S. R., Arai, S., 2006. Osmium isotope systematics of the Proterozoic and Phanerozoic ophiolitic chromitites: in situ ion probe analysis of primary Os-rich PGM. Earth Planetary Science Letters. 245, 777-791.
- Ahmed, A.H., Arai, S., Attia, A.K., 2001. Petrological characteristics of podiform chromitites and associated peridotites of the Pan African ophiolite complexes of Egypt. Mineralium Deposita, 36, 72-84.
- Akaad, M.K., Noweir, A.M., 1972. Some Aspects of the Serpentinites and their Associated Derivatives along Qift-Quesir Road, Eastern Desert. Annals of the Geological Survey of Egypt, 2, 251-270.
- Akaad, M.K., Noweir, M.A., 1980. Geology and lithostratigraphy of the Arabian Desert orogenic belt of Egypt between latitudes $25^{0}35$ and $26^{0}30$ N, N.I.A.G. Bulletin, Jeddah, 2, 127-136.
- Ali, K.A., Stern, R.J., Manton, W.I., Kimura, J.I., Khamis, H.A., 2009. Geochemistry Nd isotopes and U-Pb SHRIMP zircon dating of Neoproterozoic volcanic rocks from the Central Eastern Desert of Egypt: New insight into the ~750 Ma crust-forming event. Precambrian Research, 171, 1-22.

- Ali-Bik, W. M., Taman, Z., El Kalioubi, B., Abdel Wahab, W., 2012. Serpentinite-hosted talc–magnesite deposits of Wadi Barramiya area, Eastern Desert, Egypt: Characteristics, petrogenesis and evolution. Journal of African Earth Sciences, 64, 77–89.
- Alt, J.C., Muehlenbachs, K., Honnorez, J., 1986. An oxygen isotopic profile through the upper kilometer of the oceanic crust, DSDP Hole 504B. Earth Planet. Sci. Lett. 80, 217–229.
- Andréani, M., Mével, C., Boullier, A.M., Escartin, J., 2007. Dynamic control on serpentine crystallisation in veins: constraints on hydration processes in oceanic peridotites. Geochemistry, Geophysics, Geosystems, Q02012. http://dx.doi.org/10.1029/2006GC001373.
- Andresen, A., El-Rus, M.M.A., Myhre, P.I., Boghdady, G.Y., Corfu, F., 2009. U–Pb TIMS age constraints on the evolution of the Neoproterozoic Meatiq Gneiss Dome, Eastern Desert, Egypt. International Journal Earth Sciences 98, 481-497.
- Auzende, A.L., Devouard, B., Guillot, S., Daniel, I., Baronnet, A., Lardeaux, J.M., 2002. Serpentinites from Central Cuba: petrology, and HRTEM study. European Journal of Mineralogy, 14, 905-914.
- Auzende, A.L., Guillot, S., Devouard, B., Baronnet, A., 2006. Serpentinites in Alpine convergent setting: effects of metamorphic grade and deformation on microstructures. European Journal of Mineralogy, 18, 21-33.
- Aydal, D., 1990. Gold-bearing listwaenites in the Arac Massif, Kastamonu, Turkey. Terra Nova, 2, 43-52.
- Azer, M.K., 2013. Evolution and economic significance of listwaenites associated with Neoproterozoic ophiolites in South Eastern Desert, Egypt. Geologica Acta , 1, 113-128.
- Azer, M.K., Stern, R.J., 2007. Neoproterozoic (835-720 Ma) serpentinites in the Eastern Desert, Egypt: Fragments of forearc mantle. The Journal of Geology, 115, 457-472.
- Barnes D.J., Eldam, R., Lee, A.C., Errico, C.J., Loewy, S., Cisneros, M., in press. Petrogenesis of serpentinites from the Franciscan Complex, western California, USA. Lithos.
- Barnes, I., O'Neil, J.R., Rapp, J.B., White, D.E., 1973. Silicacarbonate alteration of serpentine: Wall rock alteration in mercury deposits of the California Coast Ranges. Economic Geology, 68, 388-398.
- Basta, E.Z., Abdel Kader, Z., 1969. The mineralogy of Egyptian serpentinites and talc-carbonates. Min. Mag., 37, 394-408.
- Bodnar, R.J., 2003. Introduction to aqueous-electrolyte fluid inclusions. In Samson, I., Anderson, A. and Marshall, D. (eds.), Fluid Inclusions: Analysis and Interpretation. Mineral. Assoc. Canada, Short Course 32, 81-99.
- Bonatti, E., Michael, P. J., 1989. Mantle peridotites from continental rifts to oceanic basins to subduction zones. Earth and Planetary Science Letters, 91, 297-311.
- Boschi, C., Früh-Green, G.L., Delacour, A., Karson, J.A., Kelley, D.S., 2006. Mass transfer nd fluid flow during detachment faulting and development of an oceanic core complex, Atlantis Massif (MAR 30°N). Geochemistry, Geophysics, Geosystems. 7, Q01004. doi:10.1029/2005GC001074.
- Botros, N.S., 2002, Metallogeny of gold in relation to the evolution of the Nubian Shield in Egypt. Ore Geology Reviews, 19, 137-164.
- Botros, N.S., 2004. A new classification of the gold deposits of Egypt. Ore Geology Reviews, 25, 1-37.
- Bregar, M., Bauernhofer, A., Pelz, K., Kloetzli, U., Fritz, H., and Neumayr, P., 2002. A late Neoproterozoic magmatic core complex in the Eastern Desert of Egypt: Emplacement of granitoids in a wrench-tectonic setting. Precambrian Research, 118, 59-82.
- Bucher, K., Frey, M., 1994. Petrogenesis of Metamorphic Rocks. Springer-Verlag, Berlin-Heidelberg, Germany, 318 pp.
- Buisson, G., and LeBlanc, M., 1987, Gold in mantle peridotites from upper Proterozoic ophiolites in Arabia, Mali, and Morocco. Economic Geology, 82, 2091-2097.
- Buisson, G., Leblanc, M., 1985. Gold in carbonatized ultramafic rocks from ophiolite complexes. Economic Geology, 80, 2026-2029.
- Buisson, G., Leblanc, M., 1986. Gold-bearing listwaenites (carbonatized ultramafic rocks) from ophiolite complexes. In: Gallagher, J.M., Ixer, R.A., Neary, C.R. (eds.), Metallogeny of Basic and Ultrabasic Rocks. London, Institution of Mining and Metallurgy, 121-132.

- Cavanagh, B.J., 1979. Rb-Sr Geochronology of some Pre- Nubian Igneous Complexes of Central and Northeastern Sudan. Ph.D. Thesis, University of Leeds, 239 pp. (unpublished).
- Coleman, R. G., 1977. Ophiolites. Berlin, Springer, 229 p.
- Collins, P.L.F, 1979. Gas hydrates in $CO_2$-bearing fluid inclusions and the use of freezing data for estimation of salinity. Economic Geology, 74, 1435-1444.
- Dasgupta, R., Hirschman, M.M., 2010. The deep carbon cycle and melting in Earth's interior. Earth and Planetary Science Letters, 298, 1-13.
- Debret, B., Nicollet, C., Andréani, M., Schwartz, S., Godard, M., 2013. Three steps of serpentinization in an eclogized oceanic serpentinization front (Lanzo massif-Western Alps). Journal of Metamorphic Geology, 31, 165-186.
- Deines, P., 1989. Stable isotope variations in carbonatites. In: Bell, K. (Ed.), Carbonatites: Genesis and evolution. Unwin Hyman, London, Boston, Sydney, Wellington, pp. 301-359.
- Deines, p., 2002. The carbon isotope geochemistry of mantle xenoliths. Earth-Science Reviews, 58, 247-278.
- Demény, A., Ahijado, A., Casillas, R., Vennemann, T.W., 1998. Crustal contamination and fluidrrock interaction in the carbonatites of Fuerteventura _Canary Islands, Spain/: a C, O, H isotope study. Lithos 44, 101-115
- Des Marais, D. J., and Moore, J. G., 1984, Carbon and its isotopes in mid-oceanic basaltic glasses: Earth and Planetary Science Letters, 69, 43-57.
- Deschamps, F., Godard, M., Guillot, S., Chauvel, C., Andreani, M., Hattori, K., Wunder, B., France, L., 2012. Behavior of fluid-mobile elements in serpentines from abyssal to subduction environments: Examples from Cuba and Dominican Republic. Chemical Geology, 312-313, 93-117.
- Deschamps, F., Guillot, S., Godard, M., Andreani, M., Hattori, K.H., 2011. Serpentinites act as sponges for fluid-mobile elements in abyssal and subduction zone environments. Terra Nova 23, 171-178.
- Deschamps, F., Guillot, S., Godard, M., Chauvel, C., Andreani, M., Hattori, K.H., 2010. In situ characterization of serpentinites from forearc mantle wedges: timing of serpentinization and behavior of fluid-mobile elements in subduction zones. Chemical Geology 269, 262-277.
- Diamond, L.W., 2003. Chapter 3. Systematics of $H_2O$ inclusions. In: Fluid Inclusions: Analysis and Interpretation (I. Samson, A. Anderson, D. Marshall, eds.) Mineralogical Association of Canada Short Course Series Volume 32: 55-79.
- Dick, H. B., Bullen, T., 1984. Chromian spinel as a petrogenetic indicator in abyssal and Alpine-type peridotites and spatially associated lavas. Contributions to Mineralogy and Petrology, 86, 54-76.
- Downs, R.T., 2006. The RRUFF Project: an integrated study of the chemistry, crystallography, Raman and infrared spectroscopy of minerals. Program and Abstracts of the 19th General Meeting of the International Mineralogical Association in Kobe, Japan. O03-13.
- Eiler, J., 2001. Oxygen isotope variations of basaltic lavas and upper mantle rocks. Mineralogical Society of America, pp. 319-364.
- El Bahariya, G.A., 2008, Geology, mineral chemistry and petrogenesis of Neoproterozoic metamorphosed ophiolitic ultramafics, Central Eastern Desert, Egypt: Implication for the classification and origin of the ophiolitic mélange: Egyptian Journal of Geology, 52, 55-81.
- El Gaby, S., 2005. Integrated evolution and rock classificationof the Pan-African belt in Egypt. First Symposium on the Classification of the Basement Complex of Egypt, pp. 1-9.
- El Gaby, S., El-Nady, O., and Khudeir, A., 1984, Tectonic evolution of the basement complex in the Central Eastern Desert of Egypt: Geologische Rundschau, 73, 1019-1036.
- El Gaby, S., List, F.K., Tehrani, R., 1988. Geology, evolution and metallogenesis of the Pan-African belt in Egypt. In: El Gaby, S., Greiling, R.O. (eds.), 1988. The Pan-African Belt of Northeast Africa and Adjacent Areas: Tectonic Evolution and Economic Aspects of a Late Proterozoic Orogen, Vieweg and Sohn, Braunschweig/Wiesbaden, Germany, 299 pp.
- El Sharkawy, M.A., El Bayoumi, R.M., 1979. The ophiolites of Wadi Ghadir area, Eastern Desert, Egypt. Annals Geol.Survey Egypt 9, 125-135.

- El-Ramly, M.F., Akaad, M.K., 1960. The basement complex in the Central Eastern Desert. Geological survey of Egypt. 8, 35p.
- El-Sayed, M.M., Furnes, H., Mohamed, F.H., 1999. Geochemical constraints on the tectonomagmatic evolution of the late Precambrian Fawakhir ophiolite, Central Eastern Desert, Egypt. Journal of African earth Sciences, 29, 515-533.
- Engel, A.E.J., Dixon, T.H., Stern, R.J., 1980. Late Precambrian evolution Afro-Arabian crust from ocean arc to craton. Geological Society of America Bulletin, 91, 699-706.
- Evans, B.W., 2004. The serpentinite multisystem revisited: chrysotile is metastable. International Geology Review 46, 479-506.
- Evans, B.W., 2010. "Lizardite versus antigorite serpentinite: magnetite, hydrogen, life (?)". Geology, 38, 879-882.
- Evans, B.W., Tromsdorff, V., 1978. Petrogenesis of garnet lherzolite, Cima di Gagnone, Lepontine Alps. Earth and Planetary Science Letters, 39, 55-71.
- Exley, R.A., Mattey, D.P., Clague, D.A. Pillinger, C.T., 1986. Carbon isotope systematics of a mantle 'hotspot': a comparison of Loihi seamount and MORB glasses. Earth and Planetary Science Letters, 78, 189-199.
- Fall, A., Tattitch, B. and Bodnar, R.J., 2011. Combined microthermometric and Raman spectroscopic technique to determine the salinity of $H_2O$-$CO_2$-NaCl fluid inclusions based on clathrate melting. Geochimica et Cosmochimica Acta, 75, 951-964.
- Farahat, E.S., 2001. Comparative petrological studies of some pillowed lavas in the Eastern Desert, Egypt. Ph.D. Thesis, Minia University, Minia, Egypt, 251 pp.
- Farahat, E.S., 2008. Chrome-spinels in serpentinites and talc carbonates of the El Ideid-El Sodmein District, central Eastern Desert, Egypt: their metamorphism and petrogenetic implications. Chemie der Erde, 68, 193-205.
- Fitches, W.R., Graham, R.H., Hussein, I.M., Ries, A.C., Shackleton, R.M. and Price, R.C., 1983. The late Proterozoic ophiolite of Sol Hamed, NE Sudan. Precambrian Res., 19: 385-411.
- Fowler, M.B., William, H.R., Windely. B.F., 1981. The metasomatic developments of zoned ultramafic balls from Fiskenaesset, West Greenland, Min. Mag., 45, 171-177.
- Früh-Green G. L., Connolly J. A. D., Plas A., Kelley D. S. and Grobéty B., 2004. Serpentinization of oceanic peridotites: implications for geochemical cycles and biological activity. In The Subseafloor Biosphere at Mid-ocean Ridges, Geophys. Monogr. Ser. 144 (eds. W. S. D Wilcock et al.). AGU, Washington, DC, 119-136.
- Früh-Green G. L., Plas A. and Lécuyer C. (1996) Petrologic and stable isotope constraints on hydrothermal alteration andserpentinization of the EPR shallow mantle at Hess Deep (Site 895). Proc. ODP Sci. Res. 147, 255-293.
- Ghoneim, M. F., Salem, I. A., and Hamdy, M. M., 1999. On the petrogenesis of magnesite from Gebel El-Maiyit, central Eastern Desert, Egypt. Fourth International Conference on the Geology of the ArabWorld, 1, 575-593.
- Gillis, K. M., Ludden, J. N., Smith, A. D., 1992. Mobilization of REE during crustal aging in the Troodos Ophiolite, Cyprus, Chemical Geology, 98, 71-86.
- Groppo, C., Compagnoni, R., 2007. Metamorphic veins from the serpentinites of the Piemonte Zone, western Alps, Italy: a review. Periodico di Mineralogia 76, 127-153.
- Guillot, S., Hattori, K., Agard, P., Schwartz, S., Vidal, O., 2009. Exhumation processes in oceanic and continental subduction contexts: a review. In: Lallemand, S., Funiciello, F. (eds.), Subduction Zone Dynamics. Springer, Verlag Berlin Heidelberg, pp. 175-204.
- Habib, M.E., Ahmed, A.A., El Nady, O.M., 1985b. Tectonic evolution of the Meatiq infrastructure, Central Eastern Desert, Egypt. Tectonics, 4 (7), 613-627.
- Hamdy, M.M., Harraz, Z.H., Aly, A.G., 2013. Pan-African (intraplate and subduction-related?) metasomatism in the Fawakhir ophiolitic serpentinites, Central Eastern Desert of Egypt: mineralogical and geochemical evidences. Arabian Journal of Geosciences, 6:13-33
- Hattori, K.H., Guillot, S., 2003. Volcanic fronts form as a consequence of serpentinite dehydration in the forearc mantle wedge. Geology 31 (6), 525-528.

- Hattori, K.H., Guillot, S., 2007. Geochemical character of serpentinites associated with high- to ultrahigh-pressure metamorphic rocks in the Alps, Cuba, and the Himalayas: recycling of elements in subduction zones. Geochemistry, Geophysics, Geosystems 8 (9), http://dx.doi.org/10.1029/2007GC001594.
- Humphris, S. E., Thompson, G., 1978. Trace element mobility during hydrothermal alteration of oceanic basalts, Geochimica et Cosmochimica Acta, 42, 127-136.
- Ishii, T., Robinson, P. T., Maekawa, H., Fiske, R., 1992. Petrological studies of peridotites from diapiric serpentinite seamounts in the Izu-Ogasawara-Marianaforearc, leg 125. In Proceedings of the Ocean Drilling Program, Scientific Results 125. College Station, TX, Ocean Drilling Program, p. 445-485.
- Khalil, I.K., Helba, A.H., Mücke, A., 2003. Genesis of the gold mineralization at the Dungash gold mine area, Eastern Desert, Egypt: a mineralogical-microchemical study. Journal of African Earth Sciences, 37, 111-122.
- Koç, S., Kadıoğlu, Y.K., 1996. Mineralogy, geochemistry and precious metal content of Karacakaya (Yunusemre-Eskisehir) listwaenites. Ofioliti, 21, 125-130.
- Kochin, G.G., and Bassyni, F.A., 1968, The mineral resources of the U.A.R. Part I. Metallic minerals. Egyptian Geological Survey and Mining Authority: Internal Report 18/68.
- Kodolányi, J., Pettke, T., 2011. Loss of trace elements from serpentinites during fluid assisted transformation of chrysotile to antigorite—an example from Guatemala. Chemical Geology, 284, 351-362.
- Kodolányi, J., Pettke, T., Spandler, C., Kamber, B.S., Gméling, K., 2012. Geochemistry of ocean floor and fore-arc serpentinites: constraints on the ultramafic input to subduction zones. Journal of Petrology 53, 235-270.
- Kröner, A., Krüger, J., Rashwan, A.A., 1994. Age and tectonic setting of granitoid gneisses in the Eastern Desert of Egypt and south-west Sinai. Geologische Rundschau. 83 , 502-513.
- Kröner, A., Stern, R.J., Dawoud, A.S., Compston, W. and Reischmann, T., 1987. The Pan-African continental margin in NE Africa: evidence from a geochronological study of granulites at Sabaloka, Sudan. Earth Planet. Sci. Lett., 85, 91-104.
- Kröner, A., Todt, W., Hussein, I.M., Manour, M., Rashwan, A.A., 1992. Dating of late Proterozoic ophiolites in Egypt and the Sudan using the single grain zircon evaporation technique. Precambrian Research, 59, 15-32.
- Li, X.P., Rahn, M., Bucher, K., 2004. Serpentinites of the Zermatt–Saas ophiolite complex and their texture evolution. Journal of Metamorphic Geology 22, 159-177.
- Li, Z.-X.A., Lee, C.-T.A., 2006. Geochemical investigation of serpentinized oceanic lithospheric mantle in the Feather River Ophiolite, California: implications for the recycling rate of water by subduction. Chemical Geology, 235, 161-185.
- Liégeois, J.-P., and Stern, R.J., 2010, Sr-Nd isotopes and geochemistry of granite-gneiss complexes from the Meatiq and Hafafit domes, Eastern Desert, Egypt: No evidence for pre-Neoproterozoic crust: Journal of African Earth Sciences, 57, 31-40.
- Loizenbauer, J., Wallbrecher, E., Fritz, H., Neymayr, P., Khudeir, A.A., Kloetzli, U., 2001. Structural geology, single zircon ages and fluid inclusion studies of the Meatiq metamorphic core complex: implications for Neoproterozoic tectonics in the Eastern Desert of Egypt. Precambrian Research, 110, 357-383.
- Lundmark, A.M., Andresen, A., Hassan, M.A., Augland, L.E., and Boghdady, G.Y., 2012, Repeated magmatic pulses in the East African Orogen in the Eastern Desert, Egypt: An old idea supported by new evidence. Gondwana Research, 22, 227-237.
- McDonough, W.F., and Sun, S.S., 1995. Composition of the Earth. Chemical Geology, 120, 223-253.
- Mellini, M., Trommsdorff, V., Compagnoni, R., 1987. Antigorite polysomatism: behavior during progressive metamorphism. Contributions to Mineralogy and Petrology, 97, 147-155.
- Mével, C., 2003. Serpentinization of abyssal peridotites at midocean ridges. C. R. Geoscience. 335, 825-852.
- Muehlenbachs, K., 1987. Oxygen isotope exchange during weathering and low temperature alteration. In: MAC Short course, Stable Isotope Geochemistry of Low-Temperature Fluids, 162-186.
- Neumayr, P., Hoinkes, G., Puhl, J., Mogessie, A., Khudeir, A.A., 1998. The Meatiq dome (Eastern Desert, Egypt) a Precambrian metamorphic core complex: petrological and geological evidence. Journal of Metamorphic Geology. 16, 259-279.

- Neumayr, P., Mogessie, A., Hoinkes, G., Puhl, J., 1996. Geological Setting of the Meatiq metamorphic core complex in the Eastern Desert of Egypt based on amphibolite geochemistry. Journal of African Earth Science. 23, 331-345.
- Ohara, Y., 2006. Mantle process beneath Philippine Sea back-arc spreading ridges: a synthesis of peridotite petrology and tectonics. Island Arc, 15, 119-129.
- Ohara, Y., Ishii, T., 1998. Peridotites from southern Mariana forearc: heterogeneous fluids supply in mantle wedge. Island Arc, 7, 541-558.
- Ohara, Y., Stern, R. J., Ishii, T., Yurimoto, H., Yamazaki, T., 2002. Peridotites from the Mariana Trough: first look at the mantle beneath an active back-arc basin. Contributions to Mineralogy and Petrology, 143, 1-18.
- Ohmoto, H., 1986. Stable isotope geochemistry of ore deposits. In stable isotopes in high temperature geological processes. Reviews of Mineralogical Society of America 16, 491-560.
- Oweiss, Kh.A., El Naggar, A.A., Abdel Razik, K.A., Moselhy, N., Ali, A.B., 2001. Gold exploration at Heiani area, South Eastern Desert, Egypt. Annals Geological Survey of Egypt, XXIV, 435-450.
- Padron-Navarta, J.A., Sanchez-Vizcaino, V.L., Garrido, C.J., Gómez-Pugnaire, M.T., Jabaloy, A., Capitani, G.C., Mellini, M., 2008. Highly ordered antigorite from Cerro del Almirez HP-HT serpentinites, SE Spain. Contributions to Mineralogy and Petrology, 156, 679-688.
- Phillips, A. H., Hess H. H., 1936. Metamorphic differentiation at contacts between serpentinite and siliceous country rocks. American Mineralogist, 2l, 333-362.
- Pitcairn, K.I., Warwick, E.P., Milton J.A., Teagle, A.H.D., 2006. Method for Ultra-Low-Level Analysis of Gold in Rocks. Analytical Chemistry 78, 1290-1295.
- Ramadan, T.M., 2002. Exploration for gold-bearing listwaenites at Um Khasila area, Central Eastern Desert, Egypt. Egyptian Journal of Remote Sensing and Space Sciences. 5, 63-76.
- Reischmann, T., 1986. Geoiogie und Genese Spriitproterozoischer Vulkanite der Red Sea Hills, Sudan. Ph.D. Thesis, Johannes Gutenberg Universith't Mainz, 202 pp. (unpublished).
- Robinson, P., Spear, F.S., Schumacher, J.C., Laird, J., Klein, C., Evans, B.W. & Doolan, B.L., 1982. Phase relations of metamorphic amphiboles: natural occurrence and theory. In Amphiboles and other Hydrous Pyriboles-Mineralogy (D.R. Veblen & P.H. Ribbe, eds.). Reviews in Mineralogy. 9B, 1-227.
- Roedder, E., 1984. Fluid inclusions. Mineralogical Society of America, Reviews in Mineralogy and Geochemistry, 12, 644 pp.
- Sakai, R., Kusakabe, M., Noto, M., Ishii, T., 1990. Origin of waters responsible for serpentinization of the Izu-Ogasawara-Mariana forearc seamounts in view of hydrogen and oxygen isotope ratios. Earth and Planetary Science Letters, 100, 291-303.
- Saleh, M.G., 2006. The chromite deposits associated with ophiolite complexes, Southeastern Desert, Egypt: Petrological and geochemical characteristics and mineralization. Chinese Journal of Geochemistry, 24, 307-317.
- Salem, I. A., Ghoneim, M. F., Zahran, A. A., and Hamdy, M. M., 1997. Petrology and genesis of the ultramafichosted vein magnesite deposits at G. El-Rubshi, Central Eastern Desert, Egypt. Third Conference on Geochemistry, Alexandria University, 1, 241-267.
- Salters, V.J.M., Stracke, A., 2004. Composition of the depleted mantle. Geochemistry, Geophysics, Geosystems, 5, Q05B07, 27pp.
- Scambelluri, M., Fiebig, J., Malaspina, N., Müntener, O., Pettke, T., 2004a. Serpentinite subduction: implications for fluid processes and trace-element recycling. International Geology Review, 46, 595-613.
- Scambelluri, M., Müntener, O., Hermann, J., Piccardo, G.B. and Trommsdorff, V., 1995. Subduction of water into the mantle: history of an alpine peridotite. Geology, 23, 459-462.
- Scambelluri, M., Müntener, O., Ottolini, L., Pettke, T.T., Vannucci, R., 2004b. The fate of B, Cl and Li in the subducted oceanic mantle and in the antigorite breakdown fluids. Earth and Planetary Science Letters, 222, 217-234.
- Schwartz, S., Guillot,S., Reynard, B., Lafay, R., Debret, b., Nicollet, C., Lanari, P., Auzende, A., in press. Pressure–temperature estimates of the lizardite/antigorite transition in high pressure serpentinites, Lithos.

- Shackleton, R.M., Ries, A.C., Graham, R.H., Fitches, W.R., 1980. Late Precambrian ophiolite melange in the Eastern Desert of Egypt. Nature, 285, 472-474.
- Shepherd, T.J., Rankin, A.H. and Alderton, D.H.M., 1985. A practical guide to fluid inclusion studies. Blackie, Glasgow.
- Sheppard S. M. F., 1980. Isotopic evidence for the origins of water during metamorphic processes in oceanic crust and ophiolite complexes. In Colloque Internationau du C.N.R.S Association mafiques ultra-mafiques dans les orogénes 272, 135-147.
- Shervais, J. W., Kimbrough, D. L., Renne, P. R., Hanan, B. B., Murchey, B., Snow, C. A., Schuman, M. M. Z., Beaman, J., 2004. Multi-stage origin of the Coast Range ophiolite, California: implications for the life cycle of supra-subduction zone ophiolites. International Geology Review, 46, 289-315.
- Simandl, G.J., Ogden, D., 1999. Ultramafic-hosted talc–magnesite. In: Simandl, G.J., Hora, Z.D., Lefebure, D.V. (eds.), Selected British Columbia mineral deposit profiles, Industrial Minerals, vol. 3. British Columbia Ministry of Energy and Mines, Open file 1999-10, 65-71.nson
- Stern, R,J., Johanson, P.R., Kroner, A., Yibas, B., 2004. Neoproterozoic ophiolites of the Arabian–Nubian Shield. In: Kusky TM (ed) Precambrian ophiolites and related rocks. Developments in Precambrian geology, Elsevier, Amsterdam, 13, 95-28.
- Stern, R.J. and Hedge, C.E., 1985. Geochronologic and isotopic constraints on Late Precambrian crustal evolution in the Eastern Desert of Egypt. American Journal of Science, 285, 97-127.
- Stern, R.J., Gwinn, C.J., 1990. Origin of late Precambrian intrusive carbonates, Eastern Desert of Egypt and Sudan: C, O and Sr isotopic evidence. Precambrian Research 46, 259-272.
- Sturchio, N.C., Sultan, M., Batiza, R., 1983. Geology and origin of Meatiq dome, Egypt: A Precambrian metamorphic core complex? Geology 11, 72-76.
- Sultan, M., Arvidson, R.E., Sturchio, N.C., 1986. Mapping of serpentinites in the Eastern Desert of Egypt by using Landsat thematic mapper data. Geology 14, 995-999.
- Sultan, M., Arvidson, R.E., Sturchio, N.C., 1986. Mapping of serpentinites in the Eastern Desert of Egypt using Landsat Thematic Mapper data. Geology, 14, 995-999.
- Takla, M.A., Basta, E.Z., Surour, A.A., 1991. Chloritites at the contact of some ophiolitic ultramafics, Eastern Desert, Egypt. Egyptian Mineralogist, 3, 151-165.
- Takla, M.A., Basta, F.F., Surour, A.A., 1992. Petrology and Mineral Chemistry of Rodingites associating the Pan-African Ultramafics of Sikait-Abu Rusheid area, South Eastern Desert, Egypt. Geology of the Arab World, 491-507.
- Takla, M.A., Noweir, M.A., 1980. Mineralogy and mineral chemistry of the ultramafic mass of El-Rubshi, Eastern Desert, Egypt. Neues Jahrbuch für Mineralogie-Abhandlungen, 140, 17-28.
- Takla, M.A., Surour, A.A., 1996. On the occurrence of Ni-sulphides and arsenides in some Egyptian serpentinites. Egyptian Minerals, 8, 1-18.
- Taylor, H.P., Frechen, J. and Degens, E.T., 1967. Oxygen and carbon isotope studies of carbonatites from the Laacher See district, West Germany and the Alno district, Sweden. Geochimica et Cosmochimica Acta, 31, 407-430.
- Trommsdorff, V., Sanchez-Vizcaino, V.L., Gomez-Pugnaire, M.T., Muntener, O., 1998. High pressure breakdown of antigorite to spinifex-textured olivine and orthopyroxene, SE Spain. Contributions to Mineralogy and Petrology 132, 139-148.
- Uçurum, A., 2000. Listwaenites in Turkey: Perspectives on formation and precious metal concentration with reference to occurrences in East-Central Anatolia. Ofioliti, 25, 15-29.
- Van den Kerkhof, A., Thiéry, R., 2001. Carbonic Inclusions. Lithos 55, 49-68.
- Veizer, J., Compston, W., Clauer, N. and Schidlowski, M., 1983. $^{87}Sr/^{86}Sr$ in Late Proterozoic carbonates: evidence for a 'mantle' event at ~900 Ma. Geochimica et Cosmochimica Acta, 47, 295-302.
- Wallbrecher, E., Fritz, H.E., Khudier, A.A., Farahad, F., 1993. Kinematics of Panafrican thrusting and extension in Egypt. In: Thorweihe, U., Schandelmeier, H. (eds.), Geoscientific Research in Northeast Africa. Proceedings of the international conference on geoscientific research in Northeast Africa. Balkema, Rotterdam, p. 27-30.

- Wenner, B.D., Taylor, P.H., 1973. Oxygen and hydrogen isotope studies of the serpentinization of ultramafic rocks in oceanic environments and continental ophiolite complexes. American Journal of Science, 273, 207-239.
- Zimmer, M., Kröner, A., Jochum, K.P., Reischmann, T., Todt, W., 1995. The Gabal Gerf complex: A Precambrian N-MORB ophiolite in the Nubian Shield, NE Africa. Chemical Geology, 123, 29-51.
- Zoheir, B.A., Lehmann, B., 2011. Listvenite-lode association at the Barramiya gold mine, Eastern Desert, Egypt. Ore Geology Reviews, 39, 101-115.

# Conference abstract

Geophysical Research Abstracts
Vol. 15, EGU2013-9967, 2013
EGU General Assembly 2013


# Regional carbonate alteration in the eastern desert of Egypt: Isotopic evidence for a mantle-derived fluid source

Iain Pitcairn (1), Ahmad Boskabadi (1), Curt Broman (1), Adrian Boyce (2), Damon Teagle (3), Matthew Cooper (3), Mokhles Azer (4), Fathy Mohamed (5), and Robert Stern (6)

(1) Department of Geological Sciences, Stockholm University, Stockholm, Sweden, (2) Scottish Universities Environmental Research Centre, East Kilbride, UK, (3) National Oceanography Centre Southampton, University of Southampton, SO14 3ZH, UK, (4) Geology Department, National Research Centre, Cairo, Egypt , (5) Geology Department, Faculty of Science, Alexandria University, Alexandria, Egypt, (6) Geosciences Department, University of Texas at Dallas, Texas, USA

The migration of carbonate-rich solutions was common during deformation and metamorphism of the Arabian-Nubian Shield (ANS), forming veins and dykes, and causing diffuse and pervasive carbonation of a wide range of basement rocks (1). Pervasive carbonate alteration focused along faults and shear zones is extremely abundant in ultramafic and mafic components of the ophiolitic sequences of the Central Eastern Desert (CED) of Egypt. Despite the abundance of this alteration, there have been few isotopic investigations into the source of fluids that caused the alteration. Isotopic investigations of intrusive carbonate dykes reveal a mixed mantle-sedimentary C source ($\delta^{13}C_{pdb}$ ranges -8 to +3.5) (1), but the genetic relationship between these and the pervasive carbonate alteration is unclear. We report isotopic (C, O, Sr) compositions of whole rocks and veins, and fluid inclusion compositions from veins in a sequence of carbonated mafic and ultramafic rocks surrounding the Meatiq core complex (MCC) in the CED of Egypt.

The MCC occurs within the Najd mega shear zone corridor and represents one of the structurally lowest units in the CED basement (2). It is exposed in a tectonic window through the Neoproterozoic cover nappes that comprise variably carbonatized/silicified ophiolitic sequences and metasedimentary and metavolcanic rocks. Carbonate alteration replaces silicates with dolomite, magnesite and ankerite with the ultramafic rocks becoming talc-carbonate rocks. Vein carbonate is dominantly dolomite and magnesite.

Carbon, O and Sr isotopic compositions of carbonated serpentinites and metavolcanics and of pure carbonate veins are used to constrain the origin of the fluid involved. The $\delta^{13}C_{pdb}$ and $\delta^{18}O_{SMOW}$ isotope compositions of pure vein carbonate range -6.8 to -8.1 and 6.4 to 10.5 respectively, whereas the age-corrected $^{87}Sr/^{86}Sr$ ratios range 0.7028 to 0.7034. The $\delta^{13}C_{pdb}$, $\delta^{18}O_{SMOW}$ and $^{87}Sr/^{86}Sr$ values in carbonated metavolcanics range -9.3 to -10.0, 9.4 to 11.1, and 0.7029 - 0.7031 respectively. The carbonated and weekly carbonated serpentinites have $\delta^{13}C$ values ranging -4.1 to -5.9, $\delta^{18}O$ compositions ranging 10.3 to 15.1, and $^{87}Sr/^{86}Sr$ ratios of 0.7039 to 0.7062. Some of the carbonated serpentinites have low Sr contents (0.2 to 0.5 ppm) whereas most samples contain between 6 and 2365 ppm. The isotopic composition of the altered rocks and veins are similar to those from intrusive carbonates in the CED (1). The pure carbonate veins have strong mantle signatures with little or no crustal Sr or surficial C and O. The carbonated serpentinites have Sr isotope ratios indicating mixing between a mantle and a more radiogenic Sr component with higher $\delta^{18}O$. The isotopic data suggests that large fluxes of mantle-derived $CO_2$-rich fluid through the CED basement rocks during the Neoproterozoic. Carbonate veins contain abundant carbonic ($CO_2 \pm CH_4 \pm N_2$) and aqueous-carbonic ($H_2O$-NaCl-$CO_2 \pm CH_4 \pm N_2$) fluid inclusions with low salinity ($<5$ wt.% NaCl eq.), similar to those reported from gold-rich vein deposits in the CED (3). It is possible that the auriferous veins were formed from the same mantle-derived fluids.

1. Stern, R.J., Gwinn, C.J., 1990. Precambrian Research 46, 259–272.

2. Loizenbauer, J., et al. 2001. Precambrian Research 110, 357-383.

3. Botros, N.S., 2002. Ore Geology Reviews 19, 137–164.